

Kyushu Institute of Technology

**Contribution of Solid–liquid–vapor  
Interface and Adjacent Droplets to  
Droplet Evaporation**

Submitted to the Department of Mechanical Engineering

In Partial Fulfilment of the Requirements  
for the Degree of Doctor of Engineering

by

Muhammad Mohib Ur Rehman

February 2023

*To the God who bless me to think and seek for truth in life*

## **Abstract**

The evaporation of droplets on a flat solid surface has been extensively studied, and it is well known that droplets evaporate from the liquid–vapor interface to the surroundings. However, the evaporation of droplets on micro/nanostructured surfaces and the evaporation of droplets surrounded by adjacent droplets is not well understood. In the former case, the contribution of the solid–liquid–vapor three phase interface formed near the macroscopic contact line to droplet evaporation become significant in addition to the liquid–vapor interface. In this work, the effects of solid–liquid–vapor three phase interface and adjacent droplet array on droplet evaporation are investigated theoretically, experimentally, and numerically. In addition, it was clarified that droplets surrounded by adjacent droplet arrays are inhibited from evaporating due to synergistic effects such as arrangement of adjacent droplets and interfacial wettability.

The scale of the solid–liquid–vapor three phase interface was estimated to be in the range of 253-940  $\mu\text{m}$  for the measured droplet of 4 $\mu\text{L}$  on micro/nanostructured surfaces. In addition, the results show that the scale of the solid–liquid–vapor three phase interface and the amount of evaporation from it increase as the initial contact angle decreases and the droplet volume increases. It was further shown that the contribution of the solid–liquid–vapor three phase interface to the droplet evaporation is 16-48%, and it was clarified that the evaporation from solid–liquid–vapor three phase interface cannot be ignored for micro/nanostructured surfaces.

We have found that the arrangement of droplets, such as the number, size and spacing of adjacent droplets, significantly affects the evaporation of the reference droplets. The

evaporation rate of a reference droplet in the array decreases monotonically as the number of adjacent droplets increases, and this suppression effect decreases as the distance between adjacent droplets increases. We found that the adjacent droplets do not affect the evaporation of the reference droplet if the size of the adjacent droplets is sufficiently smaller than that of the reference droplet.

It was also shown that the reference droplets surrounded by adjacent droplet arrays are inhibited from evaporating due to synergistic effects such as arrangement of adjacent droplets and interfacial wettability. We developed a model involving a contact angle function to accurately predict the evaporation rate of reference droplets on flat surfaces with an arbitrary contact angle in the array. We demonstrate that the contact angle function introduced in the present model should not be ignored when predicting the evaporation rates of reference droplets in an array on hydrophobic surfaces.

The results obtained in this research are expected to deepen our understanding of droplet evaporation phenomena on solid surfaces and can be applied in a wide range of scientific and engineering fields such as inkjet printing systems and bio-measurement.

**Keywords:** Diffusion, Droplet, Evaporation, Wetting, Liquid–vapor interface, Solid–liquid–vapor interface, Array, Adjacent droplets.

# Contents

<b>Contents</b> .....	<b>I</b>
<b>Abbreviations and Symbols</b> .....	<b>IV</b>
<b>1 Introduction</b> .....	<b>1</b>
1.1 Background of droplet evaporation .....	1
1.1.1 Interfacial tension and surface wettability .....	2
1.1.2 Evaporation modes.....	4
1.1.3 Vapor transport in the gas phase.....	6
1.1.4 Flow inside the droplet.....	8
1.1.5 Solid–liquid interface .....	9
1.1.6 Liquid–vapor interface and evaporation cooling .....	10
1.2 Recent problems in droplet evaporation .....	11
1.2.1 Solid–liquid–vapor Interface.....	11
1.2.2 Evaporation of droplet array .....	14
1.3 Research objectives.....	17
1.4 Outline.....	18
<b>2 Contribution of solid–liquid–vapor interface to droplet evaporation ..</b>	<b>15</b>
2.1 Introduction.....	15
2.2 Problem definition .....	16
2.3 Theoretical modeling of droplet evaporation.....	17
2.4 Materials and methods .....	24

2.4.1	Sample preparation and characterization .....	24
2.4.2	Measurement method .....	30
2.5	Results and discussion .....	32
2.5.1	Evaporation dynamics .....	32
2.5.2	Comparison between theory and experiments .....	34
2.5.3	Estimation of slv interface scale and its contribution to droplet evaporation.....	36
2.5.4	Effect of droplet volume on the scale and evaporation rate at the slv interface.....	40
2.6	Summary .....	43
<b>3</b>	<b>Contribution of adjacent droplets to droplet evaporation .....</b>	<b>44</b>
3.1	Introduction.....	44
3.2	Effect of array configuration on droplet evaporation.....	46
3.2.1	Problem definition.....	46
3.2.2	Simulation system .....	47
3.2.3	Experimental materials and methods .....	49
3.2.4	Results and discussion.....	52
3.3	Effect of surface wettability on evaporation rate of droplet array .....	65
3.3.1	Problem definition and theoretical modeling .....	65
3.3.2	Result and discussion .....	68
3.4	Summary .....	76
<b>4</b>	<b>Conclusions and outlook .....</b>	<b>78</b>
4.1	Conclusions.....	78

4.2 Outlook .....	79
<b>Reference .....</b>	<b>81</b>
<b>Acknowledgements.....</b>	<b>94</b>
<b>Research Achievements .....</b>	<b>96</b>

## Abbreviations and Symbols

$\dot{m}$	evaporation rate, $\text{kg s}^{-1}$
$V$	volume, L
$\theta$	contact angle, $^{\circ}$
$R_d$	contact radius, m
$C$	concentration, $\text{kg m}^{-3}$
$\rho$	density, $\text{kg m}^{-3}$
$P$	pressure, $\text{N m}^{-2}$
$T$	temperature, $^{\circ}\text{C}$
$RH$	relative humidity, %
$D$	diffusion coefficient, $\text{m}^2 \text{s}^{-1}$
$M$	vapor molecular weight, $\text{kg mol}^{-1}$
$A$	surface area, $\text{m}^2$
$t$	time, s
$Ra$	surface roughness average, m
$R_g$	universal gas constant, $\text{J mol}^{-1} \text{K}^{-1}$
$MS$	microstructured surface
$FS$	flat surface
$D_s$	center to center distance between droplets, m
$n$	number of adjacent droplets
$N$	total number of droplets
$d_s$	separation distance, m



$f(\theta)$  contact angle function

*Greek symbols*

$\nabla$  gradient,  $\text{m}^{-1}$

$\delta$  scale, m

*Subscripts*

$slv$  solid–liquid–vapor interface

$lv$  liquid–vapor interface

$ev$  total evaporation from droplet

$0$  initial value

$0,0$  initial value at time 0 s

$CCR$  constant contact radius

$CCA$  constant contact angle

$s$  surface

$\infty$  ambient

$sat$  saturated

$l$  liquid

$v$  vapor

$o$  reference droplet

$n$  adjacent droplet

$iso$  isolated droplet

$d$  droplet

<i>th</i>	theoretical
<i>num</i>	numerical
<i>k</i>	given droplet in array

## Chapter 1

# 1 Introduction

## 1.1 Background of droplet evaporation

The evaporation of droplets is a subject of ever-growing interest due to its important role in many industrial, scientific, and medical applications [1–10]. Irving Langmuir pioneered the field in the early 20th century and established fundamental theories for the prediction of the evaporation rates for stationary droplets suspended in ambient air [11].

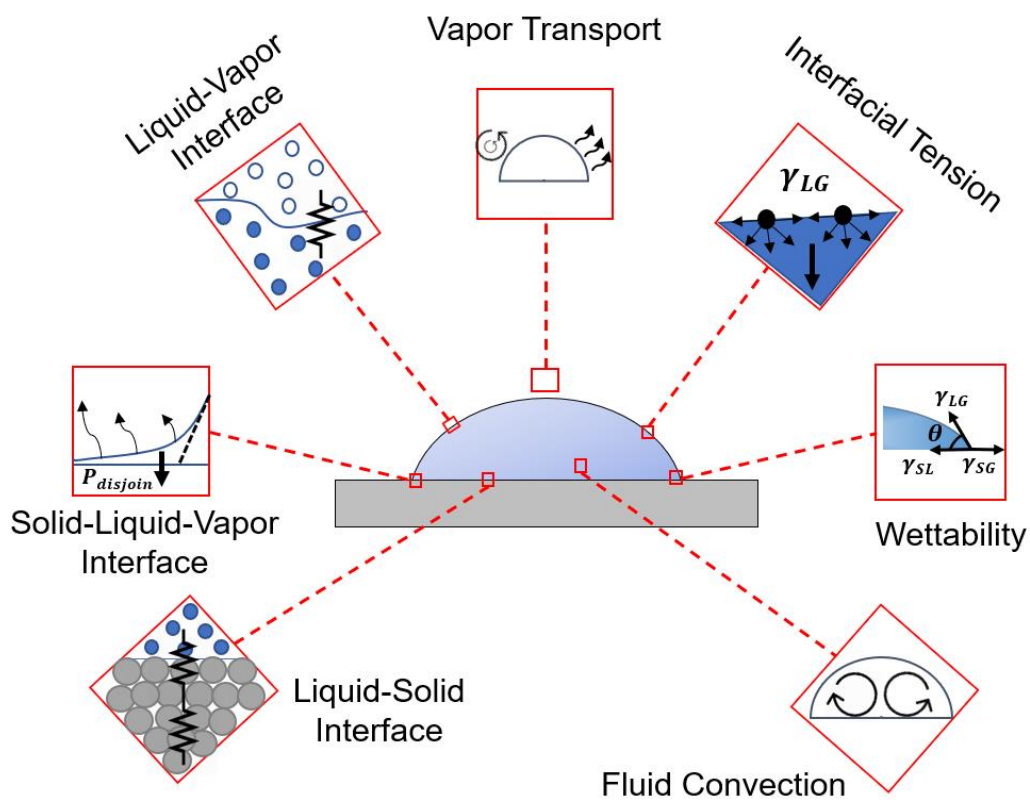


**Fig. 1.1** Background of the droplet evaporation.

At first glance, it seems like a common phenomenon where a few vapor molecules leave the surface of the liquid and enter the nearby air. However, this phenomenon is a complex multidisciplinary problem that is not limited to fluid mechanics, heat transport, physical chemistry, etc. The fundamental background of droplet evaporation is illustrated in Fig. 1.1, that summarizes numerous governing aspects as: (1) vapor transport in the gas domain, (2) liquid convection within the droplet, wettability, droplet scale, surface tension, liquid–vapor interface, solid–liquid interface, solid–liquid–vapor interface, etc. With the advancement in the field of micro/nano scale engineering, the above aspects have been recently studied rigorously to further improve the fundamental understanding about their governing role in droplet evaporation.

### **1.1.1 Interfacial tension and surface wettability**

At the macroscopic scale, the interface between liquid and vapor is considered a sharp boundary[12]. However, on the microscopic scale, there is a transition region between liquid and vapor phases, the thickness of which depends on the temperature [13]. In the liquid phase, there are isotropic intermolecular interactions such as van der Waals forces or hydrogen bonds. However, in the transition region, free liquid molecules are attracted from the vapor phase, leading to anisotropic intermolecular interactions. This leads to a tension in the direction of the transition region, which is called the interfacial tension or surface tension. The surface tension depends on the type of fluid as well as temperature and pressure conditions. Energy minimization occurs due to surface tension to form a spherical droplet in air. However, for a droplet wetted on a solid surface, equilibrium is established between the three forces, as shown in Fig.

1.2(a). These forces exist at the apparent contact line of the droplet between the liquid-vapor, solid-liquid, and solid-vapor phases. These stresses can be characterized by the contact angle of the droplet.

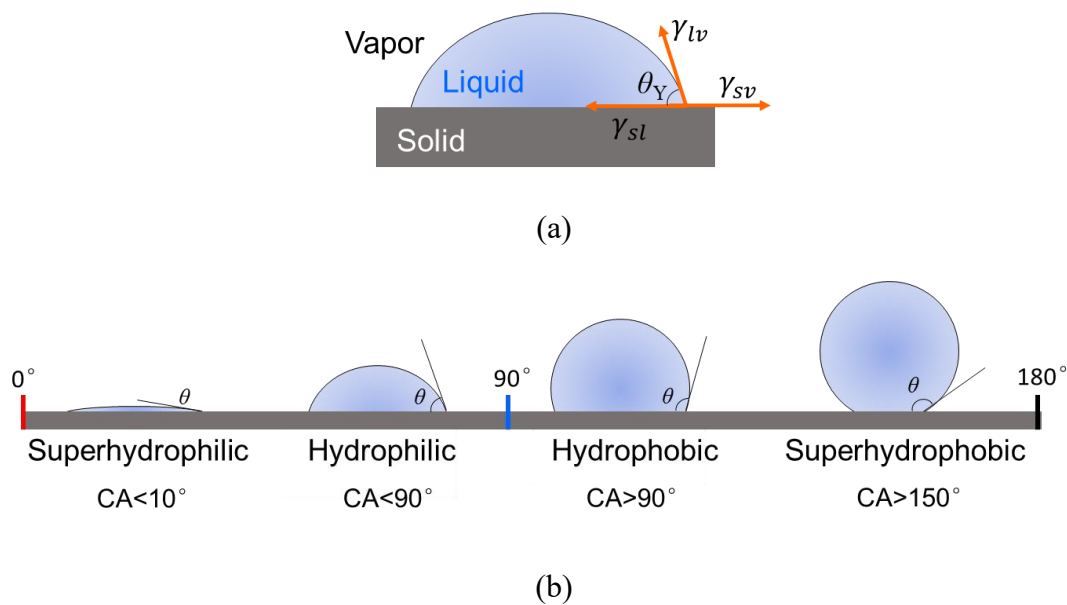


**Fig. 1.2** Schematic illustration of surface wettability (a) interfacial tensions (b) contact angle.

The contact angle depends on the chemical composition of the surface, the surface tension of the liquid and the morphology of the surface as shown in Fig. 1.2(b) [14]. For a flat surface, the water contact angle of the droplet on the surface only depends on the chemical composition of the surface and is called the young contact angle [15]. The young contact angle is measured with an optical microscope on a perfectly flat surface. However, on a microstructured surface, the apparent contact angle of a droplet is different from the young contact angle and depends on both the chemical composition of the surface and the geometric morphology of the structures. The wettability of structured surfaces is related to their wetting state, which is determined by the ratio of the wetting area to the total solid surface under the droplet. There are three wetting

states, commonly referred to as wetting, non-wetting and partially wetting, as shown in Fig. 1.3[16]. The Cassie-Baxter state, which is a non-wetting state, corresponds to the minimum solid–liquid contact area under the droplet[17]. In contrast, the Wenzel model, which is in a fully wetting state, has the maximum solid-liquid contact area under the droplet[18]. Recently, a partial wetting model has been proposed for an intermediate state between the Cassie-Baxter and Wenzel states[19]. The wettability of the droplet on the surface will decide the mode of the droplet evaporation and is of particular importance in understanding the pinning and depinning mechanics during droplet evaporation[20].

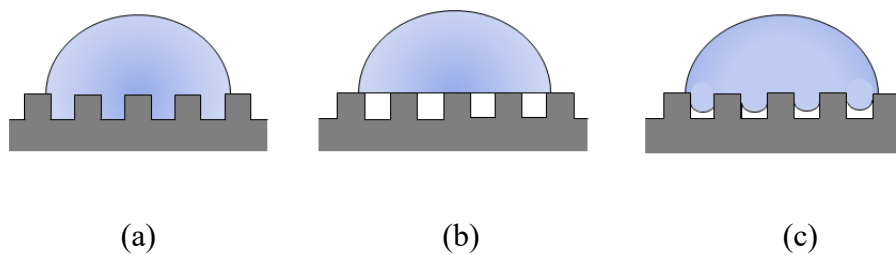


**Fig. 1.3** The wetting states of droplet at the micro/nano structured surface. (a) fully wetting state, (b) non-wetting state, and (c) partial wetting state.

### 1.1.2 Evaporation modes

It is important to understand the different types of evaporation to determine the life of a drop [21]. The instantaneous volume of the droplet is calculated with the contact radius and the contact angle at given time. Therefore, the decrease in droplet volume during evaporation depends on either the decrease in contact radius or contact angle or both simultaneously [22]. The way in which the volume of the droplet changes during evaporation is called the evaporation mode. Based on these assumptions, Picknett and

Bexon proposed two basic evaporation modes, namely constant contact radius (CCR) mode and constant contact angle (CCA) mode, as shown in Fig.1.4 [23].

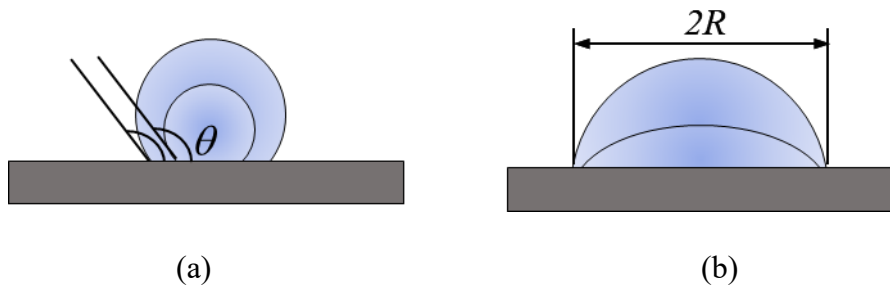


**Fig. 1.4** Modes of droplet evaporation (a) constant contact angle mode and (b) constant contact radius mode.

In the CCR mode of droplet evaporation, the contact radius remains constant during droplet evaporation, but at the expense of a reduction in the contact angle [24]. In the CCA mode of droplet evaporation, on the other hand, the contact radius decreases while the contact angle remains the same [25]. In addition to the two basic evaporation modes, there is a third mode called mixed mode. In mixing mode, both the contact angle and the contact radius of the droplet decrease. The droplet that is wetted on the flat surface evaporates in all three evaporation modes. However, for the hydrophilic case, where the young contact angle is less than 90 degrees, the CCR mode is the dominant mode among all three evaporation modes. However, for hydrophobic surfaces, the CCA mode is the dominant evaporation mode. For microstructured surfaces, the contact line of the droplet is fixed, and the droplet evaporates completely in the CCR mode of evaporation.

### 1.1.3 Vapor transport in the gas phase

Vapor transport around the droplet is important for understanding the evaporation [26]. There are two modes of vapor transportation around the droplet during evaporation known as diffusion and convection as shown in Fig. 1.5 [27]. The primary mode of the vapor transport from the droplet is diffusion of vapor from the liquid–vapor (lv) interface to the ambient air in the gas phase. In diffusion, the air at the liquid vapor interface is saturated with the vapor and is less saturated far from the droplet characterized by relative humidity of the air. The density difference of vapor is the driving force for the vapor transportation in the gas phase through diffusion. When the relative humidity of the ambient air at ambient temperature is less than 1, the number of liquid molecules leaving the lv interface of the droplet is greater than the number of vapor molecules condensing back into the droplet. According to the kinetic theory of evaporation, the net transfer of liquid molecules to the air leads to a reduction in droplet volume. This mass loss over time can be characterized by the evaporation rate of the droplet. The vapor transportation in diffusion has been extensively understood with theoretical models, numerical simulations, and experiments.

However, in addition to diffusion, outward flow is generated to assist evaporation from the droplet, due to the change in density of the air at the interface and far from the droplet [28]. These flows are referred to in the literature as buoyant convection. For the droplets evaporating on the heated substrate and alcohol droplets evaporating in the ambient environment, the buoyant convection is particularly important in addition to the diffusion [4]. Kelly–Zion et al. have recently shown with experiments that the vapor



distribution around the evaporating droplet is largely different from that calculated from the widely accepted diffusion-limited models [29].

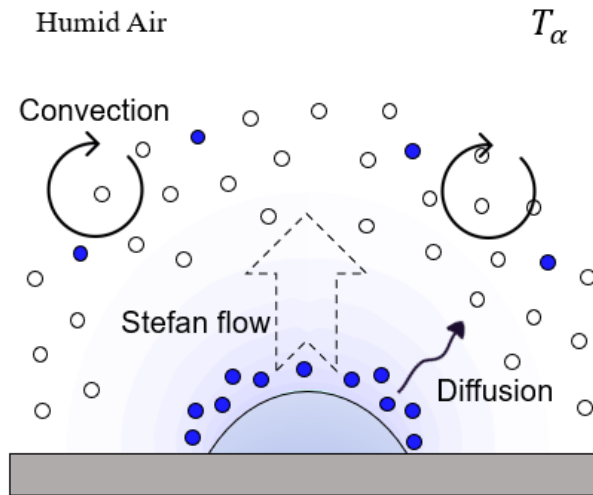


**Fig. 1.5** Vapor transport mechanism in the humid air surrounded by an evaporating droplet.

It was found that the isotropic vapor density gradient around the drop is no longer valid under certain experimental conditions. For alcohol droplets evaporating on flat surfaces in the environment, the evaporation rate with the diffusion-limited model will underestimate the results of the experiments. Therefore, new models have been developed to address this problem and to complement the mass transfer rate predicted by the diffusion model, especially from the combustion community. The Spalding evaporation model is the basic model that accounts for part of the side stream convection (Stefan flow) in addition to the diffusion flow [30]. Recently, new models have been proposed to predict the diffusive and convective contribution of vapor transport during evaporation, but their application is limited to certain fluids [31].

### 1.1.4 Flow inside the droplet

There are three types of internal flows inside the droplet during evaporation, namely evaporation-induced flows, buoyant convection and thermocapillary convection, as shown in Fig. 1.6. The net internal flows result from competition between the above. The evaporation-induced flows, first proposed by Deegan et al [32,33], occur in the direction of the apparent contact line on the side of the bulk of a pinned evaporating droplet. This is because the evaporation rate at the apparent contact line is higher than at the top of the droplet[34]. Due to this mechanism, a radially outward flow is created to compensate for the liquid at the contact line. Due to the evaporation-induced flows, the particles or impurities inside the drop accumulate at the contact line, which is shown in the 'coffee ring effect'.

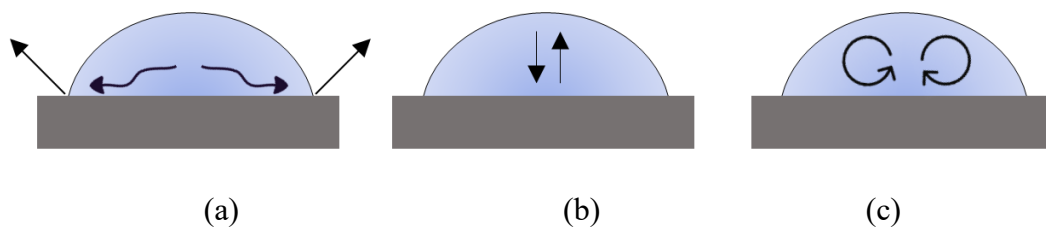


**Fig. 1.6** The flow inside the droplet. (a) evaporation induced flow, (b) buoyant convection, and (c) thermo-capillary convection.

Buoyant convection takes place due to the temperature and density gradient across the height of the drop [35]. Buoyant convection is important for large droplets evaporating on heat carriers or for alcohol droplets under ambient conditions. The contribution of side convection can be characterized by the Rayleigh number [35]. The surface temperature at the interface of the drop is non-uniform, which also leads to surface tension gradients [36]. The result is a thermocapillary flow from warmer regions,

where the surface tension is lower, to colder regions[37]. Thermocapillary flow was first observed by Marangoni and is therefore characterized by the Marangoni number[6,38]. For small water droplets evaporating on flat surfaces in ambient conditions, buoyant convection and thermocapillary convection are negligible[38]. In this case, their effect on the evaporation rate of the droplet can be ignored.

### 1.1.5 Solid–liquid interface

Thermal transport at the solid–liquid (sl) interface is important in governing heat transfer inside that is coupled to evaporation. On a microscopic scale, a discontinuity in temperature exists at sl interface and the temperature changes abruptly at the interface due to the significantly different thermal properties between solid and liquid as shown in Fig. 1.7. This temperature jump will cause additional resistance to the fluid flow in addition to the droplet and solid surface and is characterized by Kapitza length  $l_k$ . In recent years, the chemical and physical properties of the slv interface have been modified to control the interfacial thermal resistance based on experiments and simulations.

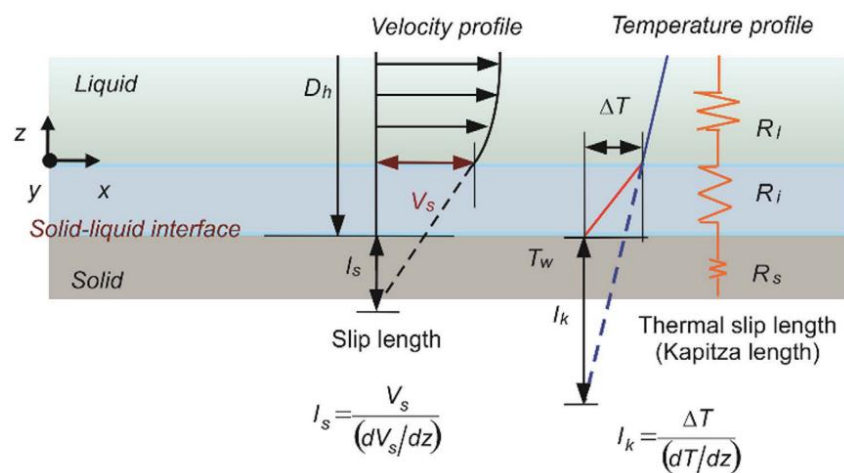


**Fig. 1.7** Description of solid–liquid interface and thermal slip length [39].

Recent studies concluded that for tiny droplets evaporating on heat surfaces, the contribution of this interface is significant as the Kapitza length,  $l_k$  become equal to the droplet size. Nagayama et al., has measured the Kapitza length of Si water system inside microchannel cooling problem [39]. However, the direct experimental measurements of thermal transport in nanoscale systems are still challenging for a droplet evaporation problem.

### **1.1.6 Liquid–vapor interface and evaporation cooling**

The understanding of heat and mass transport at the liquid–vapor (lv) interface is important because evaporation occurs at lv interface [40]. On the macroscopic scale, the lv interface exists when the same molecules are present on the bulk side of the liquid and vapor phases. However, at the microscopic scale, the liquid-vapor interface is typically a few molecular diameters thick, as shown in Fig. 1.8. There is a transition region between the liquid and vapor phases that determines the evaporation mechanism [41]. Evaporation at the liquid interface is well described by the kinetic theory of evaporation, which includes the evaporation coefficient. The evaporation coefficient describes the net mass transfer from the lv interface, and its value shows that all molecules leaving the interphase do not condense back, which is the case of perfect evaporation. The evaporation coefficient is difficult to measure experimentally and is usually calculated using molecular dynamics simulations. Recently, numerous studies have approximated the evaporation coefficient, which is called the accommodation coefficient for droplet evaporation.

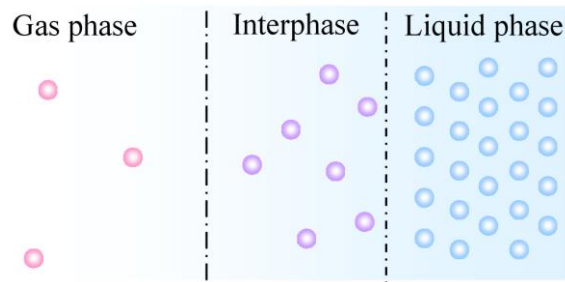


**Fig. 1.8** Microscopic illustration of the liquid-vapor interface [42].

The lv interface of the drop is cooled by the latent heat of absorption generated by the phase change between liquid and vapor [43]. Evaporative cooling reduces the temperature of the lv interface relative to that of the wall, creating temperature gradients that drive heat transfer in the solid, liquid, and gaseous phases. Evaporative cooling at the lv interface depends on the wettability, the size of the droplets, the type of solid and liquid, and the boundary conditions at the solid surface [44]. Pan et al. found that evaporative cooling at the superhydrophobic surface is intense for water droplets evaporating under ambient conditions [45]. For water droplets evaporating on hydrophobic surfaces, the effects can be neglected. F. G. H. Schofield al. also found that evaporative cooling is very strong for substrates with low thermal conductivity [46]. For organic liquids like alcohols, evaporative cooling is much more intense compared to water [47].

## 1.2 Recent problems in droplet evaporation

### 1.2.1 Solid–liquid–vapor Interface

The solid–liquid–vapor (slv) interface is of particular interest because it is believed to be the main contributor toward droplet evaporation [48]. An slv interface is often

referred to as a three-phase contact line [49], static puddle [50], contact region [51], wetting meniscus [52], thin film [53], or precursor film [54]. However, its underlying physics still corresponds to that of a nearly flat thin liquid film with a thickness ranging from 10 nm to a few micrometers, extending ahead of the macroscopic contact line of the droplet formed as shown in Fig. 1.9, owing to a capillary and disjoining pressure gradient [55]. The formation mechanism and physical stability of the slv interface of an evaporating droplet have been extensively studied using theoretical models [56]. Pham et al. presented a theoretical model to determine the scale of the slv interface of an evaporating droplet [57]. However, in their model, both the scale and the evaporation rate at the slv interface are unknown; and the model can only be applied to fully wetted evaporating droplets. The scales of the slv interfaces of droplets wetted on flat surfaces have been experimentally investigated using scanning electron microscopy [58], laser interferometry [59], nanoparticle image velocimetry [60], atomic force microscopy [61], and reflection interference contrast microscopy [62].

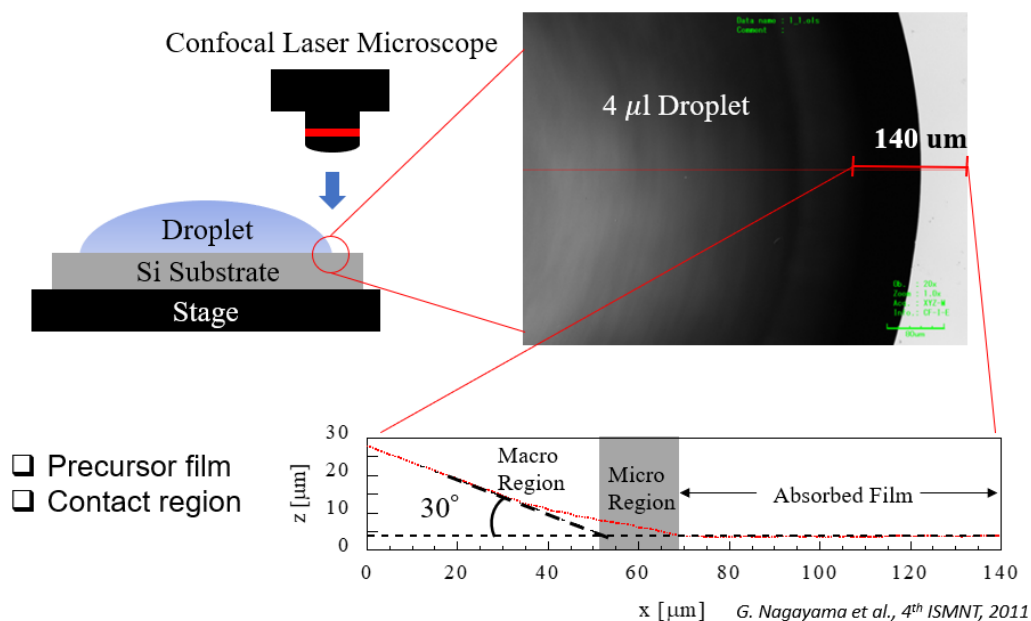


**Fig. 1.9** Confocal laser microscope image of solid-liquid-vapor interface of water droplet on silicon surface [63].

The contribution of the slv interface in the kinetically driven evaporation of a droplet, where the temperature difference between the wall and the pure vapor in the vicinity is the driving force, has been extensively studied and has been reported to be significantly high [64]. This is because the thermal resistance at the slv interface is lower compared with that at the liquid–vapor (lv) interface, which promotes droplet evaporation [65]. In contrast, in diffusion-driven droplet evaporation, both the slv and lv interfaces are in thermodynamic equilibrium with the ambient air. The vapor concentration gradients at the slv and lv interfaces drive droplet evaporation, which depends on the surface area of each interface [66]. In this case, increasing the scale of the slv interface is one of the most efficient methods for enhancing droplet evaporation [67]. A previous study found the slv interface of an n-octane meniscus on a flat Si surface to be  $\sim 10\ \mu\text{m}$ , whereas that of the lv interface was on the order of millimeters [68]. In a similar experiment, the scale of the slv interface of a water droplet wetted on a flat Si surface was experimentally measured and found to be negligible compared to the contact radius of the droplet [58,61]. Therefore, as the lv interface plays a dominant role and the slv interface makes little contribution. A good agreement has been observed between theoretical and experimental results when predicting droplet evaporation rates on flat surfaces [22,69–71].

Recently, researchers have proposed that the scale of the slv interfaces of a droplet can be artificially increased by growing micro/nanostructures on flat surfaces [55,72,73]. When a droplet is wetted on such a micro/nanostructured surface, the liquid spreads

owing to the capillary and the disjoining pressure gradient near the macroscopic contact line. Simultaneously, liquid wicking occurs within the micro/nanostructure [74]. This coupled spreading and wicking artificially increases the scale of the slv interface. For example, Chen et al. fabricated Zn oxide nanowires and porous Cu structures and observed an enlarged slv interface whose scale was dependent on the geometrical morphology of the micro/nanostructure [67]. Moreover, the slv interface on an irregularly nanostructured ZnO nanowire surface was larger than that on a regularly microstructured porous Cu surface. Shiimoto et al. [55] and Gimenez et al. [73] developed porous thin films on flat surfaces and observed the formation of large slv interfaces around droplets. They reported that an internal flow between the slv and lv interfaces occurred owing to wicking during droplet deposition. Furthermore, Poudel et al. fabricated regularly patterned microporous nanochannels at Si surface; they reported that significant wicking and evaporation occurred in the vicinity of the droplet's contact line inside the nanochannels through the micropores on the surface [72].

However, thus far, details regarding the relative contribution of the slv interface to that of the lv interface for droplet evaporation at micro/nanostructured surfaces have not been reported. In particular, the relationships between the contributions of the slv interface, surface wettability, and droplet volume of droplet evaporating at micro/nanostructured surfaces warrant in-depth evaluations.

### 1.2.2 Evaporation of droplet array

The droplet arrays not only have attention in wide range of practical scientific and engineering applications but also can be found in our everyday life as shown in Fig.

1.10. The presence of adjacent droplets around an evaporating droplet in array at a solid

*Graduate School of Engineering, Kyushu Institute of Technology, Japan*



surface increases vapor accumulation in the vicinity of liquid-vapor interface. This vapor accumulation referred to as shielding effect will suppress the evaporation rate of a droplet in array as compared to an isolated droplet under the same conditions.



**Fig. 1.10** Droplet array on the glass windows.

Extensive recent studies have been conducted to understand the evaporation rate of a droplet in array. The presence of adjacent droplets has been shown to change the internal flow structure, induce convection in vapor phase, influence the shape of the final deposits and result in shrinking final morphologies of the evaporating droplet being surrounded in array. Chen et al. found that the evaporation lifetime for an arrayed droplet prolongs compared to its isolated state even with large droplet spacing in an ordered array [75]. Khilifi et al. found that evaporation rate of droplets can be reduced by almost 55% compared to isolated droplets when the droplets are close enough [76]. Pardhan et al. analyzed the dissolution of binary droplets for both single and adjacent droplets at room temperature [77]. They reported that the adjacent droplets influenced the evaporative heat flux of each other, and as the distance of the droplets increased, the droplets tended to show the behavior of a single droplet. Edward et al. used laser interferometric technique to measure simultaneously the suppression in evaporation rate of all droplets in ordered and random two-dimensional array and found no evidence of

convection and thermal interactions [78]. Pandey et al. studied the extend of droplet confinement with various designs of two-dimensional array of evaporating droplets [79]. They found that the droplet lifetime in the array is remarkably independent of the relative position of the adjacent droplet and asymmetric nature of the droplet array. Laghezza et al. demonstrate the effect of the array size on the evaporation time of droplets in the center of the array [80]. They reported that evaporation time of the droplet in the center of the large size array increases as much as 60% compared to isolated droplets under identical conditions due to the shielding effect by adjacent droplets. However, for a small size array, no significant increase of the evaporation time was reported.

Although these studies have aimed in fundamental conceptualization of physical phenomenon that involve an increase in evaporation time of a droplet surrounded by adjacent droplets during evaporation. However, little is known about the explicit significance of the physical parameters of the adjacent droplets on the evaporation rate of the droplet in center of the array. As an isolated droplet evaporates in three modes; the constant contact radius (CCR), the constant contact angle (CCA) and mix modes depending on the surface and liquid properties. However, the presence of the adjacent droplet will alter the time that a droplet spends in each mode during droplet evaporation in array and will be influenced by the physical parameters of the adjacent droplets. The effect of the configuration of adjacent droplets on the evaporation dynamics and mode of evaporation of a droplet in array is not yet fully understood. Further, existing theoretical models for predicting the evaporation rate of droplets in the array neglect the important factor of surface wettability.

### 1.3 Research objectives

Evaporation of a single droplet on a flat surface has been studied extensively and it is well-known that the liquid–vapor (lv) interface dominates droplet evaporation kinetics. However, in practice, droplets may evaporate on a micro/nanostructured surface or be surrounded by adjacent droplets. In the former case, the solid–liquid–vapor (slv) interface formed in the vicinity of the macroscopic contact line becomes significant, while the contribution of the slv interface to droplet evaporation remains an open question. In the latter case, existing theoretical models neglected the important factor of surface wettability and thus the synergistic effects of adjacent droplet’s configuration and surface wettability on droplet evaporation in an array is still unknown. The main objectives of this thesis are described as follows:

- (1) To estimate the scale of slv interface and its contributions to the droplet evaporation.
- (2) To clarify the effects of the surface wettability and droplet volume on the scale and evaporation at slv interface.
- (3) To investigate the contribution of adjacent droplets to droplet evaporation in array.
- (4) To clarify the effect of surface wettability on the evaporation rate of the droplet array.

Upon completing these objectives, we look forward to understanding the physical mechanism of droplet evaporation in a wide range of applications.

## 1.4 Outline

In this thesis, we proposed a new methodology to estimate the droplet evaporation rate from the slv interface and the physical scale of the slv interface for a wide range of surface wettability. We found that contribution of the slv interface to droplet evaporation was more significant than that of the lv interface at micro/nanostructured surfaces. We also conducted numerical simulations and experiments to verify a model involving the synergistic effects of droplet configuration and surface wettability on droplet evaporation in an array. We verified our model and found the evaporation from the lv interface with adjacent droplets was suppressed due to vapor-mediated interactions between the droplets. The rest of thesis consists of the following three chapters:

Chapter 2, Contribution of solid–liquid–vapor interface to droplet evaporation estimates the evaporation rate at the slv interface of a droplet on a microstructured surface, based on the difference between the theoretical evaporation rate at the lv interface and the experimental evaporation rate. The scale of slv interface and its contributions to the droplet evaporation were estimated, and the effects of the surface wettability and droplet volume were clarified.

Chapter 3, Contribution of adjacent droplets to droplet evaporation describes how droplet evaporation is hindered by the presence of adjacent droplets due to vapor-mediated interactions. The contribution of the adjacent droplets to droplet evaporation was realized through theoretical modeling, numerical simulations, and experiments. Section 3.1 explains the effect of array configuration on droplet evaporation by varying the number, size, and spacing of adjacent droplets relative to a single reference droplet. In section 3.2, we clarified the effect of surface wettability on the evaporation rate of the

droplet array. We developed a model involving a contact angle function to accurately predict the evaporation rate of droplets on flat surfaces with an arbitrary contact angle in the array. We demonstrate that the contact angle function introduced in the present model should not be ignored when predicting the evaporation rates of droplets in an array on hydrophobic surfaces.

Chapter 4 summarizes the main findings of this thesis and discusses future work.

## **Chapter 2**

# **2 Contribution of solid–liquid–vapor interface to droplet evaporation**

## **2.1 Introduction**

A solid–liquid–vapor (slv) interface is formed by a capillary and disjoining pressure gradient near the macroscopic contact line of a droplet. At a micro/nanostructured surface, the scale of the slv interface increases, such that it can significantly contribute toward droplet evaporation. However, the relative contribution of the slv interface to that of the lv interface for droplet evaporation at micro/nanostructured surfaces have not been reported. In particular, the relationships between the contributions of the slv interface, surface wettability, and droplet volume of droplet evaporating at micro/nanostructured surfaces warrant in-depth evaluations. Therefore, the wettability of the micro/nanostructured surface and droplet volume may affect this contribution and warrant further clarification. In this chapter, the evaporation rate of a droplet at a macroscopic liquid–vapor (lv) interface was derived theoretically and that at fabricated surfaces was measured experimentally. Considering droplet mass conservation, the evaporation rate at the slv interface was estimated based on the difference between the experimental results and theoretical evaporation rate at the lv interface. The corresponding scale of the slv interface was estimated and further validated with experiments. Further, the effects of the surface wettability and droplet volume on the scale and evaporation at slv interface is clarified.

## 2.2 Problem definition

A droplet with an initial volume  $V_0$ , a contact radius  $R_{d0}$ , and a contact angle  $\theta_0$  is considered to evaporate at a solid surface under isothermal ambient conditions. There are two interfaces for the possible evaporation of the droplet: the lv and slv interfaces. Diffusion-driven droplet evaporation is the governing mechanism, where the evaporation rates depend on the scale of the slv and lv interfaces. The scale  $\delta_{slv}$  has been found to be negligible compared to  $R_{d0}$  for a flat surface through experiments [58,61]; therefore, its contribution to droplet evaporation is smaller. This has been confirmed by the good agreement between experimental and theoretical results during prediction of the evaporation rate at the lv interface [22,69–71]. Therefore, the lv interface dominates droplet evaporation at flat surfaces. However, in case of a structured surface, the scale  $\delta_{slv}$  of the slv interface has been found to be significantly enlarged [67,74]; thus, the slv interface may contribute more toward droplet evaporation, warranting further investigation.

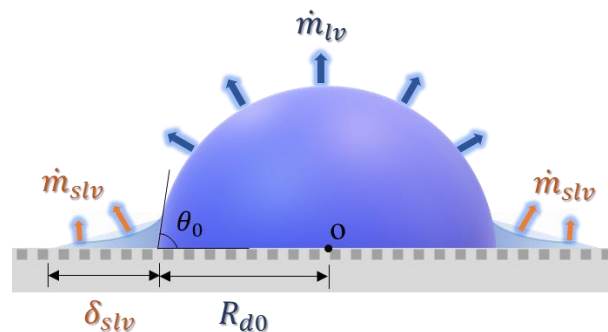


**Fig. 2.1** Schematic of sessile droplet evaporating from lv and slv interfaces on a structured surface from an initial state.

A model is proposed in Eq. (2-1) and illustrated in Fig. 2.1, where the total evaporation rate  $\dot{m}_{ev}$  of a droplet at a structured surface comprises the evaporation rates at the lv and slv interfaces, i.e.,  $\dot{m}_{lv}$  and  $\dot{m}_{slv}$ , respectively.

$$\dot{m}_{ev} = \dot{m}_{lv} + \dot{m}_{slv} \quad (2-1)$$

In this model,  $\dot{m}_{ev}$  is measured experimentally,  $\dot{m}_{lv}$  is obtained theoretically, and  $\dot{m}_{slv}$  is estimated from the difference between  $\dot{m}_{ev}$  and  $\dot{m}_{lv}$ .

### 2.3 Theoretical modeling of droplet evaporation

There are three types of internal flows during droplet evaporation: (1) Marangoni flow due to the surface tension gradient, (2) buoyant convection due to gravity, temperature gradient etc., and (3) the Deegan flow [32] due to the capillary and disjoining pressure gradient [48,49]. Since we used pure water as the working fluid for a 1-4  $\mu\text{l}$  droplet, the Marangoni number can be estimated to be lower than  $10^{-4}$ , and the Rayleigh number is much lower than  $10^{-1}$ . Hence, we can ignore both the Marangoni flow and the buoyant convection in the present study [35]. On the other hand, the Deegan flow is of importance to keep the mass conservation during droplet evaporation as the mass transport rate of the Deegan flow is equal to evaporation rate  $\dot{m}_{slv}$  at the slv interface. The following assumptions were used for the derivation of  $\dot{m}_{lv}$ :

- (1) The droplets are sufficiently small to be not affected by gravity as  $R_{d0} < 3\text{mm}$ , which is less than the capillary length [21].
- (2) The governing mechanism for evaporation from the lv interface is limited to diffusion, and gas-phase convection can be ignored as the Rayleigh number for vapor is estimated less than 12 [81].



(3) Evaporative cooling at the lv interface, caused by latent heat transfer, has a negligible influence on the evaporation rate [45].

(4) Evaporation under isothermal ambient conditions occurs in a quasi-steady state because the ratio of the diffusion time to the evaporation time is considerably smaller than 1 ( $t^* = \frac{c_s - c_\infty}{\rho_v} < 1$ ) [70].

For the boundary condition at the lv interface of an evaporating droplet, pure vapor is assumed at the lv interface, which is in saturation with a concentration corresponding to the vapor-saturated density:

$$C_s = \frac{MP_{sat}(T)}{R_g T}, \quad (2-2)$$

where  $P_s(T)$  is the saturated partial vapor pressure at ambient temperature  $T$ ,  $M$  is the molecular weight of the vapor, and  $R_g$  is the universal gas constant. The boundary condition far from the lv interface corresponds to the ambient air–vapor mixture under relative humidity  $RH$ , with concentration  $C_\infty = RH \times C_s$  [70]. The Laplace equation can be used to determine the vapor transport around the droplet under steady-state conditions, i.e.,  $\nabla^2 C = 0$ , where the vapor concentration gradient  $\nabla C$ , which is normal to the lv interface of the droplet, is the driving force for evaporation. The evaporation rate at the lv interface is described by Fick’s law [82]:

$$\dot{m}_{lv} = -DA_{lv}\nabla C, \quad (2-3)$$

where the diffusion coefficient of the vapor into ambient humid air  $D$  is calculated as  $D(T) = 22.5 \times 10^{-6}(T/273.15K)^{1.8}$  [83], and  $A_{lv}$  is the surface area of the lv

interface. The concentration gradient  $\nabla C$  depends on the contact angle  $\theta$  formed by the lv interface and the surface of the droplet [70].

The evaporation rate at the lv interface of a hemispherical droplet of radius  $R_d$  with  $\theta = 90^\circ$  can be calculated using  $A_{lv} = 2\pi R_d^2$  and  $\nabla C = C_s - C_\infty/R_d$  in Eq. (2-3) [11]:

$$\dot{m}_{lv}(R_d, 90^\circ) = -2\pi R_d D(C_s - C_\infty). \quad (2-4)$$

Hu et al. defined the evaporation rate at the lv interface of a droplet with arbitrary  $R_d$  and  $\theta$  using a surface area analogy with a hemispherical droplet, as follows [66]:

$$\dot{m}_{lv}(R_d, \theta) = -2\pi R_d D(C_s - C_\infty) \frac{1}{\sqrt{1 + \cos \theta}}. \quad (2-5)$$

Conversely, the temporal evolution of the lv interface can be obtained as follows:

$$\dot{m}_{lv}(R_d, \theta) = \rho_l \frac{d}{dt} \left[ \frac{\pi R_d^3 (1 - \cos \theta)^2 (2 + \cos \theta)}{3 \sin^3 \theta} \right], \quad (2-6)$$

where  $\rho_l$  denotes the liquid density.

Multiplying and dividing Eq. (2-5) with  $\sqrt{1 - \cos \theta}$  will yield the following:

$$\dot{m}_{lv}(R_d, \theta) = -2\pi R_d D(C_s - C_\infty) \frac{\sqrt{1 - \cos \theta}}{\sin \theta}. \quad (2-7)$$

### CCR mode of evaporation

Considering the CCR mode of evaporation, where  $R_d$  is constant and equal to the initial contact radius  $R_{d0}$ , Eq. (2-6) can be rewritten as

$$\dot{m}_{lv}(R_d, \theta) = \frac{\pi \rho_l R_{d0}^3}{3} \left[ \frac{(1 - \cos \theta)^2 (2 + \cos \theta)}{\sin^3 \theta} \right]' \frac{d\theta}{dt}, \quad (2-8)$$

where we assume that

$$\left[ \frac{(1 - \cos \theta)^2 (2 + \cos \theta)}{\sin^3 \theta} \right]' = \frac{d}{d\theta} \left[ \frac{(1 - \cos \theta)^2 (2 + \cos \theta)}{\sin^3 \theta} \right]. \quad (2-9)$$

The differential on the right side of Eq. (2-9) is solved as

$$\frac{d}{d\theta} \left[ \frac{(1 - \cos \theta)^2 (2 + \cos \theta)}{\sin^3 \theta} \right] = \frac{3}{(1 + \cos \theta)^2}. \quad (4-10)$$

The evaporation rate in Eq. (2-8) is written as

$$\dot{m}_{lv}(R_d, \theta) = \frac{\pi \rho_l R_{d0}^3}{3} \frac{3}{(1 + \cos \theta)^2} \frac{d\theta}{dt}. \quad (2-11)$$

$$\dot{m}_{lv}(R_d, \theta) = \frac{\pi \rho_l R_{d0}^3}{(1 + \cos \theta)^2} \frac{d\theta}{dt}. \quad (2-12)$$

By equating the evaporation rates calculated using Eq. (2-7) and Eq. (2-12), we obtain

Eq. (7) as follows:

$$\left. \frac{d\theta}{dt} \right|_{CCR} = - \frac{2D(C_s - C_\infty)}{\rho_l R_{d0}^2} \frac{(1 + \cos \theta)^2 \sqrt{1 - \cos \theta}}{\sin \theta}.$$

By separating variables  $\theta$  and  $t$  in Eq. (2-7) and applying definite integrals in the limit

$\theta = \theta_0$  to  $0$  at  $t = 0$  to  $t_{CCR}$  as

$$\int_0^{\theta_0} \frac{\sin \theta}{(1 + \cos \theta)^2 \sqrt{1 - \cos \theta}} d\theta = - \frac{2D(C_s - C_\infty)}{\rho R_{d0}^2} \int_{t_{CCR}}^0 dt. \quad (2-13)$$

The definite integral function on the left side of Eq. (2-13) is substituted with I as

$$I = - \frac{2D(C_s - C_\infty)}{\rho R_{d,s}^2} (0 - t_{CCR}) = \frac{2D(C_s - C_\infty)}{\rho R_{d0}^2} t_{CCR}, \quad (2-14)$$

where

$$I = \int_0^{\theta_0} \frac{\sin \theta}{(1 + \cos \theta)^2 \sqrt{1 - \cos \theta}} d\theta. \quad (2-15)$$

Using substitution method and replacing  $\sqrt{1 - \cos \theta}$  with  $x$  and  $\cos \theta = 1 - x^2$  and  $dx = \frac{\sin \theta}{2\sqrt{1 - \cos \theta}} d\theta$ , the definite integral limits in Eq. (2-15) are replaced with  $0 \rightarrow \sqrt{1 - \cos \theta_0}$  from  $0 \rightarrow \theta_0$  as

$$I = 2 \int_0^{x_0 = \sqrt{1 - \cos \theta_0}} \frac{1}{(\sqrt{2} - x)^2 (\sqrt{2} + x)^2} dx. \quad (2-16)$$

The integrand function is decomposed into partial fractions as

$$\frac{1}{(\sqrt{2} - x)^2 (\sqrt{2} + x)^2} = \frac{A}{\sqrt{2} - x} + \frac{B}{(\sqrt{2} - x)^2} + \frac{C}{\sqrt{2} + x} + \frac{D}{(\sqrt{2} + x)^2}.$$

By taking the respective limits, we can calculate the numerator coefficients as

$$A = \lim_{x \rightarrow \sqrt{2}} \frac{d}{dx} \left( \frac{1}{(\sqrt{2} + x)^2} \right)' = \lim_{x \rightarrow \sqrt{2}} \frac{2}{(\sqrt{2} + x)^3} = \frac{\sqrt{2}}{16}.$$

$$B = \lim_{x \rightarrow \sqrt{2}} \frac{1}{(\sqrt{2} + x)^2} = \frac{1}{8}.$$

$$C = \lim_{x \rightarrow -\sqrt{2}} \frac{d}{dx} \left( \frac{1}{(\sqrt{2} - x)^2} \right)' = \lim_{x \rightarrow -\sqrt{2}} \frac{2}{(\sqrt{2} - x)^3} = \frac{\sqrt{2}}{16}.$$

$$D = \lim_{x \rightarrow -\sqrt{2}} \frac{1}{(\sqrt{2} - x)^2} = \frac{1}{8}.$$

Eq. (2-16) is rewritten as

$$I = 2 \int_0^{\sqrt{1 - \cos \theta_0}} \left[ \frac{\sqrt{2}}{16} \left( \frac{1}{\sqrt{2} - x} + \frac{1}{\sqrt{2} + x} \right) + \frac{1}{8} \left\{ \frac{1}{(\sqrt{2} - x)^2} + \frac{1}{(\sqrt{2} + x)^2} \right\} \right] dx. \quad (2-17)$$

Integrating Eq. (2-17) as

$$I = \left[ \frac{\sqrt{2}}{8} \ln \left( \frac{\sqrt{2} + x}{\sqrt{2} - x} \right) + \frac{x}{2(2 - x^2)} \right]_0^{\sqrt{1 - \cos \theta_0}}. \quad (2-18)$$

By expanding the limits as follows:

$$I = \frac{\sqrt{2}}{8} \ln \left( \frac{\sqrt{2} + \sqrt{1 - \cos \theta_0}}{\sqrt{2} - \sqrt{1 - \cos \theta_0}} \right) + \frac{\sqrt{1 - \cos \theta_0}}{2(1 + \cos \theta_0)}. \quad (2-19)$$

$$I = \frac{\sqrt{2}}{8} \cdot \ln \left( \frac{1 + \frac{\sqrt{1 - \cos \theta_0}}{\sqrt{2}}}{1 - \frac{\sqrt{1 - \cos \theta_0}}{\sqrt{2}}} \right) + \frac{\sqrt{1 - \cos \theta_0}}{2(1 + \cos \theta_0)}. \quad (2-20)$$

Using the trigonometric hyperbolic function,  $\tanh z = \frac{e^{2z} - 1}{e^{2z} + 1} = y$  with  $z = \tanh^{-1} y$  and

$z = \frac{1}{2} \ln \left( \frac{1+y}{1-y} \right)$ . Eq. (2-20) can then be rewritten as

$$I = \frac{\sqrt{2}}{4} \tanh^{-1} \left[ \left( \frac{\sqrt{1 - \cos \theta_0}}{\sqrt{2}} \right) \right] + \frac{\sqrt{1 - \cos \theta_0}}{2(1 + \cos \theta_0)}. \quad (2-21)$$

Using the double angle formula,  $\sin^2 \frac{\theta}{2} = \frac{1 - \cos \theta}{2}$  and  $\cos^2 \frac{\theta}{2} = \frac{1 + \cos \theta}{2}$ , Eq. (2-21) is

rewritten as

$$I = \frac{\sqrt{2}}{4} \tanh^{-1} \left( \sqrt{\sin^2 \frac{\theta_0}{2}} \right) + \frac{\sqrt{2 \sin^2 \frac{\theta_0}{2}}}{2 \cdot 2 \cos^2 \frac{\theta_0}{2}}. \quad (2-22)$$

After simplifying Eq. (2-22),

$$I = \frac{\sqrt{2}}{4} \left[ \tanh^{-1} \left( \sin \frac{\theta_0}{2} \right) + \frac{\tan \frac{\theta_0}{2}}{\cos \frac{\theta_0}{2}} \right]. \quad (2-23)$$

The evaporation time in the CCR mode  $t_{CCR}$  is calculated by back substituting Eq. (2-23) into Eq. (2-14) as

$$t_{CCR} = \frac{\sqrt{2}\rho_l R_{d0}^2}{8D(C_s - C_\infty)} \left[ \tanh^{-1} \left( \sin \frac{\theta_0}{2} \right) + \frac{\tan \frac{\theta_0}{2}}{\cos \frac{\theta_0}{2}} \right]. \quad (2-24)$$

Further simplifications yield

$$t_{CCR} = \frac{\sqrt{2}\rho_l R_{d0}^2}{8D(C_s - C_\infty)} \left\{ \tanh^{-1}[a(\theta_0)] + \frac{a(\theta_0)}{1 - a(\theta_0)^2} \right\}, \quad (2-25)$$

where  $a(\theta_0) = \sin \frac{\theta_0}{2}$ . The evaporation rate at the lv interface in the CCR mode is

$$\dot{m}_{lv}|_{CCR} = -\frac{\rho_l(V_0/1000)}{t_{CCR}} = -\frac{8V_0D(C_s - C_\infty)}{1000 \times \sqrt{2}R_{d0}^2 \left\{ \tanh^{-1}[a(\theta_0)] + \frac{a(\theta_0)}{1 - a(\theta_0)^2} \right\}}$$

#### CCA mode of evaporation

Considering the CCA mode of evaporation, where  $\theta$  is constant and equal to the initial contact angle  $\theta_0$ , Eq. (2-6) can be rewritten as

$$\dot{m}_{lv}(R_d, \theta) = \pi\rho R_d^2 \left[ \frac{(1 - \cos \theta_0)^2(2 + \cos \theta_0)}{\sin^3 \theta_0} \right] \frac{dR_d}{dt}, \quad (2-26)$$

The evaporation rates calculated using Eqs. (2-5) and (2-26) are equated to yield as

$$\left. \frac{dR_d}{dt} \right|_{CCA} = -\frac{2D(C_s - C_\infty)}{\rho_l R_d} \frac{(1 + \cos \theta_0)}{(2 + \cos \theta_0)\sqrt{1 - \cos \theta_0}}.$$

By separating variables  $R_d$  and  $t$  in Eq. (2-8) and applying definite integrals in the limit

$R_d = R_{d0}$  to 0 at  $t = 0$  to  $t_{CCA}$ :

$$\int_0^{R_{d0}} R_d dR_d = -\frac{2D(C_s - C_\infty)}{\rho_l} \frac{(1 + \cos \theta_0)}{(2 + \cos \theta_0)\sqrt{1 - \cos \theta_0}} \int_{t_{CCA}}^0 dt. \quad (2-27)$$

The definite integrals are solved as follows:

$$t_{CCA} = \frac{\rho_l R_{d0}^2}{4D(C_s - C_\infty)} \left\{ \frac{(2 + \cos \theta_0) \sqrt{1 - \cos \theta_0}}{(1 + \cos \theta_0)} \right\}. \quad (2-28)$$

The evaporation rate at the lv interface in the CCA mode is given as

$$\dot{m}_{lv}|_{CCA} = -\frac{\rho_l (V_0/1000)}{t_{CCA}} = -\frac{4V_0 D (C_s - C_\infty)}{1000 \times R_{d0}^2 \left\{ \frac{(2 + \cos \theta_0) \sqrt{1 - \cos \theta_0}}{(1 + \cos \theta_0)} \right\}}. \quad (2-29)$$

Wilson et al. has proposed a model [84] with a complex double integral function for the initial contact angle  $\theta_0$ , which requires numerical integration to predict the evaporation rate at the lv interface. Nevertheless, the present model proposed an algebraic function of the initial contact angle  $\theta_0$ . It can be easily solved without any assumptions to predict the exact evaporation rate corresponding to the experimental conditions.

## 2.4 Materials and methods

### 2.4.1 Sample preparation and characterization

A 18 mm × 18 mm × 1 mm glass sample, denoted as FS-1, was employed in this study. Further, a 15 mm × 15 mm × 0.35 mm Si sample was cut from an n-type Si wafer, and subsequently cleaned with acetone, isopropanol alcohol, and water for 10 min to remove organic impurities. The Si sample was then treated with a diluted piranha solution to obtain FS-2. An oxide layer was deposited on the Si sample through chemical vapor deposition to obtain FS-3. Subsequently, FS-4 was prepared by treating the Si sample with 1% buffered hydrofluoric (BHF) acid to remove the natural oxide layer. To prepare microstructured irregular Cu samples MS-(1–4), wet chemical etching

was employed as shown in Fig. 2.2. The 0.3-mm-thick Cu foil was cut into 15 mm × 15 mm samples. The natural oxide layer was mechanically removed using SiC sandpaper with grit sizes of 600 μm and 1000 μm, in succession. The polishing debris was removed via ultrasonic-assisted chemical cleaning with acetone, isopropanol alcohol, and water for 10 min each. The etchant solution for wet chemical etching was prepared by mixing 2 mol/L HCl with 0.83 mol/L H<sub>2</sub>O<sub>2</sub>. The cleaned and polished Cu samples were immersed in an etchant and maintained at a constant temperature of 60 °C to ensure uniform etching. The etched Cu samples were cleaned with isopropanol alcohol, followed by deionized water, and then air-dried before evaporation. Thus, a porous surface with hierarchical structures was obtained on top of the Cu samples. A similar trend was reported in [85] during the wet chemical etching of Al samples. The surface roughness  $R_a$  of the samples depends on the etching time, provided the concentration of the etchant remains constant. The longer the etching time, the greater is the surface roughness of MS-(1–4), as illustrated in Fig. 2.3(b). Regular microstructured cavities with the surface parameters described in Table 2-2 were fabricated on the flat Si surface. MS-4 was produced using mask-based photolithography and anisotropic KOH wet-etching. MS-(5–7) were developed using maskless lithography (NEOARK, DDB-701-MS) and reactive ion etching (SAMCO, RIE-400iPB) over a 9 mm × 9 mm area as shown in Fig.2.2(b). The correlation between  $\theta_0$  and the structural parameters of the microstructured samples has been previously described by Zhang et al. [86].

A scanning probe microscope (SPM, Shimadzu, SPM-9700HT) and a scanning confocal laser microscope (SCLM, Olympus, LEXT OLS3100) were used to observe the surface morphologies of the flat and microstructured samples, respectively. Detailed

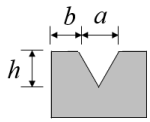
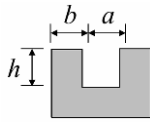


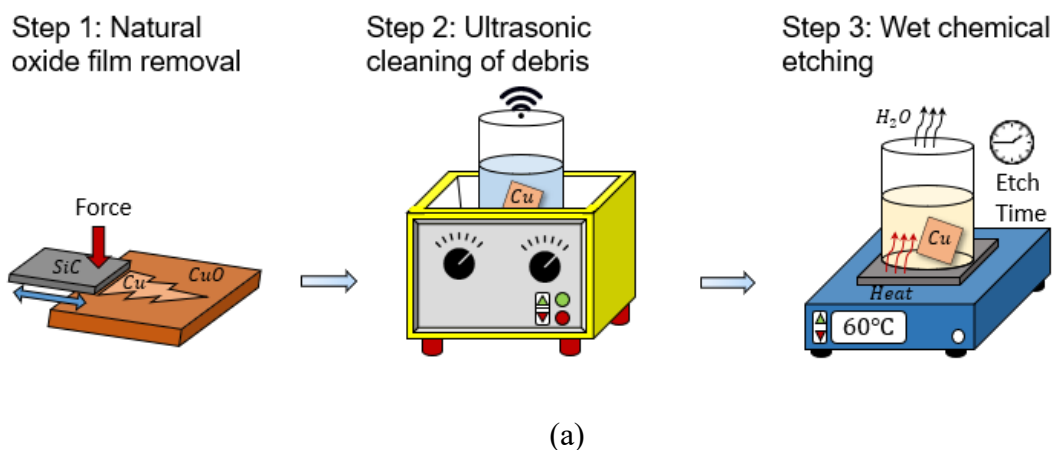
properties of the flat and microstructured samples are listed in Tables 2-1 and 2-2, respectively. The surface roughness across the centerline of the scan area is illustrated in Fig. 2.3.

**Table 2-1** Samples with flat surfaces.

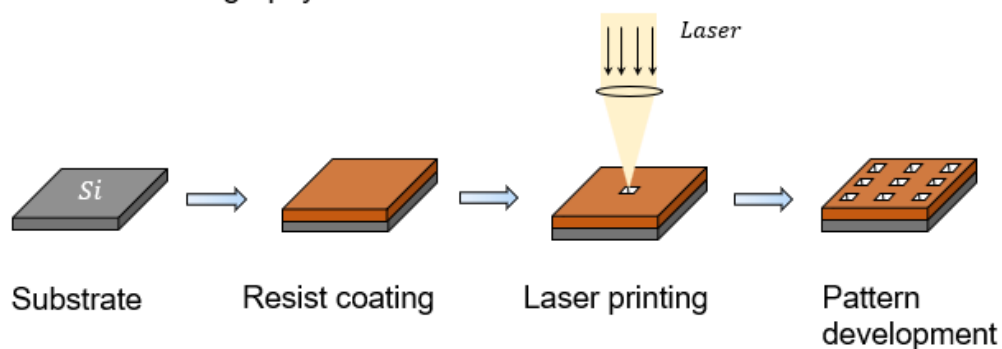
Cases	Material	$R_a$ [nm]	$\theta_0$ [°]
FS-1	Glass	$1.11 \pm 0.72$	$34.6 \pm 1.6$
FS-2	Piranha-treated Si	$1.92 \pm 0.58$	$40.2 \pm 3.4$
FS-3	Oxide-coated Si	$0.49 \pm 0.27$	$51.4 \pm 0.5$
FS-4	BHF-cleaned Si	$0.82 \pm 0.35$	$80.2 \pm 0.9$

**Table 2-2** Samples with microstructured surfaces.

Cases	Material	$R_a$ / Structure parameters [ $\mu\text{m}$ ]	$\theta_0$ [°]	
MS-1	Etched Cu	3600 s	$2.64 \pm 0.99$	$24.3 \pm 4.3$
MS-2		2700 s	$2.02 \pm 0.65$	$34.4 \pm 3.5$
MS-3		1200 s	$1.68 \pm 0.63$	$53.0 \pm 6.3$
MS-4		300 s	$1.1 \pm 0.3$	$62.1 \pm 4.1$
MS-5	Wet-etched Si	 $a = 10, b = 1, h = 8$	$93.0 \pm 3.0$	
MS-6	Deep RIE Si	 $a = 20, b = 20, h = 10$	$103 \pm 2.0$	
MS-7		$a = 60, b = 20, h = 10$	$110 \pm 2.5$	
MS-8		$a = 180, b = 20, h = 10$	$128 \pm 2.4$	



Step 1: Maskless lithography



Step 2: Deep reactive ion etching (RIE)

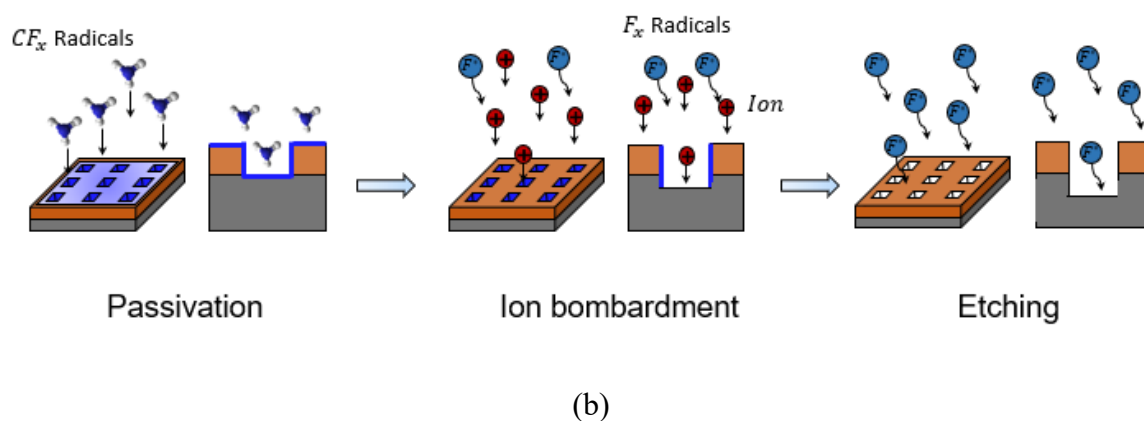
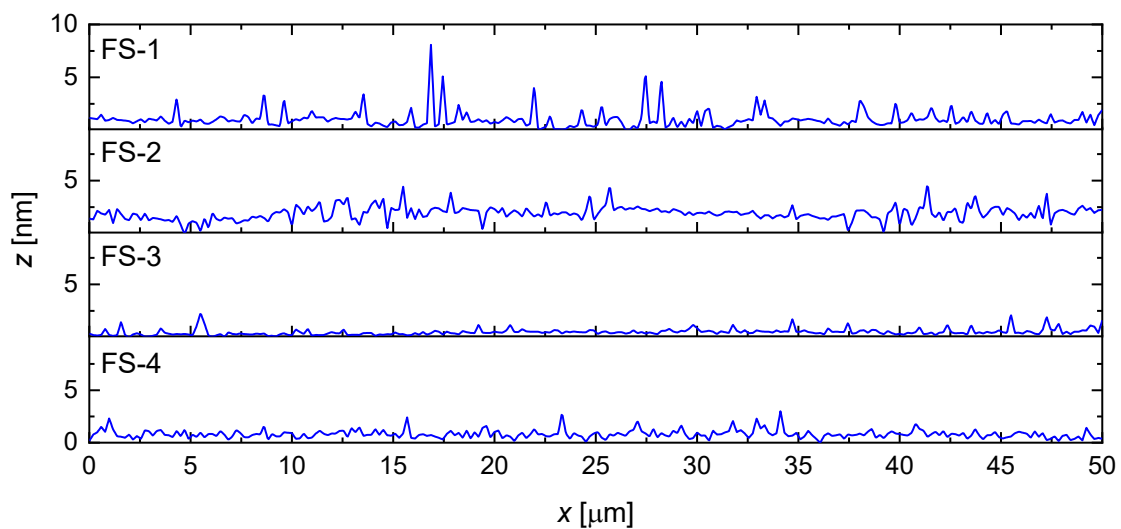
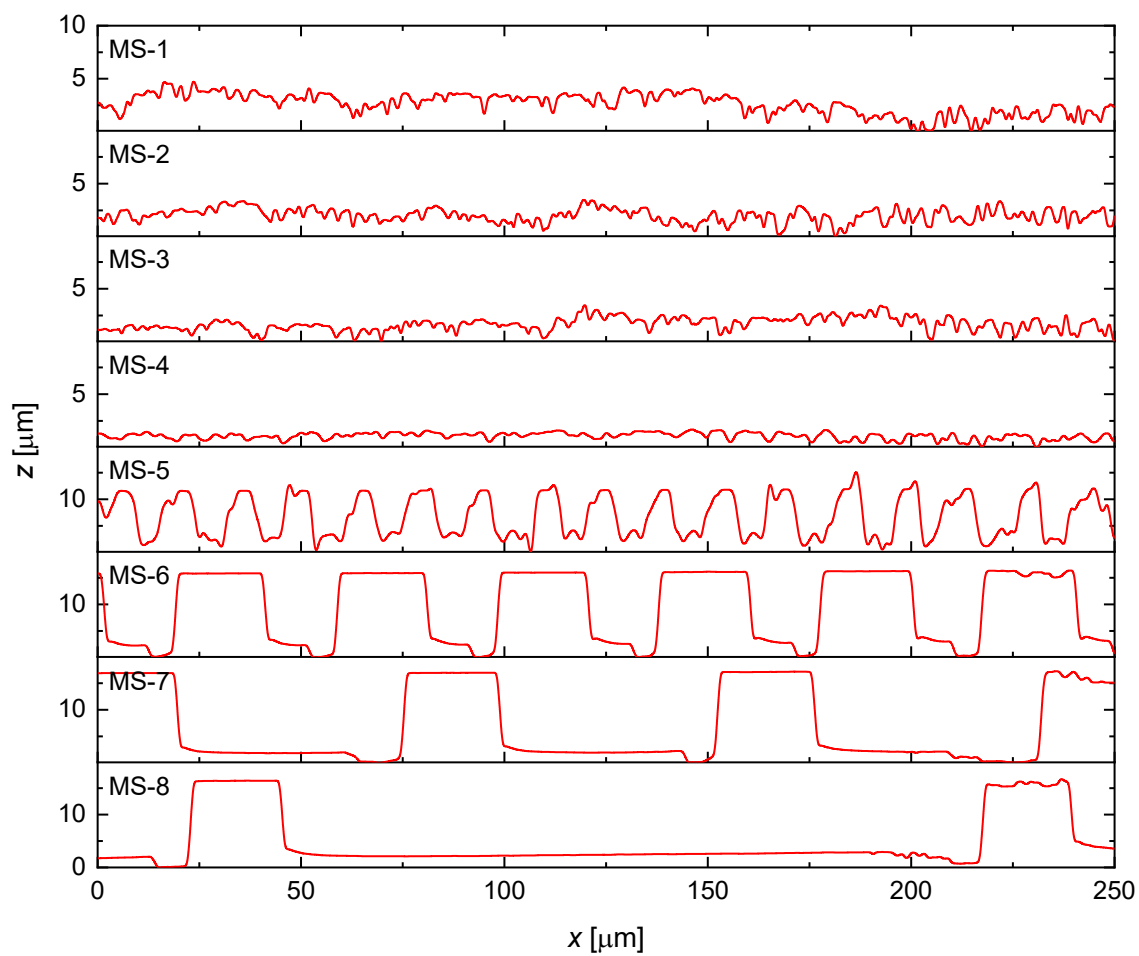


**Fig. 2.2** Schematic of the fabrication process of microstructured (a) Cu and (b) Si samples.



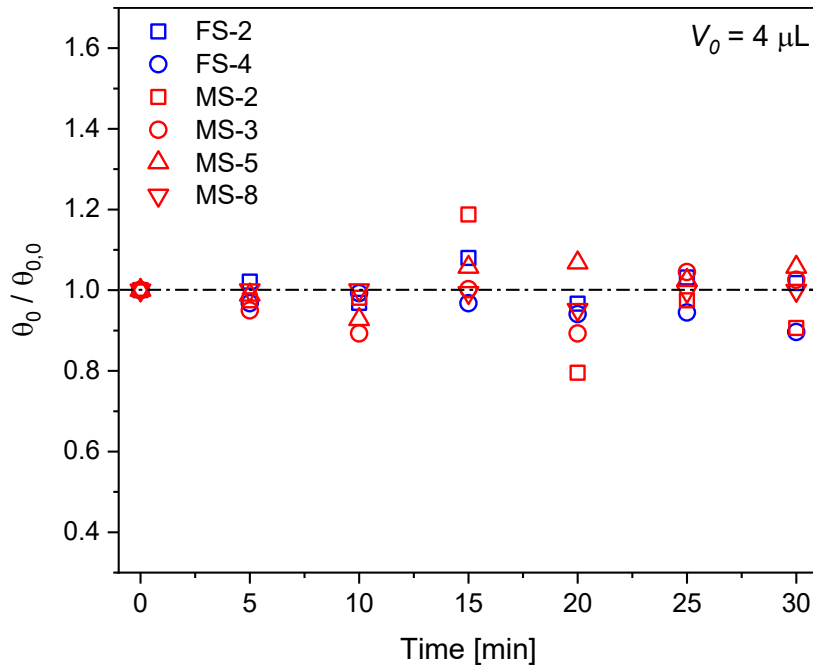
(a)



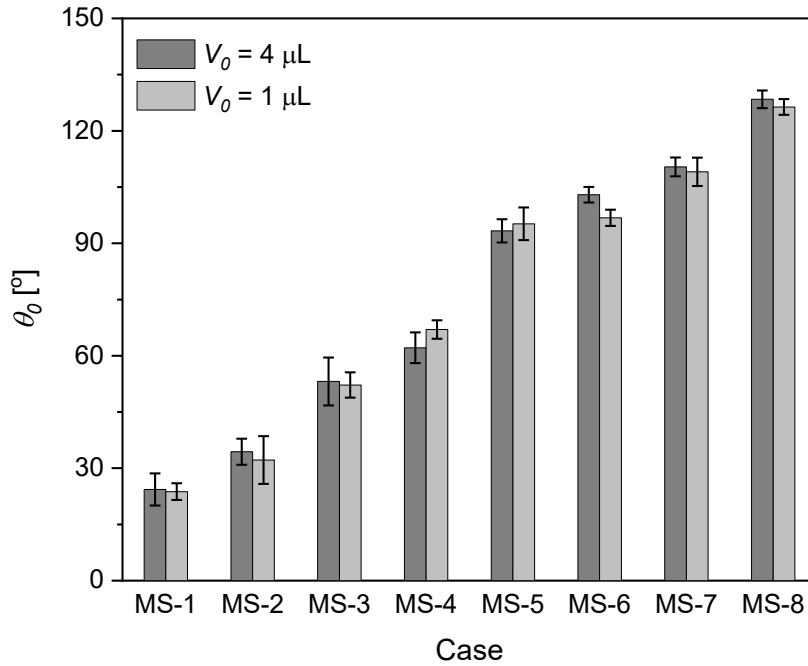
(b)

**Fig. 2.3** Surface morphologies of (a) flat and (b) microstructured samples.

The stability and uniformity of the fabricated surfaces were evaluated based on the plots of dimensionless  $\theta_0$  (i.e.,  $\theta_{0,0}/\theta_0$ ) versus time and initial volume  $V_0$  versus  $\theta_0$ , as shown in Fig. 2.4. The initial contact angle after attaining equilibrium state at the start of the stability evaluation test (0 min) is denoted as  $\theta_{0,0}$ . The results in Fig. 2.4(a) show that the dimensionless  $\theta_0$  values of the samples do not change significantly over 30 min, which is considerably shorter than the evaporation times of droplets at the surfaces considered in this study. This indicates that the fabricated surfaces are negligibly affected by the formation of the natural oxide layer; the random variation in dimensionless  $\theta_0$  over time only corresponds to the experimental non-uniformity of the surfaces. Furthermore, Fig. 2.4(b) shows that  $V_0$  does not significantly affect  $\theta_0$  of the microstructured samples.



(a)



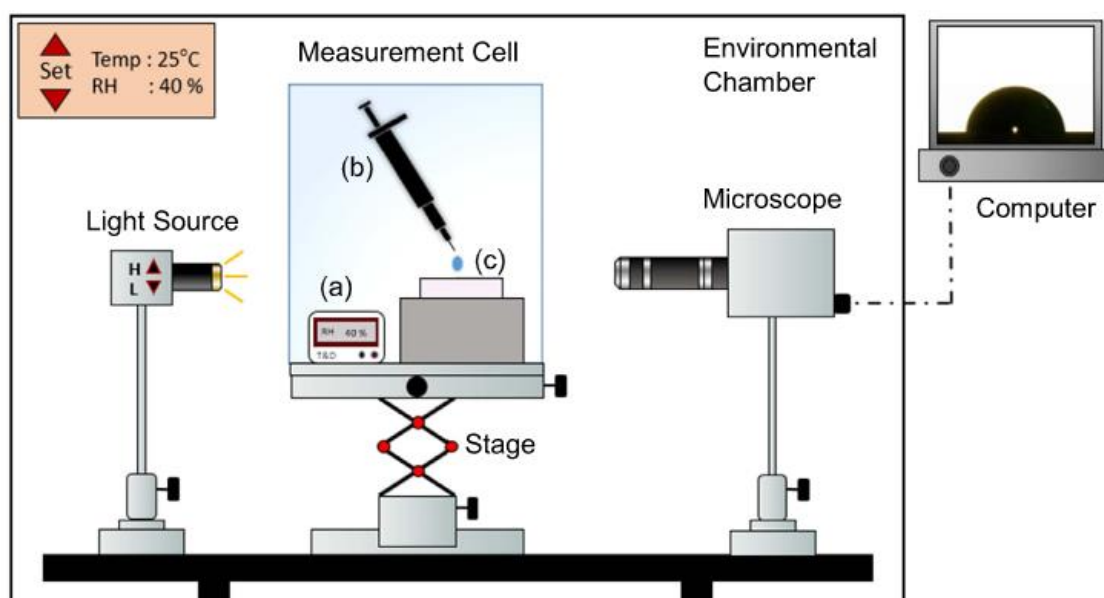
(b)

Fig. 2.4 (a) Dimensionless  $\theta_0$  vs. time and (b)  $\theta_0$  vs.  $V_0$ .

### 2.4.2 Measurement method

A digital optical microscope (Keyence, VHX200) equipped with an adjustable backlight source was used to capture a high-resolution video from the side of the droplet during evaporation. A three-axis mechanical stage was employed to adjust the droplet positions according to a fixed imaging system. An acrylic cover was used as the measurement cell to prevent convection around the droplets during evaporation. A thermal recorder (T&D Cooperation, TR-72Ui) was used to measure the ambient temperature and humidity in the vicinity of the droplet inside the measurement cell. A micropipette (Hamilton, 701RN) was used to precisely and gently disperse microliter-sized droplets onto the surface without entrapping air. An environmental chamber

(Espec, TBL-4HWOP3A) was used to precisely control the temperature and humidity of the environment. An open-source image analysis code (ImageJ, v-1.53) [87] was used to calculate  $V$ ,  $\theta$ , and  $R_d$  of the droplets using the recorded high-resolution videos. In all the experiments, high-purity water (Wako, LC /MS 214-01301) was used for the droplets to avoid the effects of solid containments. The experiments were repeated at least five times under strictly controlled ambient conditions, and the uncertainty of the results was calculated using the mean and standard deviations of the experimental dataset. A detailed schematic of the experimental setup is presented in Fig. 2.5.



**Fig. 2.5** Schematic of the measurement system. The inset shows the measurement cell comprising a (a) temperature and humidity recorder, (b) micropipette, and (c) substrate.

The temporal measurements of the ambient temperature  $T$  and relative humidity  $RH$  during the evaporation of a 4  $\mu\text{L}$  droplet are illustrated in Fig. 2.6.  $T$  and  $RH$  in the measurement cell varied within small ranges (i.e.,  $T = 25 \pm 1^\circ\text{C}$  and  $RH = 40 \pm 3\%$ ). These findings demonstrate that the ambient conditions remained unchanged during droplet evaporation at both the flat and microstructured surfaces.

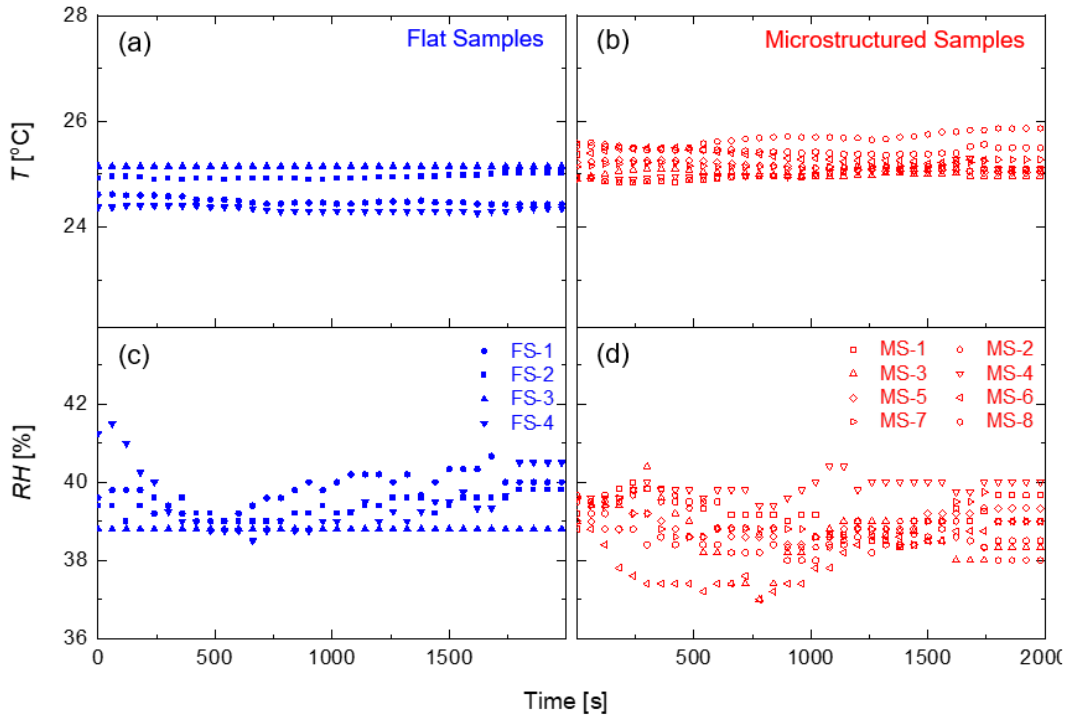


**Fig. 2.6** Temporal measurements of (a, b)  $T$  and (c, d)  $RH$  during droplet evaporation at the flat and microstructured surfaces. Symbols correspond to the arithmetic mean of the experimental data set.

## 2.5 Results and discussion

### 2.5.1 Evaporation dynamics

The temporal evolutions of  $R_d$ ,  $\theta$ , and  $V$  of the droplet during evaporation are illustrated in Fig. 5 for the flat and microstructured samples. In Fig.2.7, the symbols correspond to the arithmetic mean of the experimental data, while the error bar is from five measurements for each sample. Since part of the measurement error at the end of evaporation varies largely, few of the error bars are not presented to retain the readability of the experimental data.

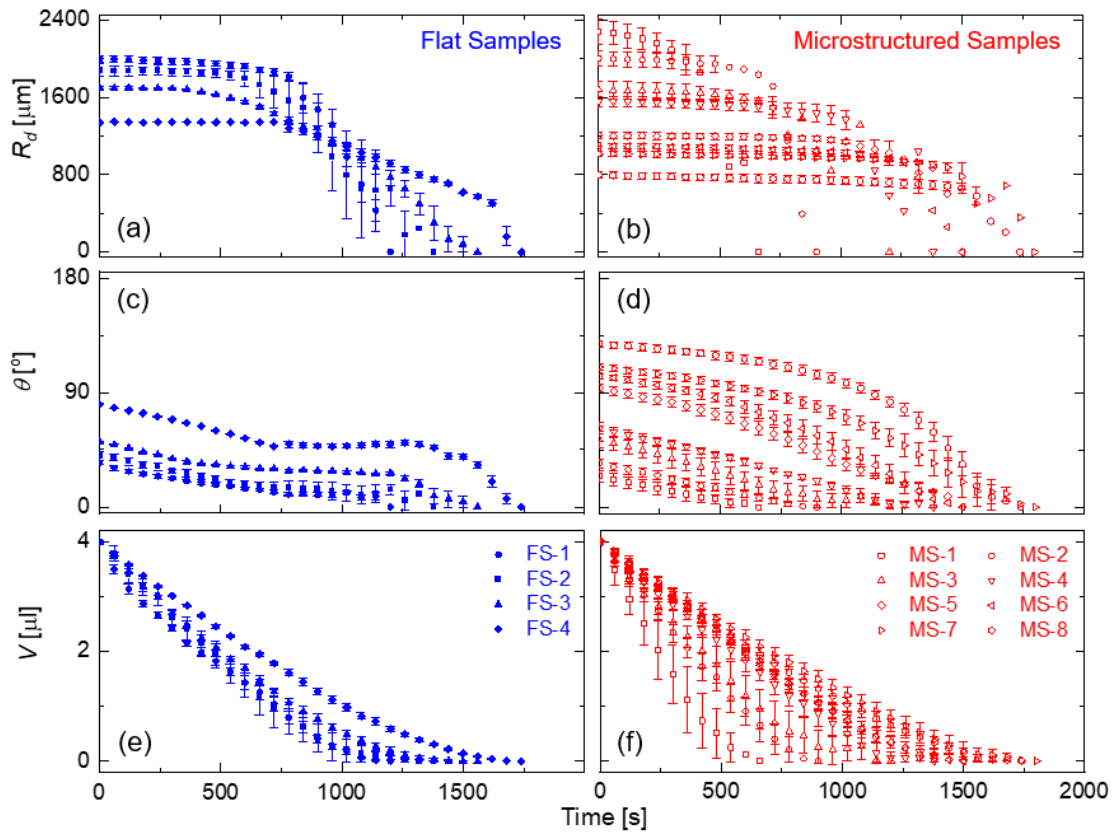


**Fig. 2.7** Temporal evolution of (a, b)  $R_d$ , (c, d)  $\theta$ , and (e, f)  $V$  during droplets evaporation at flat and microstructured surfaces.

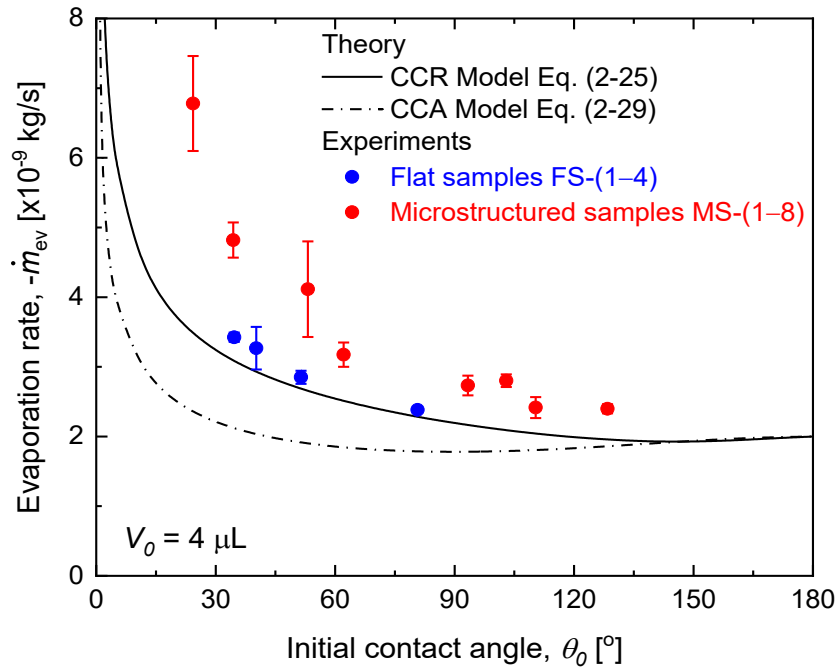
Figs. 2.7(a) and (b) demonstrate that  $R_d$  remains constant during evaporation at the microstructured surfaces. For the flat samples, as illustrated in Fig. 2.7(a),  $R_d$  generally remains constant for the maximum duration of the evaporation; however, depinning of the contact line occurs at the end of evaporation for FS-3 and FS-4. This phenomenon occurs because the pinning force is strong at microstructured and hydrophilic flat samples, and evaporation occurs mainly in the CCR mode at the expense of a decrease in  $\theta$ , as illustrated in Figs. 2.7(c) and (d). However, there exists a linear decrease in  $V$  in all the cases, as illustrated in Figs. 2.7(e) and (f), yielding a quasi-steady time course.



## 2.5.2 Comparison between theory and experiments

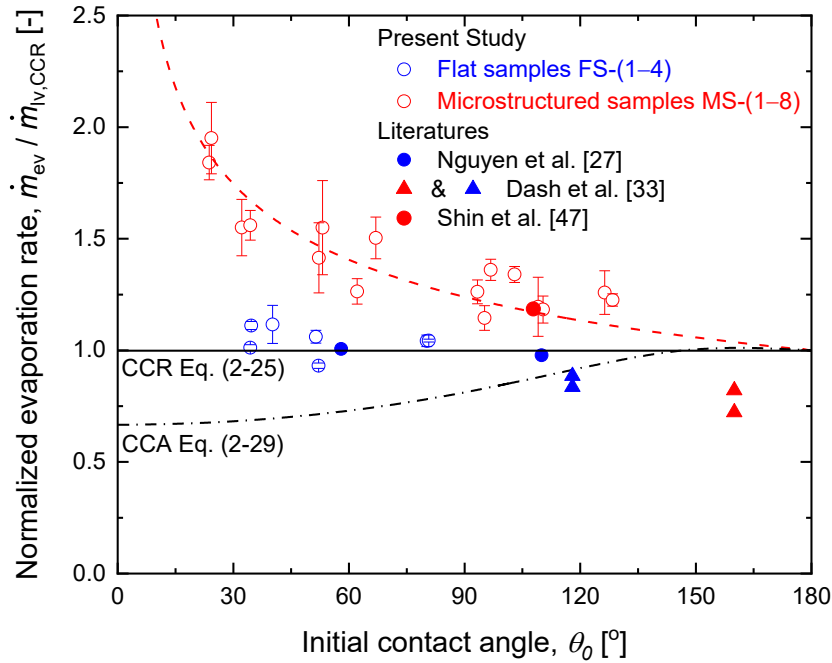
The same ambient conditions of  $T$  and  $RH$ , which are 25 °C and 40%, respectively, were used to predict the theoretical evaporation rate  $\dot{m}_{lv}$  in line with the experimental conditions measured in Fig. 2.6. The measured evaporation rate  $\dot{m}_{ev}$  was compared with the theoretical evaporation rate  $\dot{m}_{lv}$  calculated using Eqs. (2-25) and (2-29) for the CCR and CCA modes of evaporation. The theoretical prediction of the evaporation rate  $\dot{m}_{lv}$  was found to be lower for the CCA mode, as compared to the CCR mode. This is because the decrease in the surface area of the lv interface during evaporation is significant in the CCA mode. As the droplet evaporation at microstructured surfaces adopts the CCR mode, it is considered as a reference for comparison between theory and experiments.

Fig. 2.8 shows that the experimentally measured  $\dot{m}_{ev}$  increases with decreasing  $\theta_0$  for all the samples. This corresponds to a larger surface area of lv interface for the droplet with lower  $\theta_0$ , under a constant  $V_0 = 4 \mu\text{L}$ . Notably, for droplet evaporation at the flat surfaces, good agreement was noted between Eq. (2-25) and the experimental results, indicating that the role of the lv interface in mass transfer was dominant in the CCR mode of evaporation. However, for droplet evaporation at the microstructured surfaces, Eq. (2-25) yielded significantly underestimated theoretical results, corresponding to the missing term of evaporation  $\dot{m}_{slv}$  in the presence of the slv interface. This deviation become significant for the hydrophilic microstructured Cu samples MS-(1–4) than the hydrophobic microstructured Si samples MS-(5–8).



**Fig. 2.8** Comparison between theoretically calculated evaporation rates at the lv interface  $\dot{m}_{lv}$  and experimentally measured evaporation rates  $\dot{m}_{ev}$  for the flat and microstructured samples.

A detailed comparison is made with the literature to ensure the authenticity of the experiment results in the present study. For this purpose, the experimental data and theoretical predictions in Fig. 2.8 are normalized with respect to Eq. (2-25) in Fig. 2.9 for droplet evaporation at flat and microstructured surfaces for the  $\theta_0$  range from 0 to 180°. Good agreement was found between the present experimental data and literature data [16,71,88] for droplet evaporation at flat and microstructured surfaces. However, the literature data [33] for droplet evaporation at hydrophobic flat surfaces and superhydrophobic microstructured surfaces are smaller than the theoretical predictions. In these cases, the role of the slv interface to droplet evaporation both for CCR and CCA mode is negligible, while the suppression of droplet temperature reduced the evaporation rate due to the solid-liquid interfacial thermal resistance [33].



**Fig. 2.9** Comparison of the experimental results with the literature data for droplet evaporation at flat and microstructured surfaces (normalized with respect to Eq. (2-25)). Blue and red colors represent experimental evaporation rates at flat and microstructured surfaces, respectively. The red dashed line serves as a guide.

### 2.5.3 Estimation of slv interface scale and its contribution to droplet evaporation

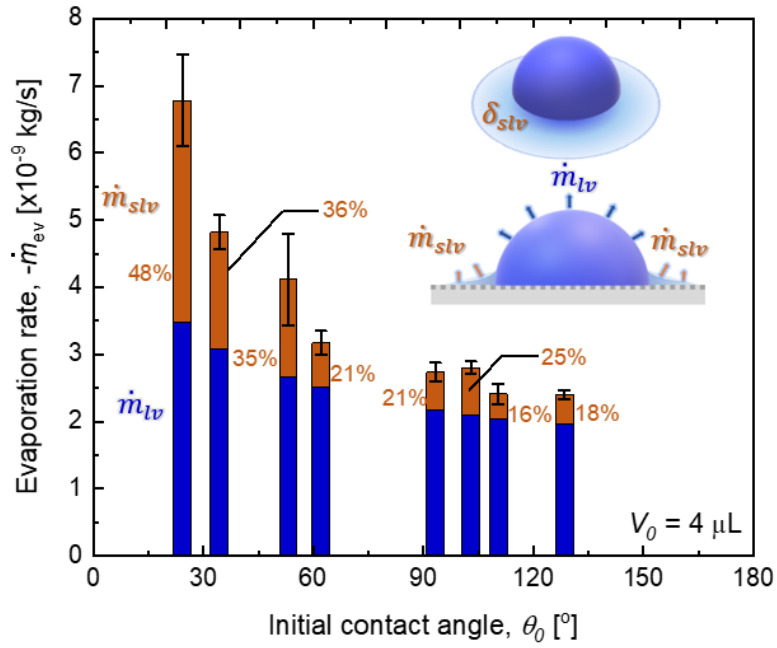
The evaporation rate  $\dot{m}_{slv}$  at the slv interface and its contribution to droplet evaporation at the microstructured surfaces are illustrated in Fig. 2.10(a). Here,  $\dot{m}_{slv}$  is estimated using Eq. (2-1) based on the difference between the experimentally measured  $\dot{m}_{ev}$  presented in Fig. 2.8 and the theoretically calculated  $\dot{m}_{lv}$  determined using Eq. (2-25). The error bar in Fig. 2.10(a) corresponds to the experimentally measured  $\dot{m}_{ev}$  and estimated  $\dot{m}_{slv}$ . The contribution of the slv interface increased from 16% to 48% as  $\theta_0$

decreased for a 4  $\mu\text{L}$  droplet; this was related to the increase in the corresponding scale of the slv interface  $\delta_{slv}$ . This is likely because the higher the capillary and disjoining pressure gradient, the larger is the scale of the slv interface, and vice versa. According to the Frumkin–Derjaguin model, a decrease in the equilibrium initial contact angle  $\theta_Y$  at the flat surface increases the disjoining pressure at the slv interface [89]. For the slv interface on micro/nanostructured surfaces, the disjoining pressure primarily depends on the wetting states inside these structures. Zhao et. al reported a higher disjoining pressure and a greater  $\delta_{slv}$  for the fully wetting (Wenzel) state, as compared to those of the non-wetting (Cassie–Baxter) state on nanostructured surfaces [90]. As shown in Table 2-2, the initial contact angles of the microstructured surfaces range from 24.3 to 128°, corresponding to the fully wetting and intermediate wetting states [19,86]. Therefore, samples MS-(1–4) yielded larger  $\delta_{slv}$  values owing to a higher disjoining pressure at the slv interface and contributed toward a higher  $\dot{m}_{slv}$ , as compared to the MS-(5–8) samples. Further clarifications regarding the evaporating slv interface in the intermediate wetting state are expected in the future.

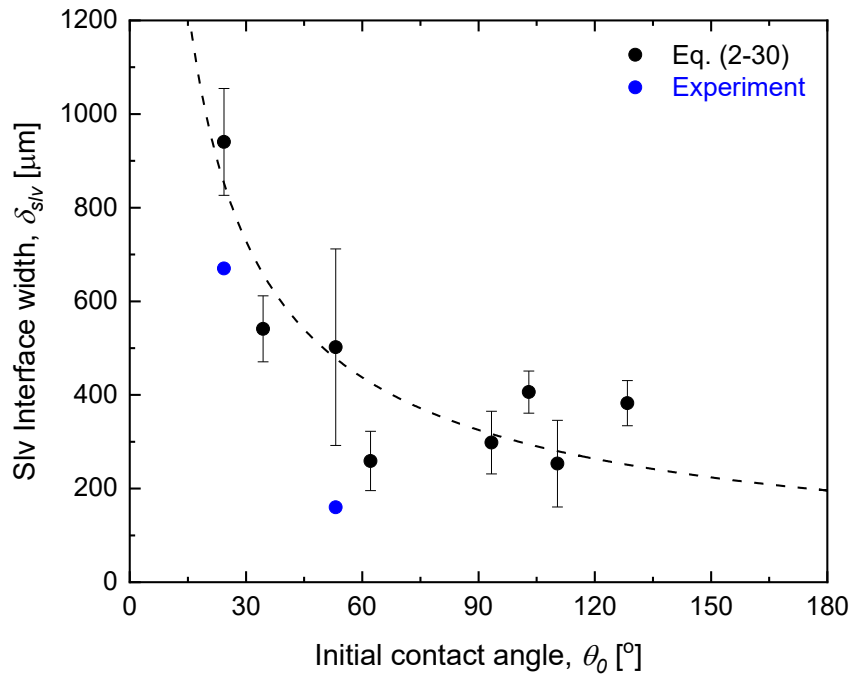
Under the thermal equilibrium attained in ambient conditions, the surface areas of the slv and lv interfaces of the droplet,  $A_{slv}$  and  $A_{lv}$ , respectively, are the principal driving mechanisms of evaporation. Therefore, the evaporation rate and the surface area ratios at the slv and lv interfaces are proportionally equal:

$$\frac{\dot{m}_{slv}}{\dot{m}_{lv}} = \frac{A_{slv}}{A_{lv}} = \frac{\pi((R_{d0} + \delta_{slv})^2 - R_{d0}^2)}{\frac{2\pi R_{d0}^2(1 - \cos\theta_0)}{\sin^2\theta_0}} = \frac{2\pi R_{d0}\delta_{slv} + \pi\delta_{slv}^2}{\frac{2\pi R_{d0}^2}{(1 + \cos\theta_0)}}. \quad (2-30)$$

Eq. (2-30) is an implicit equation for the variable  $\delta_{slv}$  and is solved iteratively using the MATLAB function Fzero having a tolerance limit of  $1 \times 10^{-9}$  [91].



(a)



(b)

**Fig. 2.10** (a) Estimated contributions of the slv interface to evaporation rate of droplets on microstructured surfaces. (b) Slv interface scale  $\delta_{slv}$  versus initial contact angle  $\theta_0$  for 4  $\mu\text{L}$  droplets. The fitted dashed line serves as a guide.

The scale  $\delta_{slv}$  of the slv interface estimated using Eq. (2-30) is plotted against  $\theta_0$  in Fig. 2.10(b) for the droplets evaporating at the microstructured surfaces MS-(1–8). The error bar and scattering of the estimated values correspond to  $\dot{m}_{slv}$  in Eq. (2-30).  $\delta_{slv}$  decreased with increasing  $\theta_0$ , corresponding to the trend of  $\dot{m}_{slv}$ , as illustrated in Fig. 2.10(a). This finding confirms that the scale of the slv interface depends on the surface wettability of the microstructured samples. According to the results shown in Fig. 2.7(b), the estimated  $\delta_{slv}$  is on the order of  $R_{d0}$ , thereby highlighting the fact that the scale effect of the slv interface is prominent for a 4  $\mu\text{L}$  droplet on microstructured surfaces. The experimental  $\delta_{slv}$  shown in Fig. 2.10(b) was measured from the top view images of the 4  $\mu\text{L}$  droplet on the microstructured Cu samples MS-1 and MS-3 captured using the high-speed microscope (Keyence, VW6000). The acquired images were analyzed using an open-source image analysis code (ImageJ, v-1.53). The experimental  $\delta_{slv}$  values agreed well with the values estimated using Eq. (2-30) as shown in Fig. 2.10(b).

Experiments were performed to measure the scale  $\delta_{slv}$  from the top view of the 4  $\mu\text{L}$  droplet on the microstructured Cu samples MS-1 and MS-3 using a high-speed microscope (Keyence, VW6000). Optical magnifications of 30x and 50x were used for the droplet on samples MS-1 and MS-3, respectively. The acquired images were analyzed using an open-source image analysis code (ImageJ, v-1.53). The results with the scale are presented in Fig. 2.11 (b). Note that  $\delta_{slv}$  was measured at three different

locations as displayed in Fig. E1(b). The mean values are approximated and plotted in Fig. 8(b).

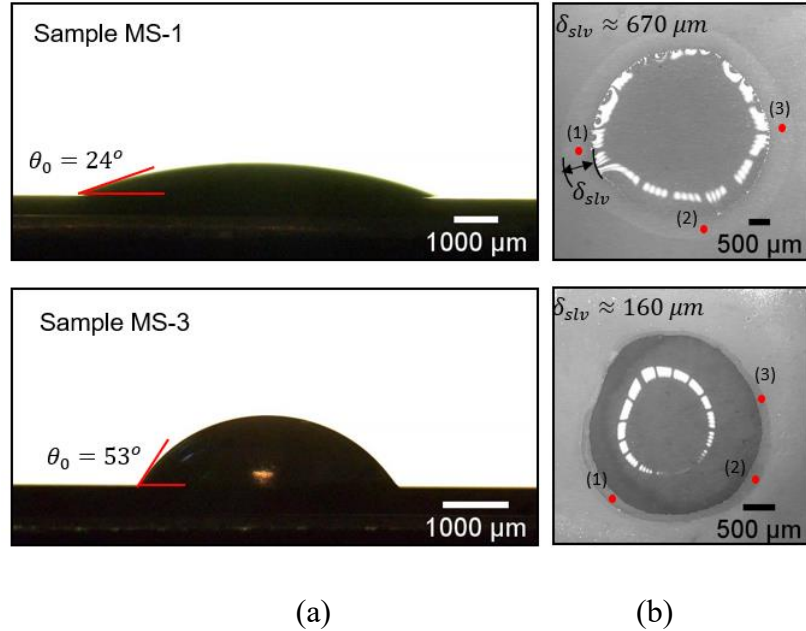
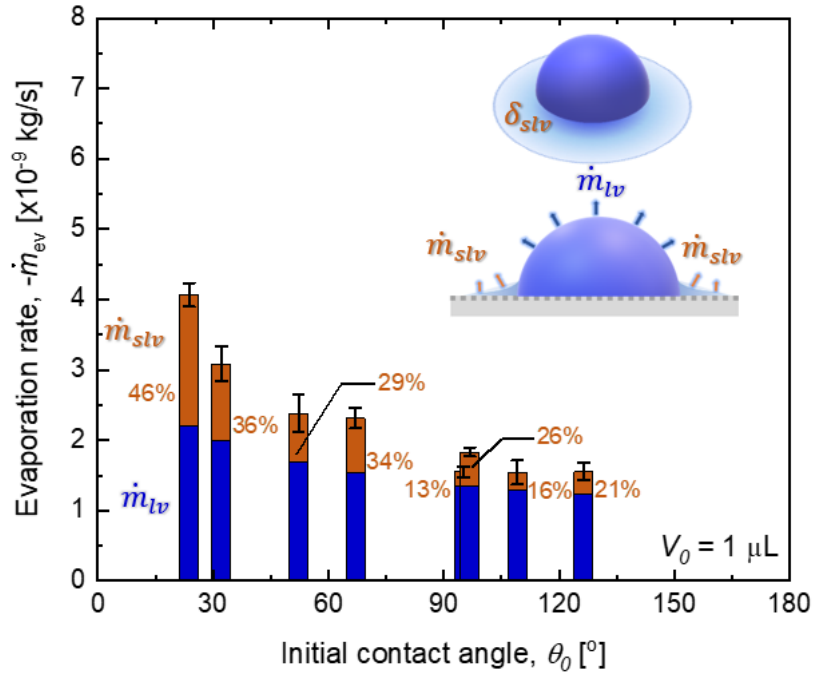


**Fig. 2.11** Microscopy images of (a) side view and (b) top view of the droplet at time  $t=0$  s for the microstructured Cu samples MS-(1,3).

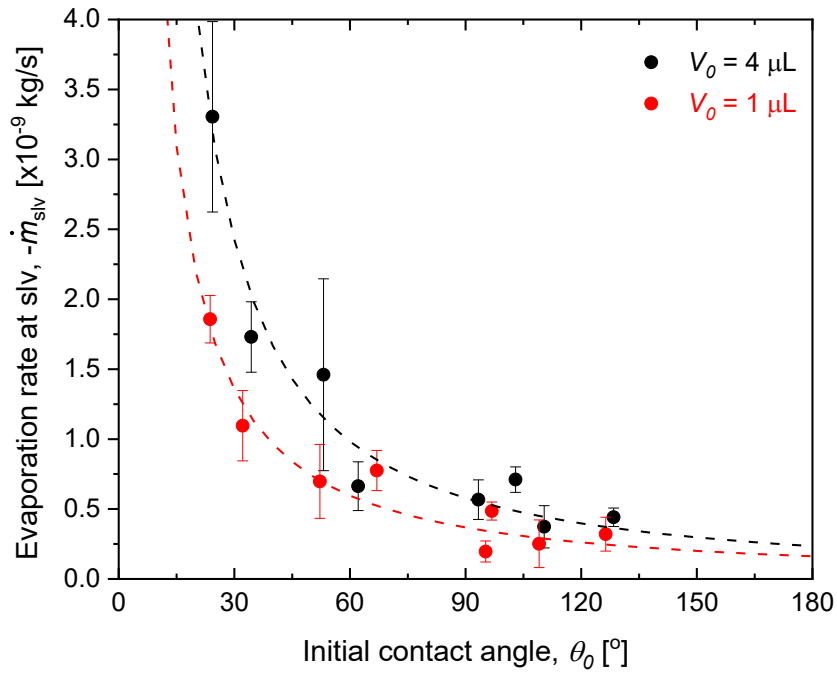
#### 2.5.4 Effect of droplet volume on the scale and evaporation rate at the slv interface

The effects of  $V_0$  on  $\dot{m}_{ev}$ ,  $\dot{m}_{slv}$ , and  $\delta_{slv}$  for droplet evaporation at the microstructured surfaces are shown in Fig. 2.11. Fig. 2.12(a) shows that the contribution of the slv interface to the droplet evaporation of 1  $\mu\text{L}$  is approximately of the same order of magnitude as that for a 4  $\mu\text{L}$  droplet (see Fig. 2.10(a)). This indicates that the contribution of the slv interface to droplet evaporation is not affected by the droplet volume in the microliter range. As can be seen in Figs. 2.10(a) and 2.12(a), both  $\dot{m}_{lv}$

and  $\dot{m}_{slv}$  decreased with  $V_0$ ; therefore, the percentage contribution of the slv interface remained constant. In

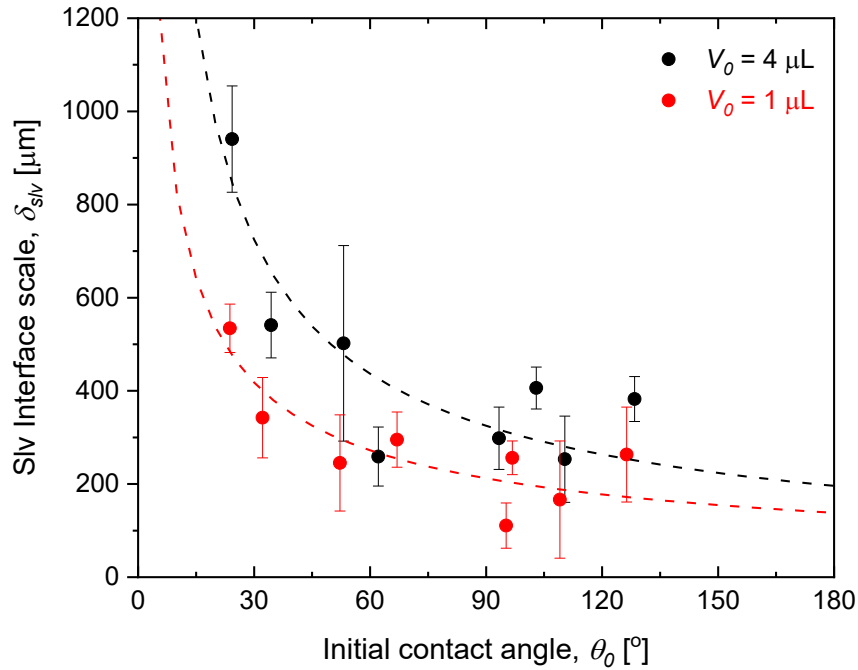


(a)



(b)





(c)

**Fig. 2.12** Effects of  $V_0$  on (a)  $\dot{m}_{ev}$ , (b)  $\dot{m}_{slv}$ , and (c)  $\delta_{slv}$  for droplet evaporation at microstructured surfaces. The fitted dashed lines serve as guides.

Fig. 2.10(b),  $\dot{m}_{slv}$  of a 1  $\mu\text{L}$  droplet is smaller than that of a 4  $\mu\text{L}$  droplet. On a related note,  $\delta_{slv}$  of a 1  $\mu\text{L}$  droplet is smaller than that of a 4  $\mu\text{L}$  droplet, as illustrated in Fig. 2.10(c). This implies that, for a given surface, an evaporating droplet with a larger  $V_0$  spreads more easily, owing to a larger  $\delta_{slv}$ . Notably,  $\delta_{slv}$  and  $\dot{m}_{slv}$  at the slv interface decreased with increasing  $\theta_0$ , exhibiting similar trends with  $\theta_0$  for 1  $\mu\text{L}$  and 4  $\mu\text{L}$  droplets. The effect of the droplet volume on  $\delta_{slv}$  and  $\dot{m}_{slv}$  can be further investigated by decreasing  $V_0$  below 1  $\mu\text{L}$ , which will be addressed in the future.

## 2.6 Summary

This study provides detailed insights into the contributions of the slv interface toward droplet evaporation at micro/nanostructured surface and highlights the effects of surface wettability and droplet volume. we found that contribution of the slv interface was more significant than that of the lv interface for droplet evaporation at micro/nanostructured surfaces, while the lv interface dominated the droplet evaporation at flat surfaces. The scale of the slv interface  $\delta_{slv}$  increased at the microstructured surfaces, ranging from 253–940  $\mu\text{m}$  for 4  $\mu\text{L}$  droplets with contact radii of 796–2280  $\mu\text{m}$ . The contribution of the slv interface to the droplet evaporation rate varied between 21% and 48% for hydrophilic microstructured Cu surfaces. However, for droplets on hydrophobic microstructured Si surfaces, the contribution of the slv interface to the evaporation rate was lower and ranged from 16% to 25%. The scale  $\delta_{slv}$  and evaporation rate  $\dot{m}_{slv}$  at the slv interface increased with a decrease in the initial contact angle  $\theta_0$  or an increase in the droplet volume  $V_0$ . However, accurate measurements regarding the scale of the slv interface  $\delta_{slv}$  and direct measurement of the evaporation rate at the slv interface  $\dot{m}_{slv}$  remain a challenge. Clarifications on the evaporation at the slv interface in the intermediate wetting state are expected in the future. Overcoming these limitations will pave the way for practical engineering and medical applications of droplet evaporation at micro/nanostructured surfaces.

## **Chapter 3**

# **3 Contribution of adjacent droplets to droplet evaporation**

## **3.1 Introduction**

Droplet evaporation at a solid surface in an array has scientific relevance in applications such as inkjet printing, spray cooling, perspiration on human skin, coughing/sneezing, and DNA mapping. The presence of adjacent droplets around an evaporating droplet in array at a solid surface increases vapor accumulation in the vicinity of liquid-vapor interface. This vapor accumulation referred to as shielding effect will suppress the evaporation rate of a droplet in array as compared to an isolated droplet under the same conditions. However, little is known about the effects of the array configuration of the adjacent droplets on the evaporation rate of droplets in an array. Further, As an isolated droplet evaporate in three modes; the constant contact radius (CCR), the constant contact angle (CCA) and mix modes depending on the surface and liquid properties. However, the presence of the adjacent droplet will alter the time that a droplet spends in each mode during droplet evaporation in array and will be influenced by the physical parameters of the adjacent droplets. In this context, we demonstrate with numerical simulations and experiments that physical parameters such as the number, size, and separation distance of adjacent droplets highly influence evaporation rate of droplets in an array.

Current diffusion-based theoretical models can accurately predict the evaporation rate of an isolated droplet on a flat surface [66,69,70,92]. However, in identical conditions, these models overestimate the evaporation rate of a droplet surrounded by neighboring droplets in the array [93]. In this context, Carrier *et al.* introduced the concept of "super-droplet" and proposed an analytical expression that describes how its evaporation is hindered by the presence of adjacent droplets [76]. A basic assumption of this model is that an array of droplets with an arbitrary contact angle can be considered as a single flat super-droplet. However, this assumption prevents the model from accurately predicting the evaporation rate when the distance between individual droplets in the array is larger than a threshold value [79]. To address this limitation, Wray *et al.* [94] proposed a theoretical model by assuming that droplets in the array interact only in the gas domain through diffusion. Wray *et al.*'s model is capable of accounting for the relative size and position of each droplet in the array to accurately predict the evaporation rate of droplets [94]. Their predictions were experimentally validated by Edwards *et al.* [78], who used an interferometric technique to directly measure the individual evaporation rate of droplets on hydrophilic glass surfaces for ten different array configurations.

However, Wray *et al.*'s model is applicable only to hydrophilic droplets (so-called thin droplets) in the array. Therefore, the model is inappropriate to predict the evaporation rates of droplets in the array on hydrophobic surfaces [94, 95,96]. In this study, we propose a generalized model that considers the important factor of surface wettability for accurately predicting the evaporation rate of droplets in array.

## 3.2 Effect of array configuration on droplet evaporation

### 3.2.1 Problem definition

An array of droplets is considered to evaporate on flat surfaces as shown in Fig. 3.1. In the given array configuration, the central droplet in array is considered as a reference droplet  $o$ , as it is uniformly surrounded by  $n_d$  adjacent droplets that ranges between 1 to 4. The contact radius of the reference and adjacent droplets are denoted as  $R_{d0}$  and  $R_{dn}$ , respectively. While the contact angle  $\theta$  of all the droplets are identical and is equal to  $50^\circ$ . The contact radius of the adjacent droplets is varied between 0 to  $2R_{d0}$ . The adjacent droplets are separated by the constant distance  $d_s$  which ranges from 0 to  $80R_{d0}$ .

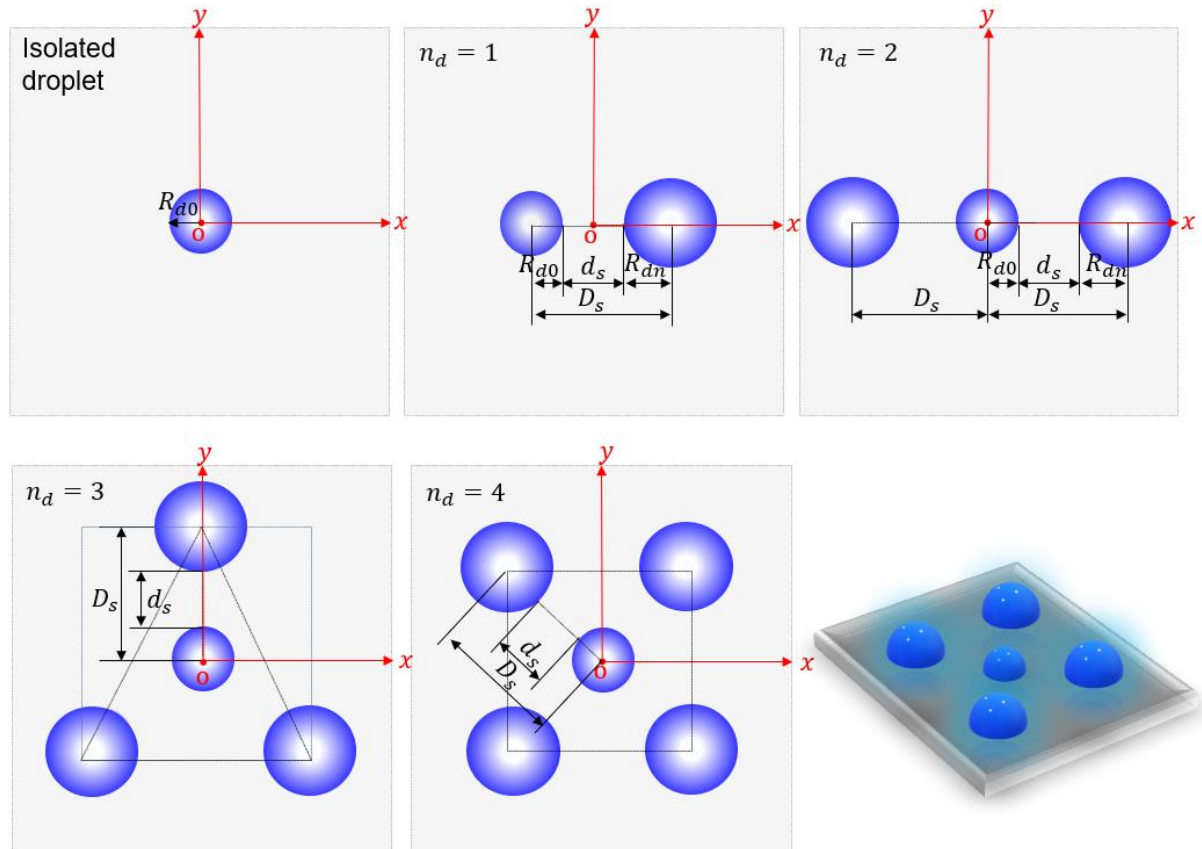


**Fig. 3.1** Schematics of droplet array configurations in the present study.

The ambient conditions (i.e., temperature and relative humidity) are kept constant at 25°C and 40%. The continuous diffusion of vapour from the liquid-vapour interface (lv) of the droplets in the array with saturation density  $\rho_s$  to the ambient density  $\rho_\infty$  determine the evaporation process. The evaporation is considered to be quasi steady because the ratio of diffusion time to the evaporation time ( $t^* = \frac{\rho_s - \rho_\infty}{\rho_s}$ ) is far less than one. The evaporation cooling at lv interface caused by latent heat transfer has negligible influence on the evaporation rate. The external and internal flows in the liquid and gas domains, respectively, are considered weak to influence the evaporation rate. The droplets are sufficiently small to be affected by gravity since  $R_d$  is smaller than capillary length.

### 3.2.2 Simulation system

A cylinder with a radius and height of  $100 R_{d0}$ , where  $R_{d0} = 1$  mm, was used as the simulation domain as depicted in Fig. 3.2(a), and it enclosed a droplet array on a surface located at the bottom of the system. A non-structured tetrahedral grid was used for the spatial discretization of the simulation domain, and the total number of grid elements ranged between 1 and 3 million. Fig. 3.2(b) shows the grid in the  $xy$ -plane of the simulation domain, and its enlarged view in vicinity of the droplet array is shown in Fig. 3.2(c). The element size of the simulation grid was refined in the vicinity of the lv interface of the droplets to improve the simulation accuracy. Simulation grids were generated using the preprocessor SALOME[97], and the maximum aspect ratio and skewness of the tetrahedral elements in simulations grids were below 5 and 0.85,

respectively. Thus, it was ensured that the grid quality was not compromised by the presence of the sharp curvature at the lv interface of the droplets in the simulation domain. The vapor diffusion from the lv interface to the gas domain is simulated only and the internal flow of the droplet is ignored because the liquid is not included in the simulation domain.

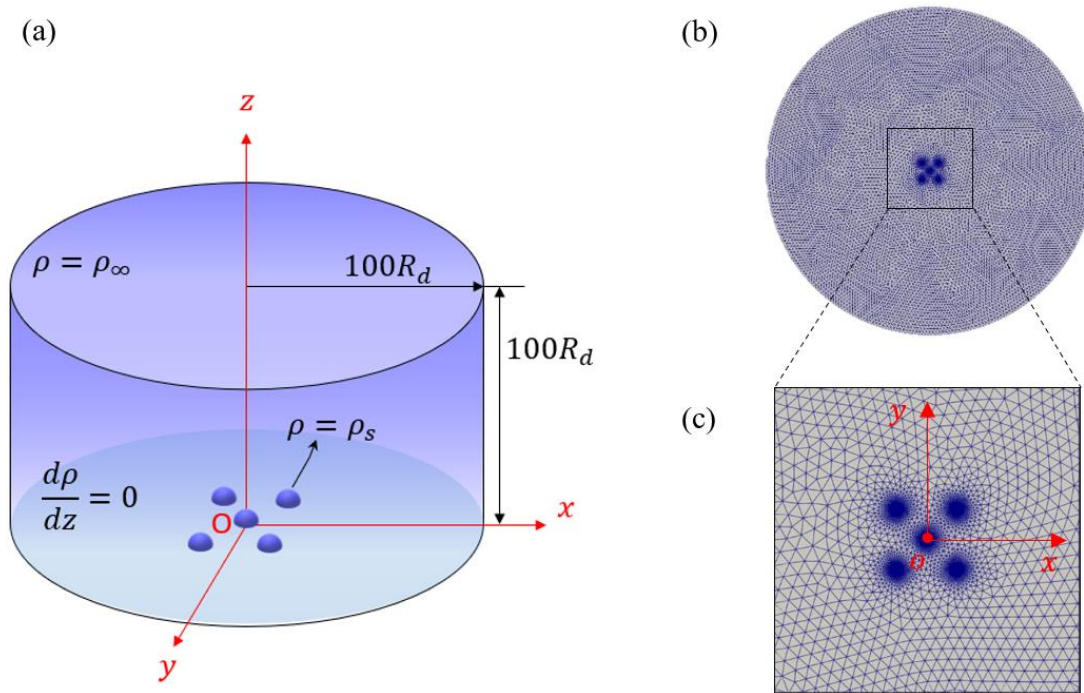


**Fig. 3.2** Simulation system: (a) domain with boundary conditions, (b) grid in the  $xy$ -plane of the simulation domain, and (c) enlarged view of the grid in vicinity of the droplet array.

Fick's second law can be written as a three-dimensional Laplace equation in terms of the vapor density  $\rho$  [82]:

$$\frac{d^2\rho}{dx^2} + \frac{d^2\rho}{dy^2} + \frac{d^2\rho}{dz^2} = 0. \quad (3-1)$$

The mass transfer rate based on Fick's first law can be written as

$$\dot{m} = -A_{lv}D(T)\left.\frac{d\rho}{dn}\right|_{lv}. \quad (3-2)$$

Here,  $\frac{d\rho}{dn}$  [kg/m<sup>4</sup>] is the vapor density gradient normal to the lv interface, and  $\hat{n}$  is a unit vector normal to the lv interface.

The boundary conditions were as follows: (1) at the lv interface of all droplets, the vapor density was constant ( $\rho = \rho_s = 23$  g/m<sup>3</sup>); (2) in the far field, the vapor density was constant ( $\rho = \rho_\infty = 9$  g/m<sup>3</sup>); and (3) at the walls, there was no vapor penetration into the wall as  $\frac{d\rho}{dz} = 0$ . The contact angle of all the droplets was identical and in the range from 10° to 170°, and the number of adjacent droplets  $n_d$  varied between 0 and 4. The separation distance  $d_s$  was maintained constant at  $10R_d$ . Grid independence was confirmed for all simulations. The governing equations, Eqs. (3-1) and (3-2), were solved using the finite volume method in OpenFOAM [98]. The Gauss linear scheme was adopted as the Laplacian scheme for discretization, and surface normal gradients were corrected. The simulation results were visualized using the post-processor Paraview [99].

### 3.2.3 Experimental materials and methods

An untreated cover glass of 24 mm × 24 mm (Matsunami Glass) with a Young contact angle  $\theta_Y$  of  $50^\circ \pm 2^\circ$  was used as a hydrophilic surface. Hydrophobic surfaces with  $\theta_Y = 120^\circ \pm 3^\circ$  were prepared by spraying a commercial water-repellent coating evenly onto the cover glass and drying the sprayed glass in a draft chamber for 60 min. A scanning probe microscope (SPM, Shimadzu, SPM-9700HT) was used to observe the surface morphologies of the hydrophilic and hydrophobic surfaces, and SPM images are



shown in Fig. 3.3. The average surface roughness  $Ra$  [nm] was found to be  $0.75 \pm 0.43$  nm for hydrophilic surfaces and  $231 \pm 87$  nm for hydrophobic surfaces. Since  $Ra$  of both hydrophilic and hydrophobic surfaces is on the nanometer scale, these surfaces are considered to be flat surfaces.

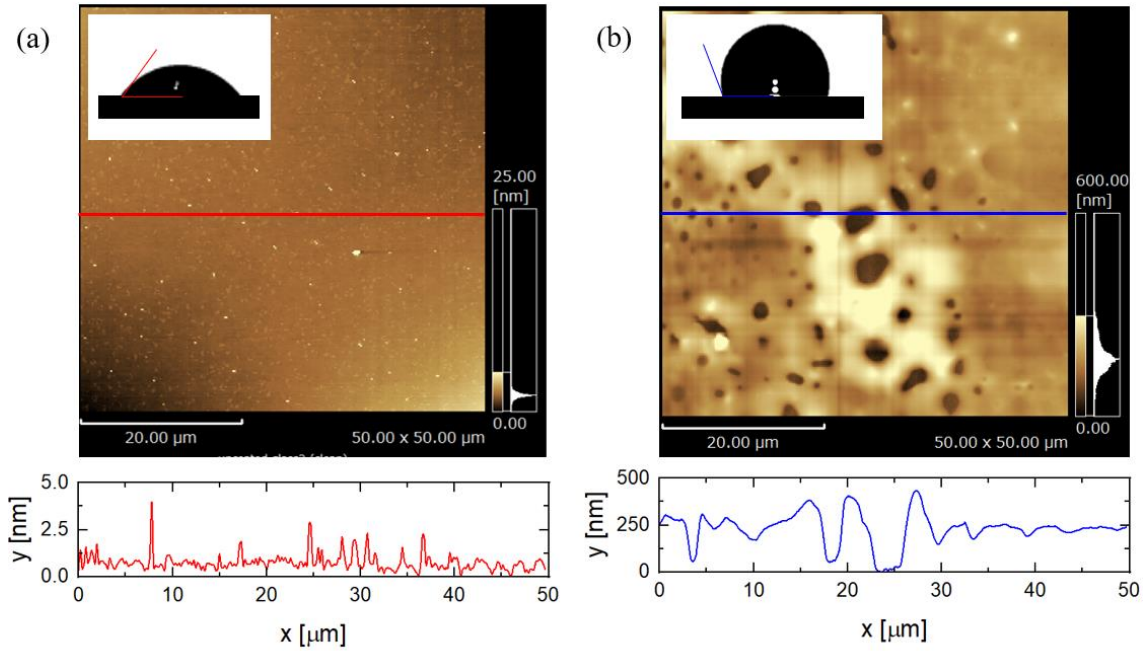


**Fig. 3.3** SPM images and cross-sectional profiles of (a) hydrophilic and (b) hydrophobic surfaces. The insets show the water contact angle images at the surfaces.

A detailed schematic of the experimental setup is presented in Fig. 3.4. Deposition positions for the droplet array were manually marked on the rear side of the transparent cover glass, and 1  $\mu$ L pure water droplets were carefully deposited on the marks with a micropipette (Hamilton, 701 RN), with the aid of a vertically aligned microscope (Sightron, nano capture SP725S). The number of adjacent droplets  $n_d$  was set to four, and the separation distance was  $10R_d$ . The droplets in the array were allowed to evaporate naturally in a measurement cell under controlled ambient conditions in an environmental chamber (Espec, TBL-4HWOP3A). The measurement cell was made of

*Graduate School of Engineering, Kyushu Institute of Technology, Japan*

transparent acrylic to prevent convection around the droplets during evaporation. The dynamics of the reference droplet was recorded using a horizontally oriented digital microscope (Keyence, VHX-200) with a backlight source. The contact angle, contact radius, and volume of the reference droplet were then calculated from recorded videos using an open-source image analysis code (ImageJ, v-1.53) [87]. A thermo recorder (T&D Corporation, TR-72Ui) was used to measure the temperature and relative humidity in the measurement cell during droplet evaporation. Experiments were repeated five times for each measurement of isolated droplets and the reference droplet in arrays on hydrophilic and hydrophobic surfaces. The uncertainty of the results was calculated using the mean and standard deviation of the experimental dataset.

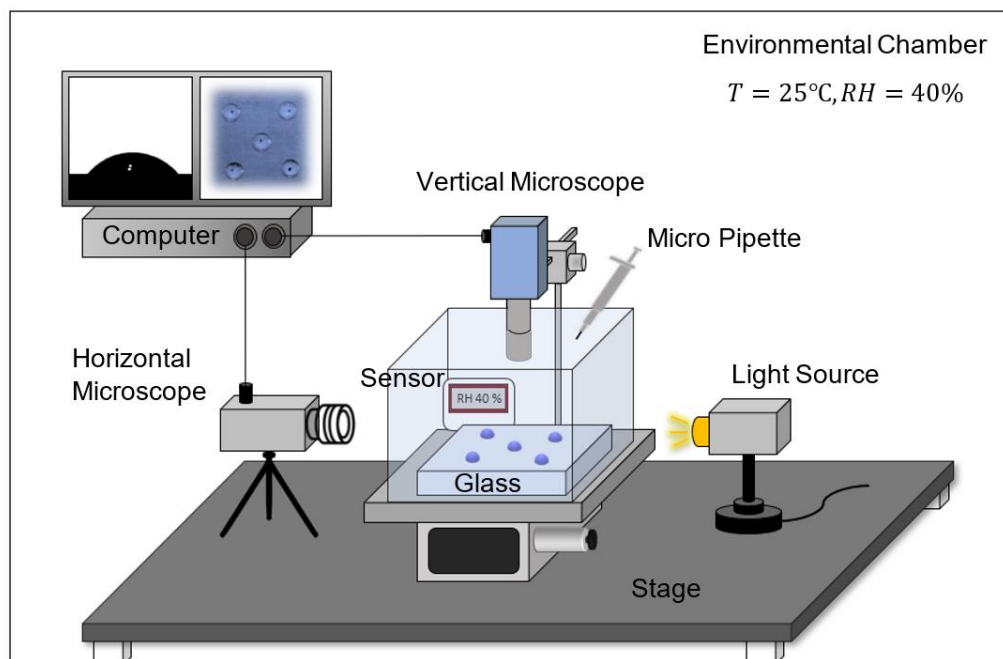


**Fig. 3.4** Schematic of the measurement system for evaporation of droplet array under constant temperature and humidity.

### 3.2.4 Results and discussion

The steady state density profiles are calculated with the numerical simulation for the given conditions and results has been plotted in Fig. 3.5 and 3.6. In Fig. 3.5, the effect of the separation distance  $d_s$  and number of adjacent droplets  $n_d$  has been studied for the constant contact angle and size of adjacent droplet  $R_{dn}$ .

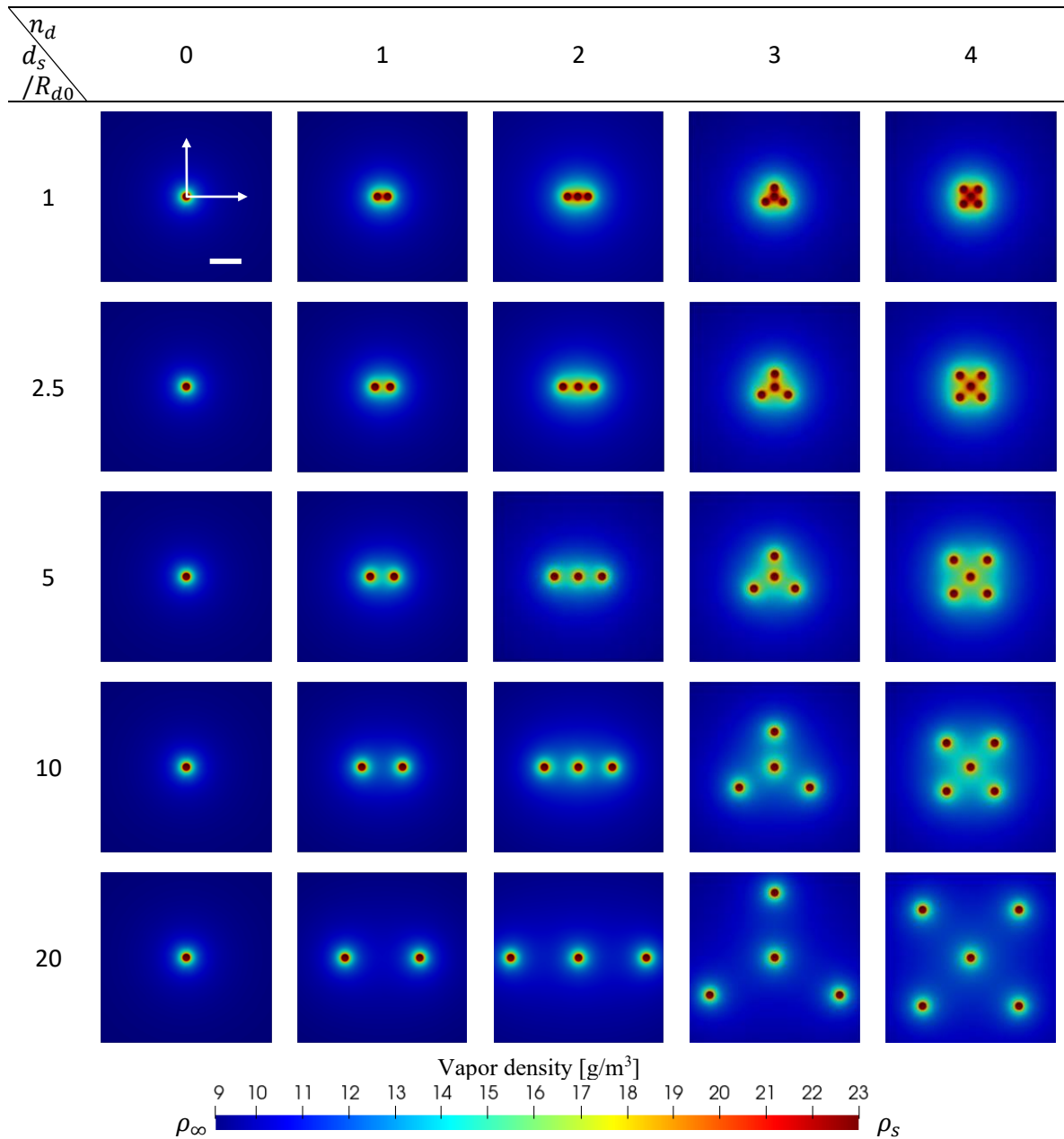


**Fig. 3.5** Effect of separation distance  $d_s$  and number of adjacent droplets  $n_d$  on vapor density distribution in the  $xy$ -plane at the bottom of the simulation domain for constant contact angle  $\theta = 50^\circ$  and size of adjacent droplet  $R_{dn} = R_{dn0}$ , where  $R_{d0} = 1\text{mm}$ .

The vapor density near the reference droplet increases monotonously when the number of the adjacent droplets increases from 1 to 4, in comparison with the isolated droplet. This implies that the vapor density near the reference droplet in the diffusion domain depended on the number of adjacent droplets. However, as the adjacent droplets become close to the reference droplet, the vapor density increases sharply. From Fig.3.5, it is found that when the  $d_s$  reduces to order of  $R_{d0}$  the high vapor density region increases at the centre of the droplet array in comparison to the isolated droplet in particular for  $n_d = 4$ . However, for the  $d_s = 20R_{d0}$ , the extended high vapor density region disappears. In Fig. 3.6, the effect of the adjacent droplet size  $R_{dn}$  and number of adjacent droplets  $n_d$  has been studied for the constant contact angle and separation distance  $d_s$ . Figure 3.6 shows that when a reference droplet is surrounded equally by a small adjacent droplet i.e.,  $R_{dn} < R_{d0}$ , the vapor density around the reference droplet is not much affected in comparison to the isolated droplet when  $R_{dn} = 0.1R_{d0}$ . This result shows that the vapor mediated interaction between a large reference droplet surrounded by small size adjacent droplets is relatively insignificantly to be weak. Contrary, when a small reference droplet is surrounded by large sized adjacent droplets as can be seen for the  $R_{dn} = 2R_{d0}$ , the high vapor density region in the centre of the droplet array increases tremendously in comparison to the isolated droplet for the for  $n_d = 4$ . Figure 3.5 and 3.6 therefore depict that the vapor mediated interactions between the

evaporating droplet does not remain same for same reference droplet at different configurations of the adjacent droplets.

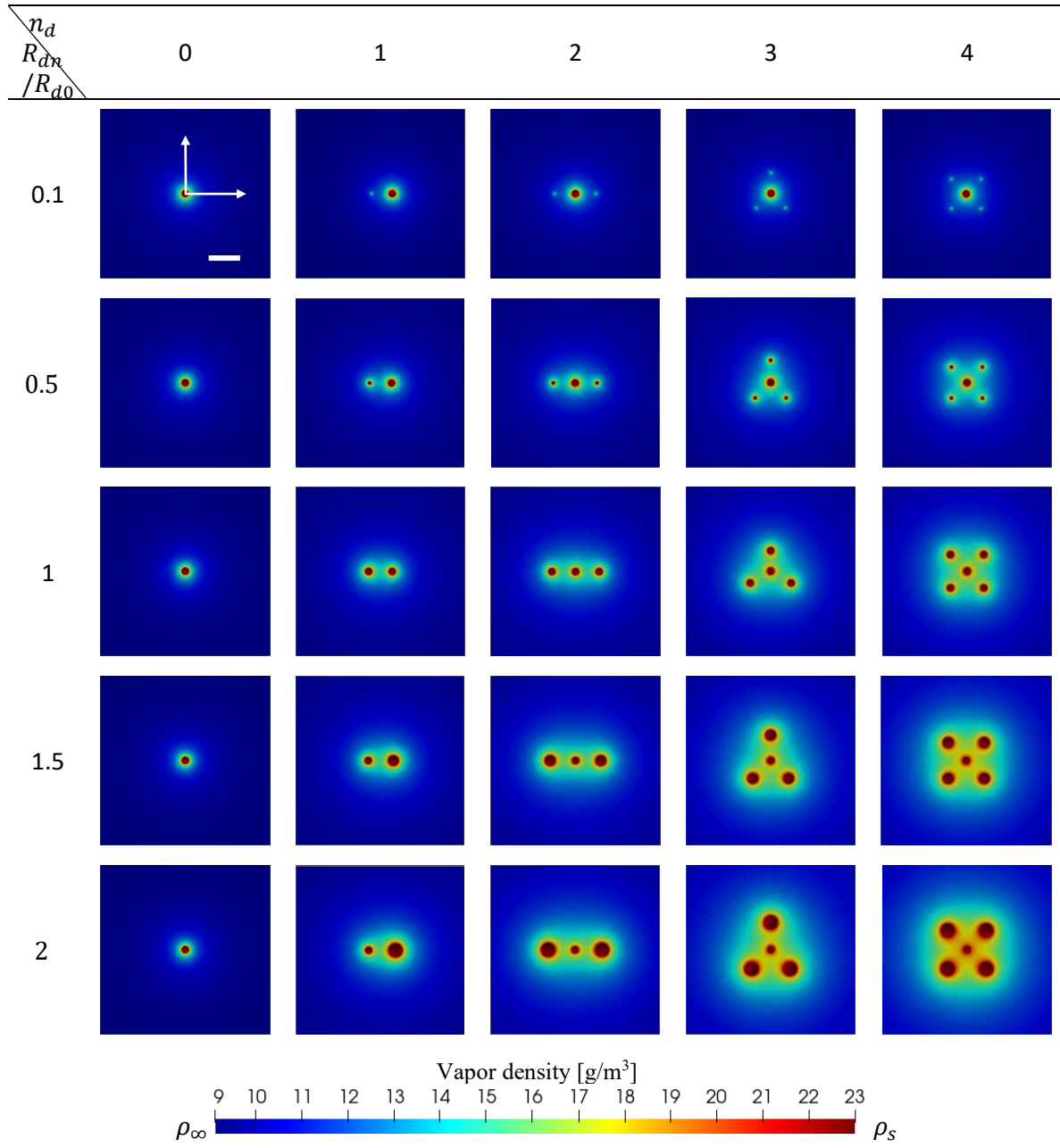


**Fig. 3.6** Effect of adjacent droplet size  $R_{dn}$  and number of adjacent droplets  $n_d$  on vapor density distribution in the  $xy$ -plane at the bottom of the simulation domain for

constant contact angle  $\theta = 50^\circ$  and separation distance  $d_s = 10R_d$ , where  $R_d = 1\text{mm}$ .

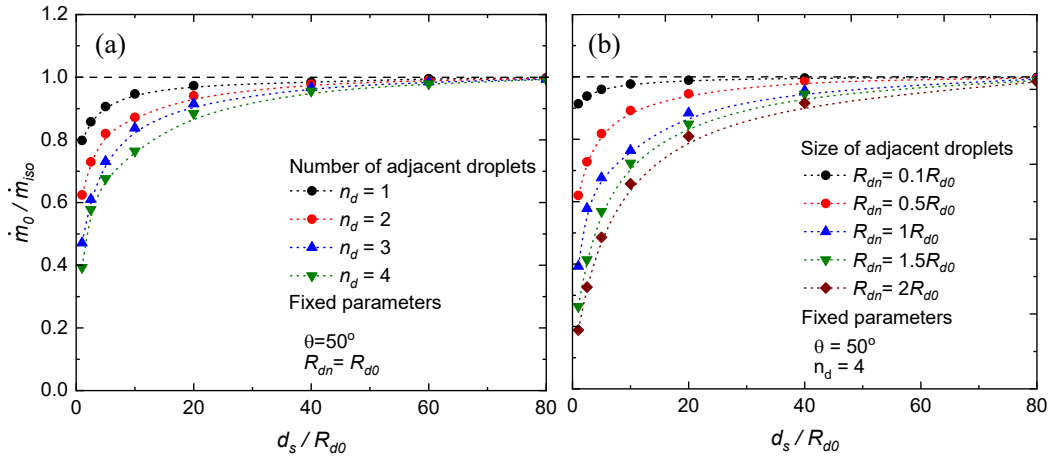


**Fig. 3.7** Effect of the number of adjacent droplets  $n_d$ , size of adjacent droplets  $R_{dn}$  and dimensionless separation distance  $d_s/R_d$  on (a) the evaporation rate of the reference droplet normalized by the evaporation rate of the isolated droplet  $\dot{m}_o/\dot{m}_{iso}$ .

Figure 3.7 shows the relationships plotted between the number of adjacent droplets, size of adjacent droplets and separation distance against the evaporation rate of the reference droplet normalized evaporation rate  $\dot{m}_o/\dot{m}_{iso}$ . The number of the adjacent droplets  $n_d$  ranges between 1 and 4. The size of the adjacent droplet  $R_{dn}$  ranges between  $0.1R_{d0}$  and  $2R_{d0}$ . The separation distance ranges between 0 and  $80R_{d0}$ . A value of one for the ratio  $\dot{m}_o/\dot{m}_{iso}$  (dashed line) indicates that the reference droplet's evaporation rate was identical to that of the isolated droplet under identical conditions. Notably,  $\dot{m}_o/\dot{m}_{iso}$  significantly decreased with a decrease in  $d_s/R_d$ , showing that the separation distance was a primary factor in the reduction of the evaporation rate of droplet arrays. This is in corresponding to in Fig. 3.5, the local vapor density near the reference droplet relatively increased in the presence of adjacent droplets when the separation distance decreased. Apparently, an extended saturated vapor cloud

surrounding the reference droplet hindered vapor diffusion in the computation domain, resulting in the reduction of  $\dot{m}_o/\dot{m}_{iso}$  irrespective of the contact angle. As the separation distance increased is increase to  $80R_{d0}$ ,  $\dot{m}_o/\dot{m}_{iso}$  approached unity, and the reference droplet's evaporation resembled that of an isolated droplet. The additional dependence of  $\dot{m}_o/\dot{m}_{iso}$  on the number of adjacent droplets and size of adjacent droplets can be readily discerned in Fig. 3.7(a) and (b), respectively. It shows that the number of adjacent droplets and size of adjacent droplets were a secondary factor influencing the evaporation rate of droplet arrays. In particular, deviations of  $\dot{m}_o/\dot{m}_{iso}$  from unity became significant as the number and size of the adjacent droplet increased. This is because the area of the saturated vapor cloud surrounding the reference droplet increased as shown in Fig. 3.5 and Fig.3.6, respectively.

The effect of the separation distance  $d_s$  on the temporal variation of temperature  $T$ , relative humidity  $RH$ , contact radius  $R_d$ , contact angle  $\theta$ , volume  $V$  and evaporation rate has been presented in Fig. 3.8. The black and colored symbols represent the isolated and arrayed droplets, respectively. The separation distance  $d_s$  is selected as 5, 10 and 15 times of  $R_{d0}$ . The configuration of droplet array is set to  $n_d = 4$  and  $R_{dn} = R_{d0}$ . Figure 3.8(a) and (b) shows that  $T$  and  $RH$  for all the cases remains constant to be  $25^\circ\text{C}$  and  $40\%$ , respectively. Therefore, their role in determining the role of the  $d_s$  can be ignored. Figure 3.8(c) and (d) shows that the reference droplet evaporates in constant contact radius (CCR), constant contact angle (CCA) and mix modes. Figure 3.8(c) shows that the CCR mode of the evaporation extends for the reference droplet as the separation distance decreases. Similarly, Fig. 3.8(d) shows that CCA modes also extended for the reference droplet as the separation distance decreases. Figure 3.8(e) shows that the

evaporation time extends for the reference droplet as the separation distance decreases. When the separation distance is reduced to  $5R_{d0}$ , the evaporation time increases from 600 to 1100s for reference droplet in comparison to the isolated droplet. The evaporation gradient is calculated by taking gradient of the mass time curve through curve fitting using MATLAB. Figure 7(f) shows that during the early stage of evaporation, the evaporation rate of the isolated droplet is highest as compared to the reference droplet surrounded by adjacent droplets. The decreases of the separation distance will decrease the evaporation rate in the early stage in comparison to the isolated droplet. However, a pivot point exists approximately in the middle of the evaporation time when the trend of the evaporation rate will be inverse. This means that the reference droplet will evaporate at a higher rate than compared to the isolated droplet. This is because the surface area of the isolated droplet becomes significantly lower after this point in comparison to the reference droplet and therefore the evaporation rate decreases after the pivot point. The effect of the contribution of the separation distance on evaporation mode has been depicted in Fig. 3.9. As consistent with Fig. 3.8(c) and (d), the duration of the CCR and CCA mode for reference droplet evaporation is extended when the separation distance decreases. This is due to the slower change of the droplet shape and longer pinning period resulting from the presence of adjacent droplets. However, the separation distance has negligible influence on the mix mode of evaporation of reference droplets. Therefore, the time spent by the reference droplet in mix mode of evaporation is of same order to the isolated droplet irrespective of the separation distance.



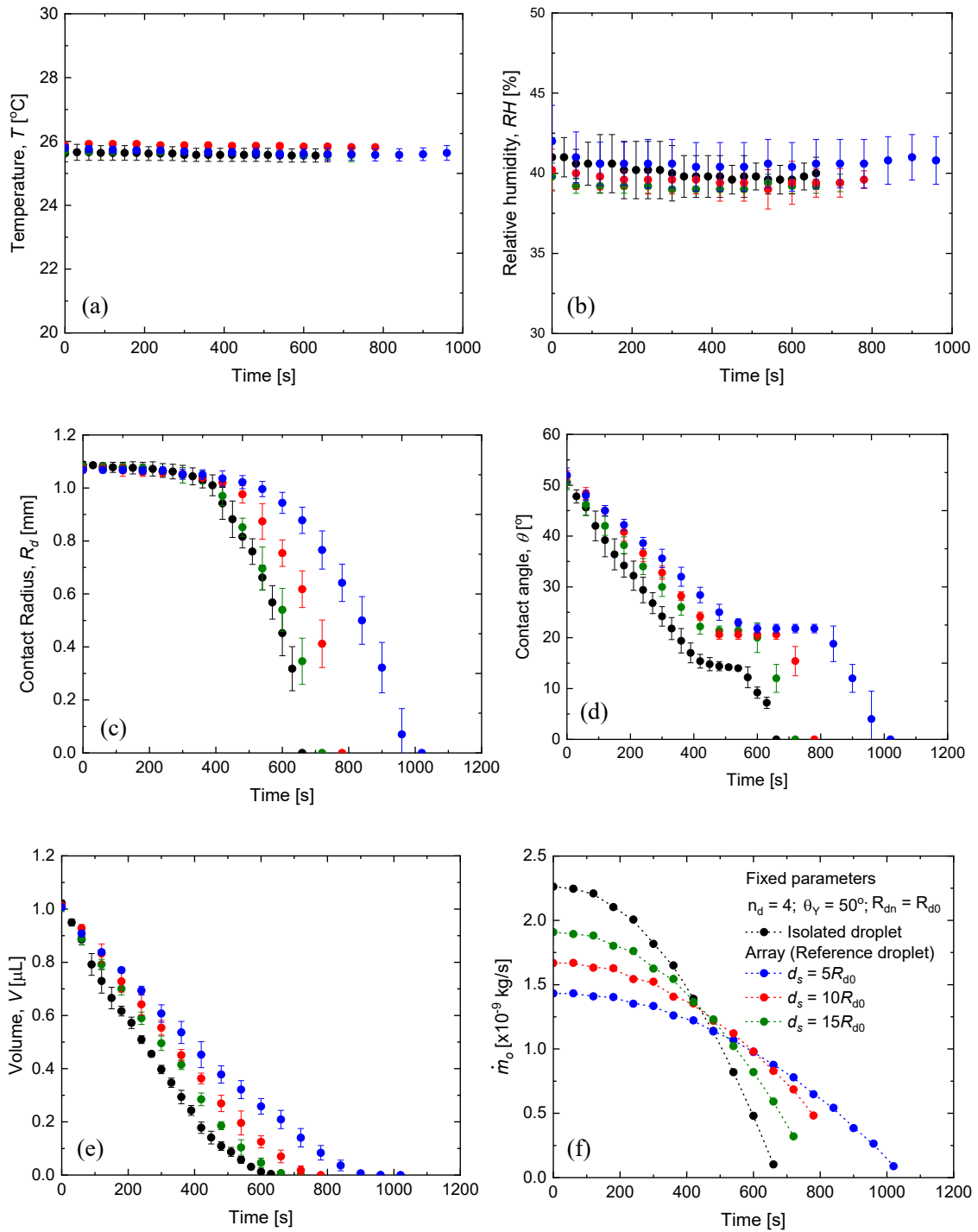


**Fig. 3.8** Effect of separation distance on temporal variations of the measured (a) temperature, (b) relative humidity, (c) contact radius, (d) contact angle, (e) droplet volume during droplet evaporation in array, and (f) evaporation rate. The configuration of droplet array is set to  $n_d = 4$  and  $R_{dn} = R_{d0}$ .

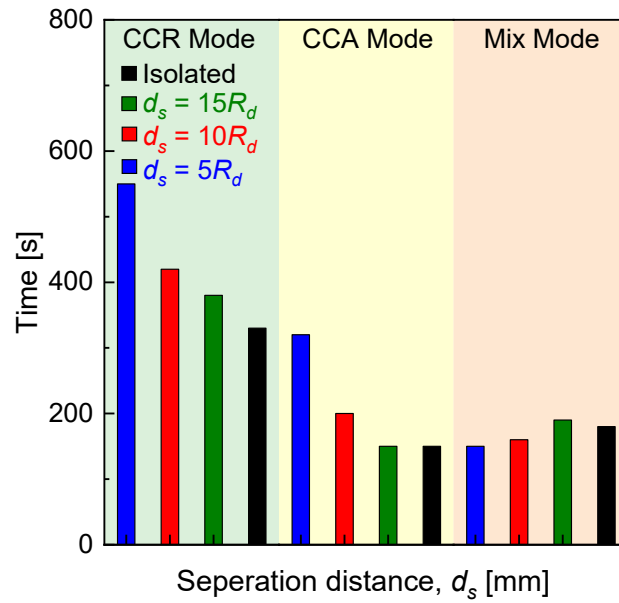


**Fig. 3.9** Effect of separation distance on evaporation mode of the reference droplet. The configuration of droplet array is set to  $n_d = 4$  and  $R_{dn} = R_{d0}$ .

The effect of the number of adjacent droplets  $n_d$  on the temporal variation of temperature  $T$ , relative humidity  $RH$ , contact radius  $R_d$ , contact angle  $\theta$ , volume  $V$  and evaporation rate has been presented in Fig. 3.10. The black and colored symbols represent the isolated and arrayed droplets, respectively. The number of adjacent droplets  $n_d$  is selected as 1, 2 and 4, respectively. The configuration of droplet array is set to  $R_{dn} = R_{d0}$  and  $d_s = 5R_{d0}$ . Fig. 3.10 (a) and (b) shows that  $T$  and  $RH$  for all the cases remains constant to be  $25^\circ\text{C}$  and  $40\%$ , respectively. Therefore, their role in determining the role of the  $n_d$  can be ignored. Figure 3.10 (c) and (d) shows that the reference droplet evaporates in constant contact radius (CCR), constant contact angle (CCA) and mix modes. Figure 3.10(c) shows that the CCR mode of the evaporation increases for the reference droplet as the number of adjacent droplets increases. Similarly, Fig. 3.10(d) shows that CCA modes also extended for the reference droplet as the number of adjacent droplets increases. Figure 3.10(e) shows that the evaporation

time extends for the reference droplet as number of adjacent droplets increases. When the number of adjacent droplets is 4, the evaporation time increases from 600 to 1100s for reference droplet in comparison to the isolated droplet.

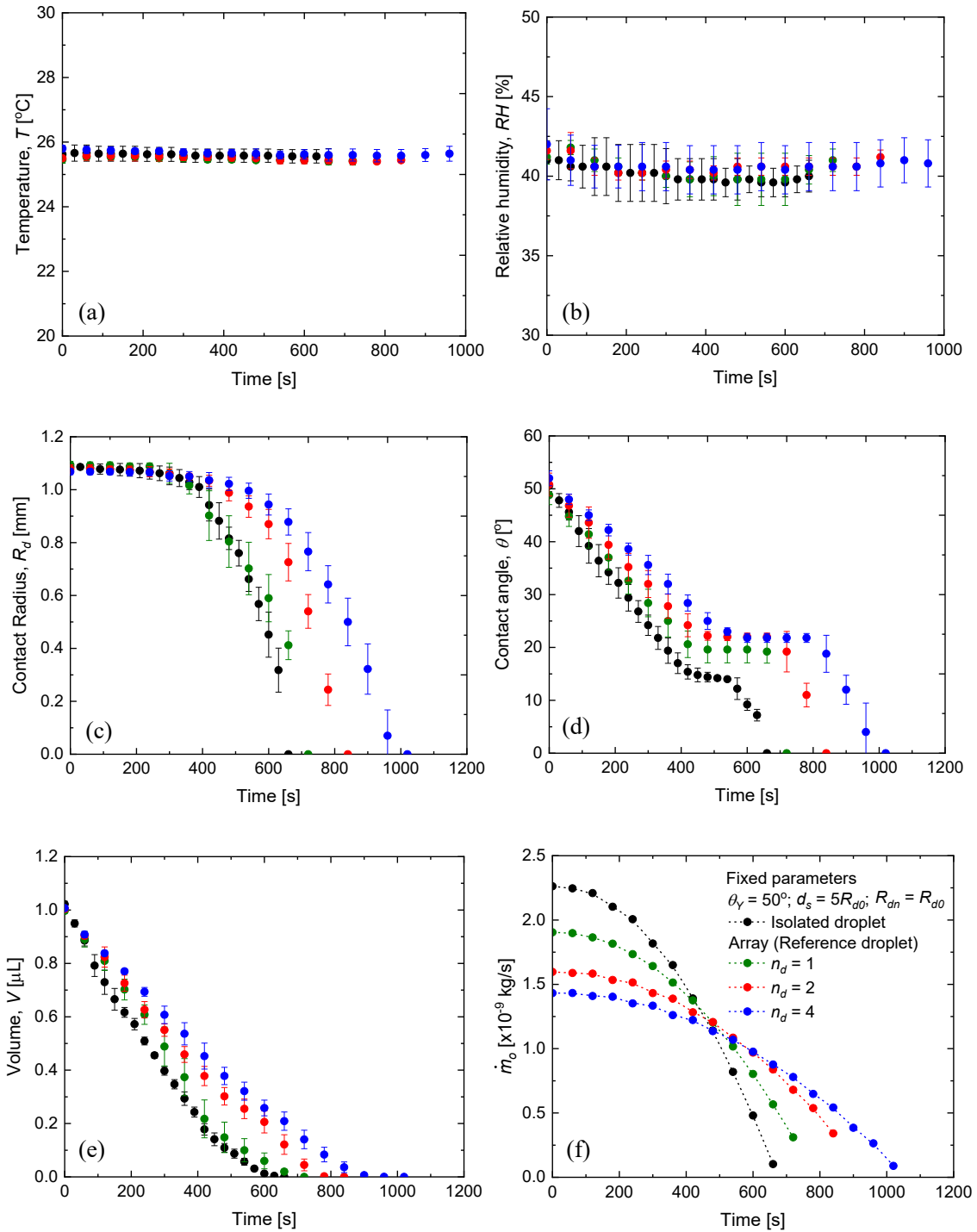


**Fig. 3.10** Effect of number of adjacent droplets on temporal variations of the measured (a) temperature, (b) relative humidity, (c) contact radius, (d) contact angle, (e) droplet volume during droplet evaporation in array. The configuration of droplet array is set to  $n_d = 4$  and  $R_{dn} = R_{d0}$ .

The evaporation gradient is calculated by taking gradient of the mass time curve through curve fitting using MATLAB. Figure 3.10(f) shows that during the early stage of evaporation, the evaporation rate of the isolated droplet is highest as compared to the reference droplet surrounded by adjacent droplets. The increase in the number of adjacent droplets will decrease the evaporation rate in the early stage in comparison to the isolated droplet. The effect of the contribution of the number of adjacent droplets on evaporation mode has been depicted in Fig. 3.11.

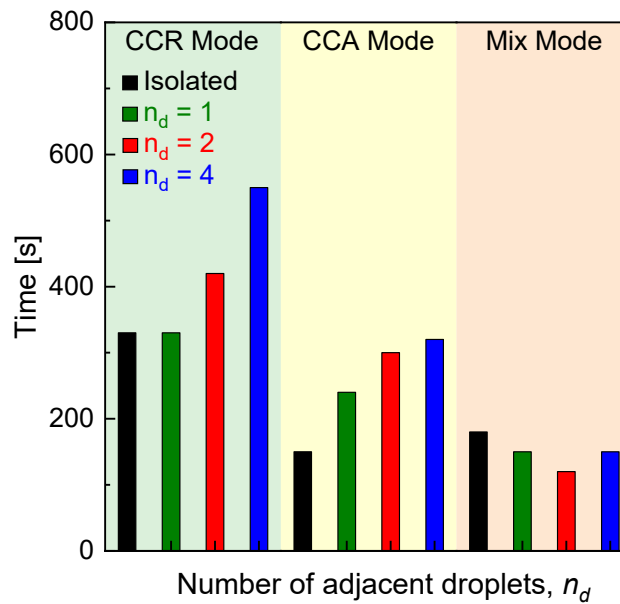


**Fig. 3.11** Effect of number of adjacent droplet on evaporation mode of the reference droplet. The configuration of droplet array is set to  $R_{dn} = R_{d0}$  and  $d_s = 5R_{d0}$ .

As consistent with Fig. 3.10(c) and (d), the duration of the CCR and CCA mode for reference droplet evaporation is extended. This is due to the slower change of the

droplet shape and longer pinning period resulting from the presence of adjacent droplets. However, the number of adjacent droplets has negligible influence on the mix mode of evaporation of reference droplets. Therefore, the time spent by the reference droplet in mix mode of evaporation is of same order to the isolated droplet.

The effect of the size of adjacent droplets  $R_{dn}$  on the temporal variation of temperature  $T$ , relative humidity  $RH$ , contact radius  $R_d$ , contact angle  $\theta$ , volume  $V$  and evaporation rate has been presented in Fig. 3.12. The black and colored symbols represent the isolated and arrayed droplets, respectively. The size of adjacent droplets  $R_{dn}$  is selected as 0.8, 1 and 1.5, respectively. The configuration of droplet array is set to  $n_d = 4$  and  $d_s = 5R_{d0}$ . Figure 3.12(a) and (b) shows that  $T$  and  $RH$  for all the cases remains constant to be  $25^\circ\text{C}$  and 40%, respectively. Therefore, their role in determining the role of the  $R_{dn}$  can be ignored. Figure 3.12 (c) and (d) shows that the reference droplet evaporates in constant contact radius (CCR), constant contact angle (CCA) and mix modes. Figure 3.12(c) shows that the CCR mode of the evaporation increases for the reference droplet as the number of adjacent droplets increases. Similarly, Fig. 3.12(d) shows that CCA modes also extended for the reference droplet as the size of adjacent droplets increases. Figure 3.12(e) shows that the evaporation time extends for the reference droplet as size of adjacent droplets increases. When the size of adjacent droplets is 1.5, the evaporation time increases from 600 to 1200s for reference droplet in comparison to the isolated droplet. The evaporation gradient is calculated by taking gradient of the mass time curve through curve fitting using MATLAB. Figure 3.12 (f) shows that during the early stage of evaporation, the evaporation rate of the isolated droplet is highest as compared to the reference droplet surrounded by adjacent droplets.

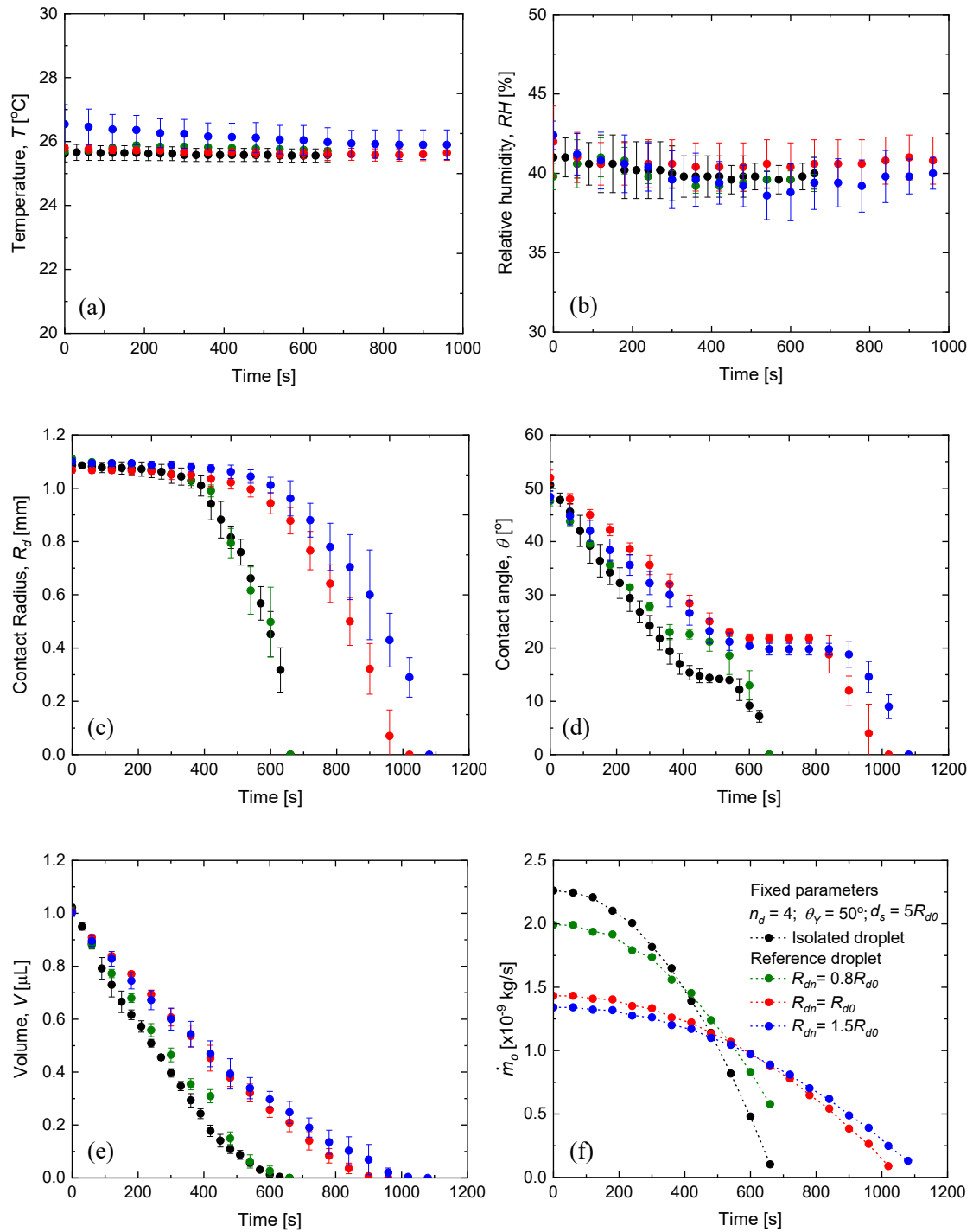


**Fig. 3.12** Effect of size of adjacent droplets on temporal variations of the measured (a) temperature, (b) relative humidity, (c) contact radius, (d) contact angle, (e) droplet volume during droplet evaporation in array, and (f) evaporation rates. The configuration of droplet array is set to  $n_d = 4$  and  $d_s = 5R_{d0}$ .

The increase in the size of adjacent droplets will decrease the evaporation rate in the early stage in comparison to the isolated droplet. The effect of the contribution of the size of adjacent droplets on evaporation mode has been depicted in Fig. 3.13. As consistent with Fig. 3.12(c) and (d), the duration of the CCR and CCA mode for reference droplet evaporation is extended. This is due to the slower change of the droplet shape and longer pinning period resulting from the presence of adjacent droplets. However, the size of adjacent droplets has negligible influence on the mix mode of evaporation of reference droplets. Therefore, the time spent by the reference droplet in mix mode of evaporation is of same order to the isolated droplet.

The transient experimental data and steady numerical simulation has been compared in Fig. 3.14 for time  $t = 0s$ . It is found that the transient experiment at the initial time is well validated with the numerical simulations for the cases that include the effects of the separation distance, number of adjacent droplets and size of the adjacent droplets.

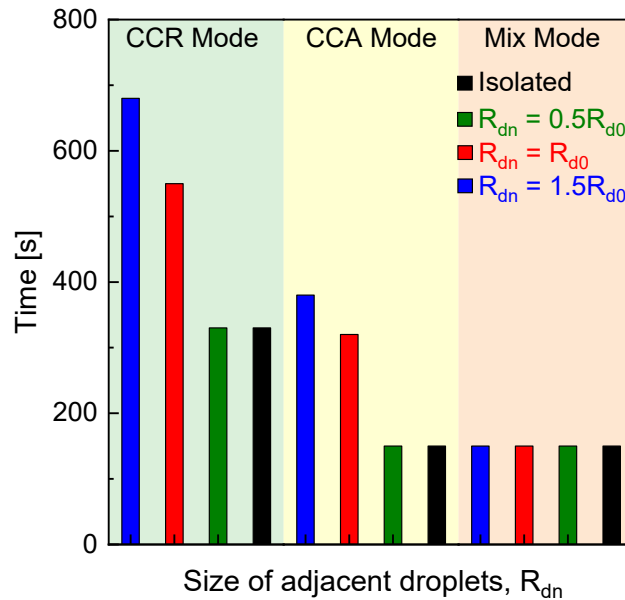


**Fig. 3.13** Effect of size of adjacent droplets on evaporation mode of the reference droplet. The configuration of droplet array is set to  $n_d = 4$  and  $d_s = 5R_{d0}$ .

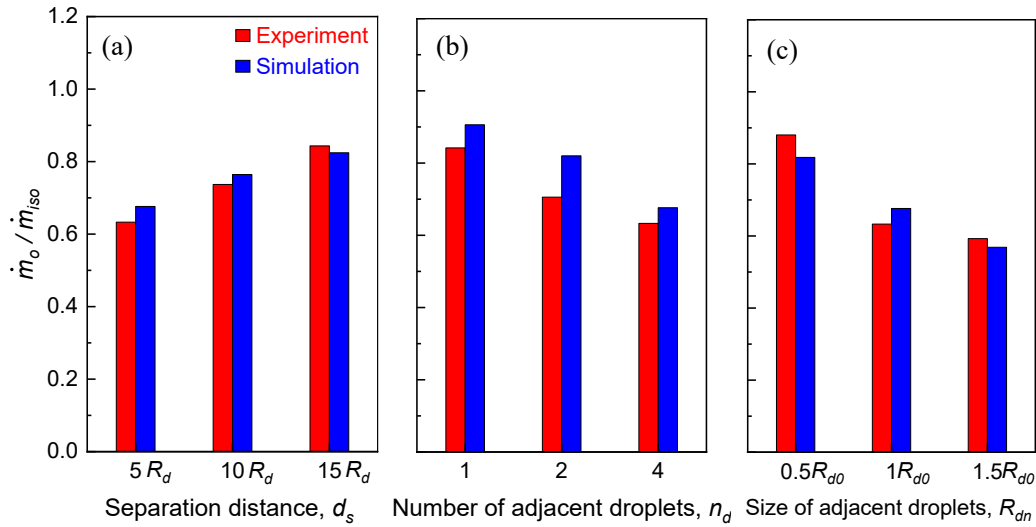


**Fig. 3.14** Validation between experiment and theory for on evaporation mode of the reference droplet normalized with the isolation droplet in given range of (a) separation distance, (b) number of adjacent droplets, and (c) size of adjacent droplets.

### 3.3 Effect of surface wettability on evaporation rate of droplet array

#### 3.3.1 Problem definition and theoretical modeling

An array of  $N$  water droplets is considered to evaporate on flat hydrophilic and hydrophobic surfaces. The central droplet of the array is considered as the reference droplet, and it is surrounded by  $n_d$  (1–4) adjacent droplets in different configurations as shown in Fig. 3.15. The reference droplet is separated from its adjacent droplets by a constant distance  $d_s$  [mm] that ranges from 0 to  $80 R_d$ , where  $R_d$  [mm] is the contact radius of reference droplet. All the droplets in the array have identical  $R_d$  and identical contact angle  $\theta$ . The ambient temperature  $T$  and relative humidity  $RH$  are maintained



constant at 25°C and 40%, respectively. Vapor continuously diffuses from the lv interface with saturation density  $C_s$  [g/m<sup>3</sup>] to the ambient with density  $C_\infty$ . The external and internal flows in the liquid and gas regimes, respectively, are considered too weak to influence the evaporation rate[35,81]. Furthermore, the effect of gravity on the shape of the droplets is negligible since  $R_d$  is smaller than the capillary length (sessile droplets)[21]. For an isolated droplet with an arbitrary contact angle evaporating on a flat surface, the instantaneous evaporation rate  $\dot{m}_{iso}$  [kg/s] is given by[66]

$$\dot{m}_{iso} = -2\pi R_d D(T)(C_s - C_\infty) \frac{1}{\sqrt{1+\cos\theta}}, \quad (3-3)$$

where the diffusion coefficient  $D(T) = 22.5 \times 10^{-6} (T/273.15)^{1.8}$  [m<sup>2</sup>/s][83].

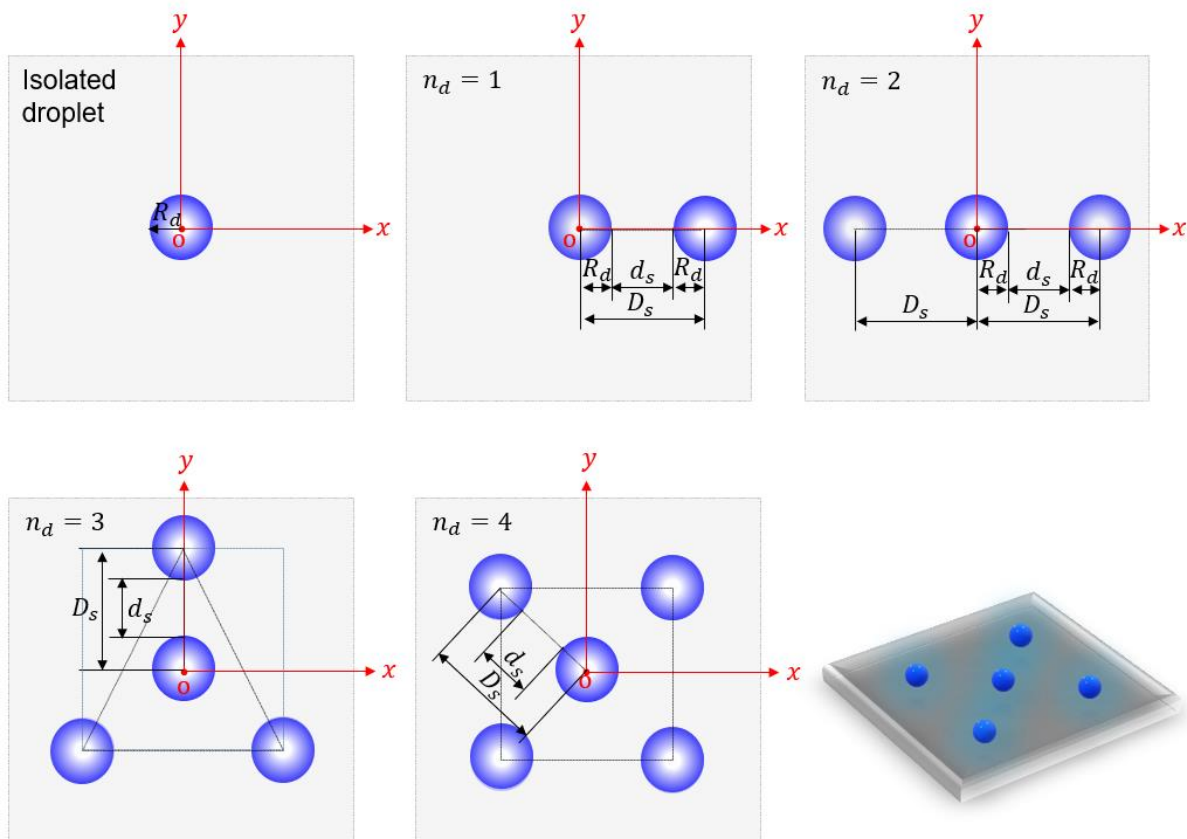


**Fig. 3.15** Schematics of droplet array configurations. The origin of co-ordinate system is located at center of the reference droplet.

The vapor density  $\rho_s$  at the lv interface is considered to be saturated at ambient temperature  $T$  and is calculated using  $C_s(T) = MP_s(T)/R_gT$ , where  $P_s(T)$  [Pa] is the saturated partial vapor pressure,  $M$  [kg/mol] is the vapor molecular weight, and  $R_g$  [J/(mol·K)] is the universal gas constant. The ambient density at a specific relative humidity  $RH$  is calculated using  $\rho_\infty = RH \times \rho_s(T)$ . For the reference droplet surrounded by  $n_d$  adjacent droplets, the evaporation rate  $\dot{m}_o$  is calculated using Wray *et al.*'s model[94]:

$$\dot{m}_o = \dot{m}_{iso} - \frac{2}{\pi} \sum_{k=1}^N \dot{m}_{ad,k} \sin^{-1} \left( \frac{R_d}{D_{s,k}} \right). \quad (3-4)$$

Here,  $D_s$  [mm] is the distance between the centers of two adjacent droplets in the array, and it is given by  $D_s = d_s + 2R_d$  as shown in Fig. 3.15,  $\dot{m}_{ad}$  is the evaporation rate of adjacent droplets, and  $k$  corresponds to the number of individual droplet in array ranging from 1 to  $N$  (total number of droplets). The evaporation rates  $\dot{m}_o$  and  $\dot{m}_{ad}$  are analogous to the evaporation flux  $\dot{m}/A_{lv}$  because the surface area of the lv interface, given by  $A_{lv} = 2\pi R_d^2/(1 + \cos\theta)$  [mm<sup>2</sup>], is identical for all the droplets. However,  $\dot{m}_o$  and  $\dot{m}_{ad}$  are unknown and depend on vapor interactions between the droplets. Therefore, Eq. (3-2) is a system of  $N \times N$  linear equations that should be solved simultaneously. To simplify Eq. (3-2), Edwards *et al.*[78] rewrote the system of equations in a square matrix as follows:

$$\dot{m}_o = \Phi^{-1} \dot{m}_{iso}, \quad (3-5)$$

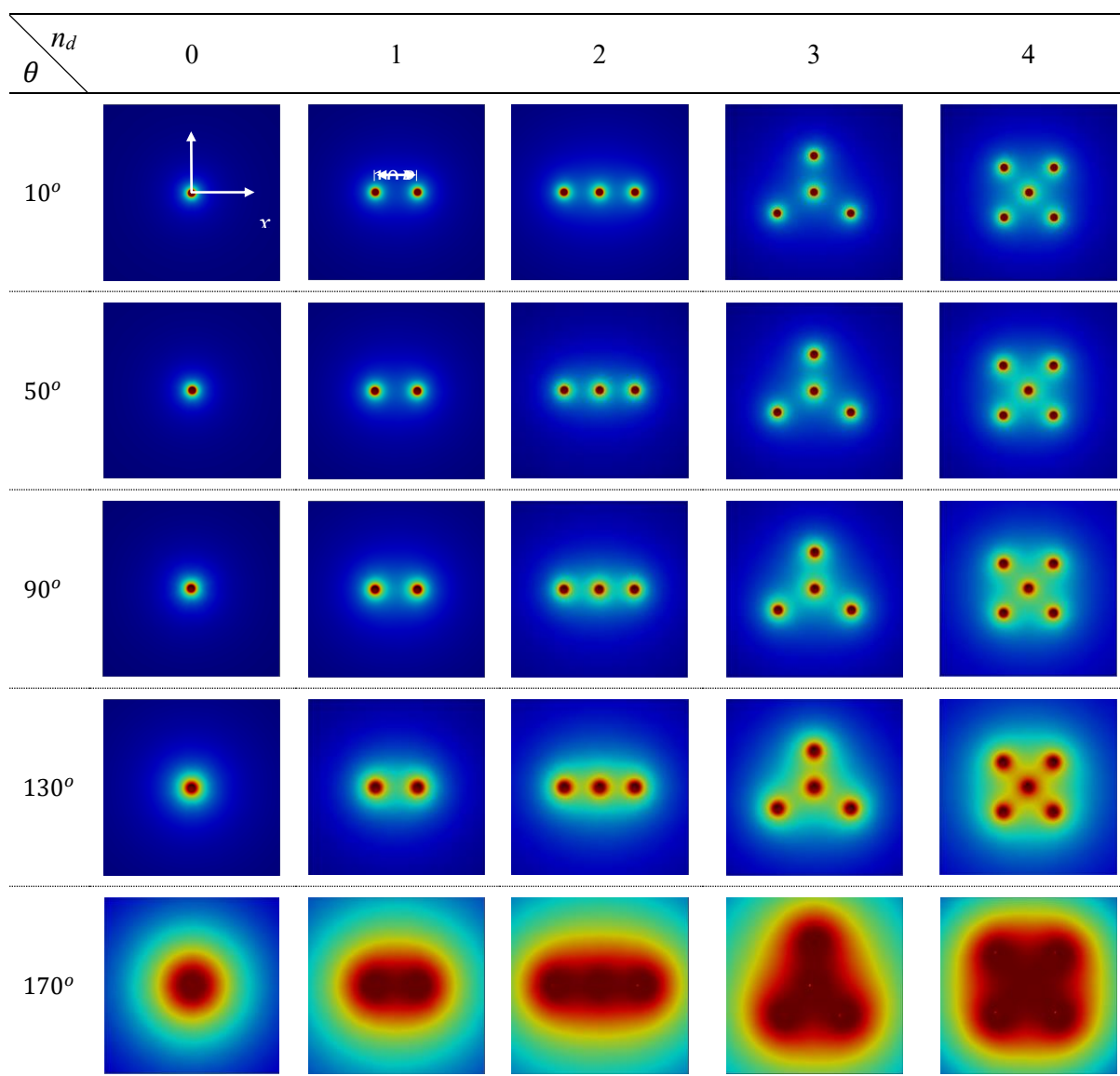
where  $\Phi$  is an  $N \times N$  suppression matrix. The off-diagonal elements capturing the interactions between droplets can be calculated as  $\Phi_{ij} = \frac{2}{\pi} \sin^{-1} \left( \frac{R_d}{D_{s,ij}} \right)$ ; the diagonal elements represent the interaction of a droplet with itself and hence are one. Here, the subscripts  $i$  and  $j$  represent the row and column of the suppression matrix  $\Phi$ . For the prediction of the evaporation rate of reference droplet  $\dot{m}_o$  in Eq. (3-5), the suppression matrix  $\Phi$  can be reduced to the order  $1 \times N$  while matrix  $\dot{m}_{iso}$  contains constants with an order of  $N \times 1$ . Further information about the model can be found in the supplementary material of Edwards *et al.*[78]. Since the effect of surface wettability is ignored in Eq. (3-5), we propose a contact angle function  $f(\theta)$  to improve Wray *et al.*'s model as follows:

$$\dot{m}_o = \Phi^{-1} \dot{m}_{iso} f(\theta). \quad (3-6)$$

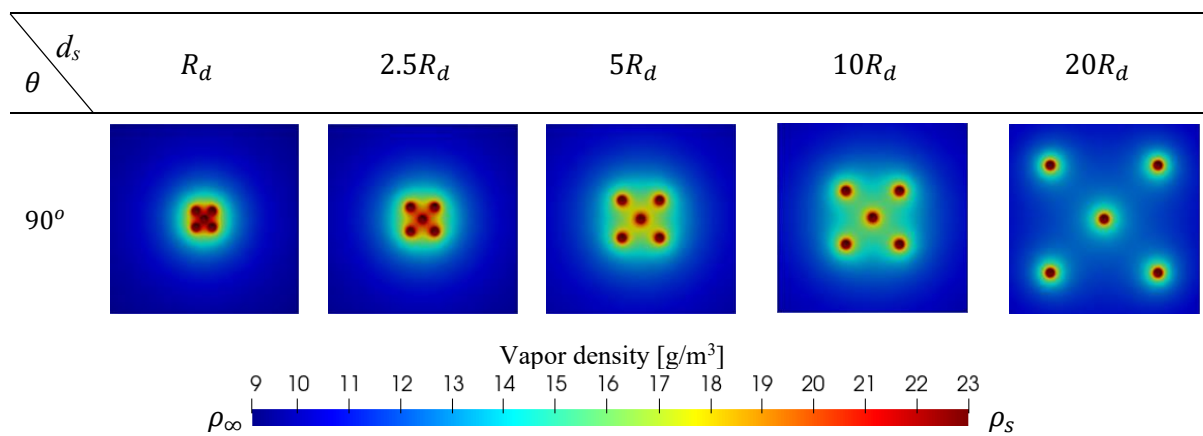
Here,  $f(\theta)$  was obtained through three-dimensional numerical simulations by solving Fick's first and second laws for mass transfer in the steady state.

### 3.3.2 Result and discussion

The vapor density distribution in the  $xy$ -plane at the bottom of the simulation domain is shown in Fig. 3.16, and the normalized local vapor density along the  $z$ -axis is shown in Fig. 3.17. For a given contact angle  $\theta$ , an increase in the number of adjacent droplets  $n_d$  increased the vapor density near the reference droplet, thereby suppressing the reference droplet's evaporation rate. For a given  $n_d$ , the vapor density near the reference droplet increased significantly as the contact angle increased. This implies that the vapor density profiles in the diffusion domain depended on the surface wettability.



(a)



(b)

**Fig. 3.16** Vapor density distribution in the  $xy$ -plane at the bottom of the simulation domain: (a) effect of contact angle  $\theta$  and number of adjacent droplets  $n_d$  for  $d_s = 10 R_d$ , where  $R_d = 1\text{mm}$ , and (b) effect of separation distance  $d_s$  for  $\theta = 90^\circ$ .

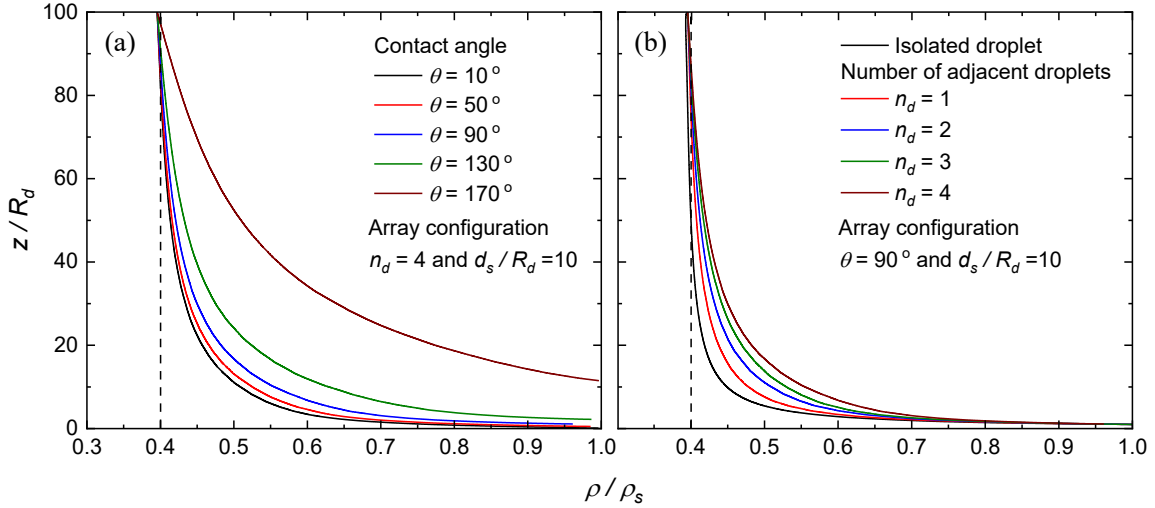


**Fig. 3.17** Normalized vapor density along the  $z$ -axis for droplet evaporation in an array for (a) different contact angles and (b) different numbers of adjacent droplets. The dotted lines represent  $RH=40\%$ .

Figure 3.18 shows the relationships between the contact angle, dimensionless separation distance  $d_s/R_d$ , and the evaporation rate of the reference droplet ( $n_d = 4$ ). In Fig. 3.18(a), the normalized evaporation rate  $\dot{m}_o/\dot{m}_{iso}$  (based on Eq. 3-5) of the reference droplet is plotted against  $d_s/R_d$  in the contact angle range  $10^\circ$ – $170^\circ$ . A value of one for the ratio  $\dot{m}_o/\dot{m}_{iso}$  (dashed line) indicates that the reference droplet's evaporation rate was identical to that of the isolated droplet under identical conditions. Notably, the larger the contact angle of the isolated droplet, the greater was the value of  $\dot{m}_{iso}$ . On the one hand,  $\dot{m}_o/\dot{m}_{iso}$  significantly decreased with a decrease in  $d_s/R_d$ , showing that the separation distance was a primary factor in the reduction of the evaporation rate of droplet arrays. As shown in Fig. 3.16(b), the local vapor density near

the reference droplet relatively increased in the presence of adjacent droplets when the separation distance decreased. Apparently, an extended saturated vapor cloud surrounding the reference droplet hindered vapor diffusion in the computation domain, resulting in the reduction of  $\dot{m}_o/\dot{m}_{iso}$  irrespective of the contact angle. As the separation distance increased,  $\dot{m}_o/\dot{m}_{iso}$  approached unity, and the reference droplet's evaporation resembled that of an isolated droplet. On the other hand, the dependence of  $\dot{m}_o/\dot{m}_{iso}$  on the contact angle can be readily discerned in Fig. 3.18(a), showing that the contact angle was a secondary factor influencing the evaporation rate of droplet arrays. In particular, deviations of  $\dot{m}_o/\dot{m}_{iso}$  from unity became significant as the contact angle increased. This is because the area of the saturated vapor cloud surrounding the reference droplet increased with the contact angle, as shown in Fig. 3.16(a) (right most column of  $n_d = 4$ ). It was found that  $\dot{m}_o/\dot{m}_{iso}$  was close to unity at  $d_s/R_d = 80$  for the cases with  $\theta \leq 130^\circ$ , and a longer separation distance was required for  $\theta = 170^\circ$ . Thus, the separation distance and contact angle are correlated factors that have a synergetic effect on  $\dot{m}_o/\dot{m}_{iso}$ .

Wray *et al.*'s model (Eqs. (3-4) and (3-5)) plotted in Fig. 7(a) (black line) overlapped with the present numerical results for  $\theta = 10^\circ$  (black circle) and  $50^\circ$  (red circle), while it deviated from the numerical results for  $\theta \geq 90^\circ$ , especially in the region of small separation distances. Although we verified that Wray *et al.*'s model [94] is applicable to the hydrophilic droplets in the array, apparently, this model could not capture the effect of the contact angle on the evaporation rate. Since Fig. 3.18(a) shows the importance of surface wettability for predicting the evaporation rate of droplets in the array, surface wettability was incorporated into  $f(\theta)$ , as shown in Eq. (3-6).

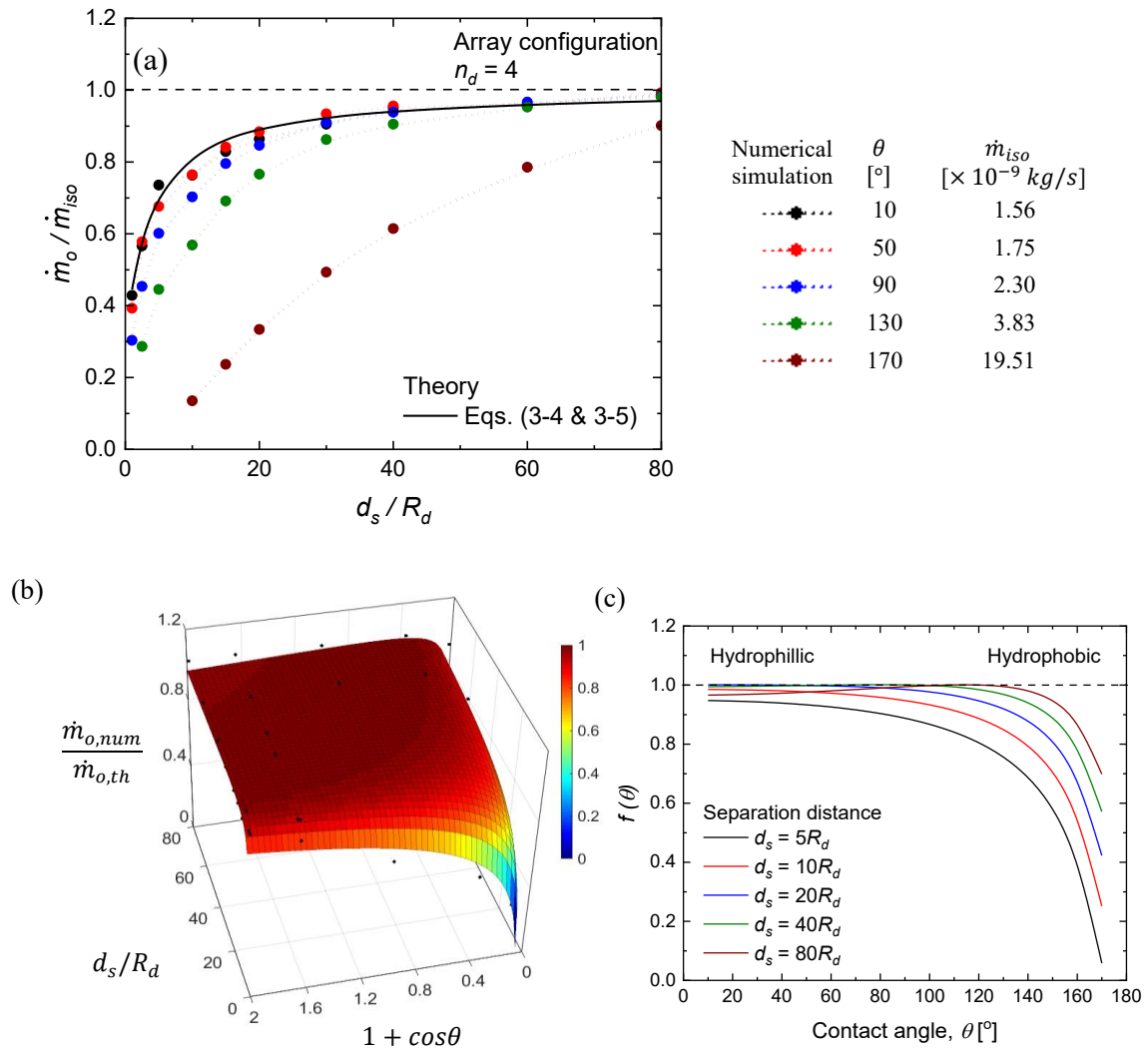


**Fig. 3.18** Effect of the contact angle and dimensionless separation distance  $d_s/R_d$  on (a) the evaporation rate of the reference droplet normalized by the evaporation rate of the isolated droplet  $\dot{m}_o/\dot{m}_{iso}$ , (b) the evaporation rate of the reference droplet normalized by the prediction of Eq. (3-5)  $\dot{m}_{o,num}/\dot{m}_{o,th}$ , and (c) the contact angle function  $f(\theta)$ .

To obtain  $f(\theta)$ , we plotted the numerically determined evaporation rate of the reference droplet normalized by Eq. (3-5),  $\dot{m}_{o,num}/\dot{m}_{o,th}$ , against  $d_s/R_d$  and  $1 + \cos\theta$ , as shown in Fig. 3.18(b). Similar to Fig. 3.18(a), a decrease in the separation distance  $d_s/R_d$  and an increase in the contact angle term  $1 + \cos\theta$  caused a reduction in

$\dot{m}_{0,num}/\dot{m}_{0,th}$ . Through MATLAB[91] analysis,  $f(\theta)$  was obtained by fitting dataset in Fig. 3.18 with a quadratic function as follows:

$$f(\theta) = a + bx + cx^2, \text{ where } x = \ln \left[ \frac{d_s}{R_d} (1 + \cos\theta) \right]. \quad (3-7)$$

The coefficients were calculated to be  $a = 0.7$ ,  $b = 0.176$ , and  $c = -0.023$ , and they were verified to be valid for the investigated cases of the present study. In Fig. 3.18(c),  $f(\theta)$  is plotted as a function of the contact angle and separation distance. For  $f(\theta) = 1$ , Wray *et al.*'s model coincides with the present model for the hydrophilic cases. However,  $f(\theta)$  apparently decreases for the hydrophobic cases, which should be considered in the prediction of the evaporation rate of a droplet in an array on hydrophobic surfaces.

To validate the present model, we performed experiments involving evaporation of droplets in isolation and in an array on flat hydrophilic and hydrophobic surfaces under identical conditions. The time history of experimental data of the evaporating reference droplet on hydrophilic and hydrophobic surfaces is presented in Fig. 3.19. As shown in Figs. 3.19(a) and 3.19(b), temporal variations of the ambient temperature and relative humidity in the measurement cell were small, in the ranges of  $T = 25 \pm 2^\circ\text{C}$  and  $RH = 40 \pm 3\%$ . This eliminated the possibility of the ambient conditions influencing the experimental results. Figs. 3.19(c) and 3.19(d) shows that three evaporation modes, namely constant contact radius (CCR), constant contact angle (CCA), and mixed modes, existed for all cases. For hydrophilic surfaces, the evaporation of the isolated droplet was similar to that of the reference droplet in the array, with the CCR mode being dominant. However, for droplet evaporation on hydrophobic surfaces, the contributions of the CCA and mixed modes were significant.



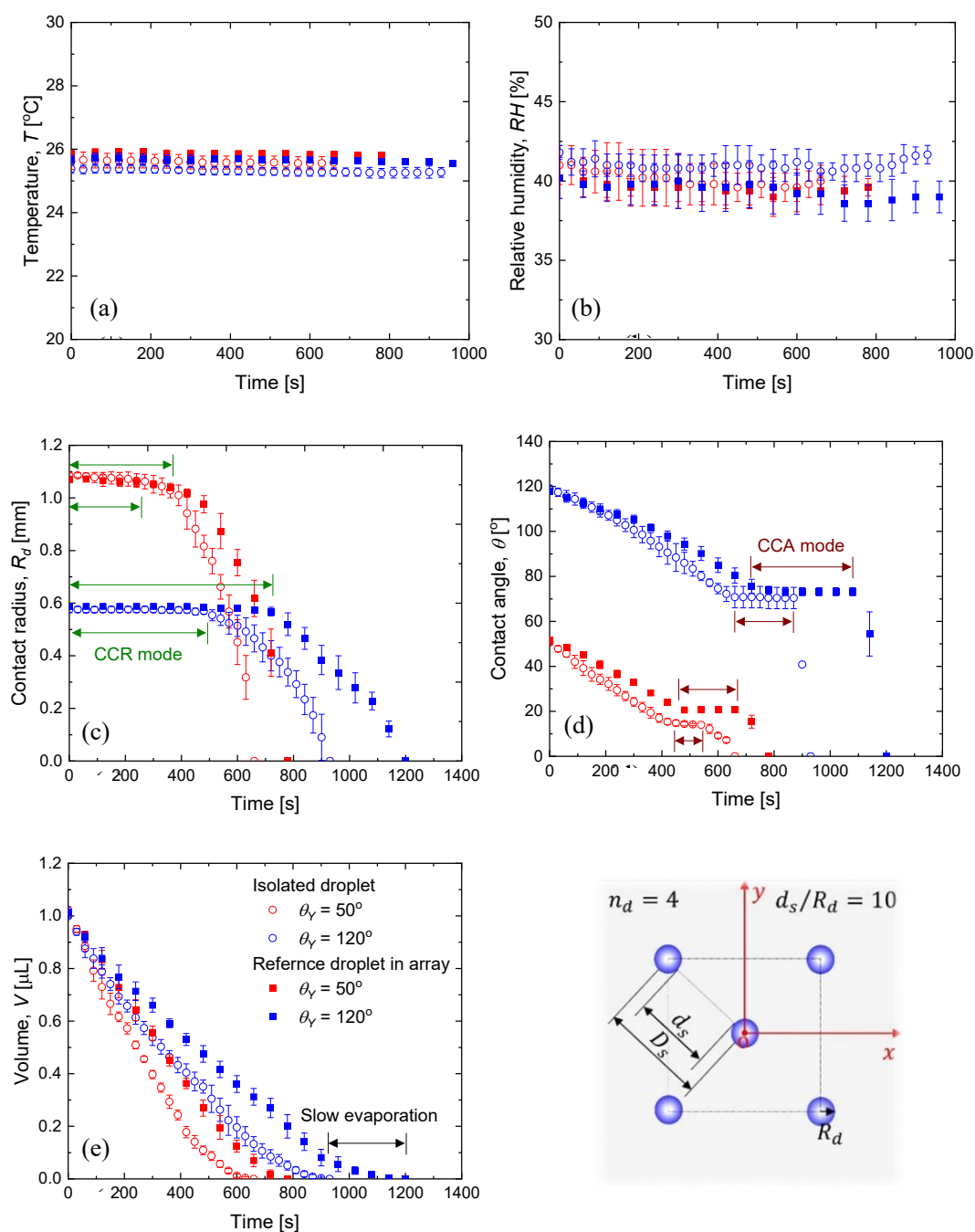


**Fig. 3.19** Temporal variations of the measured (a) temperature, (b) relative humidity, (c) contact radius, (d) contact angle, and (e) droplet volume during droplet evaporation on hydrophilic (red) and hydrophobic surfaces (blue) in isolation (open circles) and in the array (closed squares). The configuration of droplet array is set to  $n_d = 4$  and  $d_s/R_d = 10$ .

Fig. 3.19(c) shows that the CCR mode's duration for the droplet evaporating in the array was longer than that for the isolated droplet. Hydrophobic surfaces showed a longer CCR mode duration than hydrophilic surfaces, due to the slower change of the droplet shape and longer pinning period resulting from the presence of adjacent droplets. Similar results for the durations of the CCA and mixed modes are presented in Fig. 3.19(d), and they show longer durations of these modes for the reference droplet compared with the isolated droplet. Fig. 3.19(e) shows the time history of the droplet volume during evaporation. The reference droplet evaporated slowly, and the evaporation time was longer compared with the isolated droplet. In particular, the reference droplet on a hydrophobic surface evaporated much slower than that on a hydrophilic surface. This confirmed our earlier observation from Fig. 3.18 that the surface wettability should be considered for predicting droplet evaporation in an array.

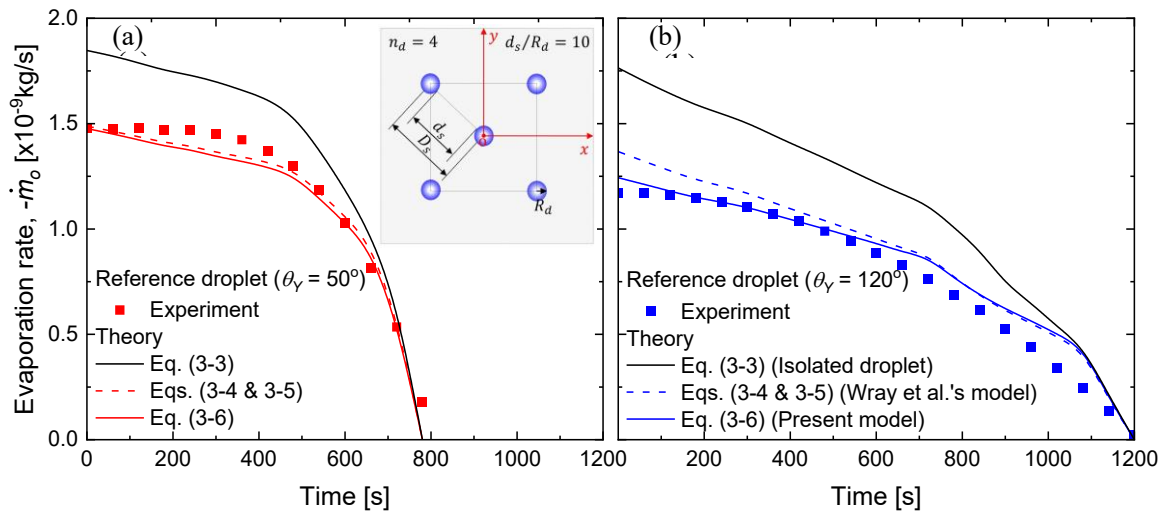


**Fig. 3.20** Theoretical and experimental evaporation rates  $\dot{m}_o$  for a reference droplet on (a) hydrophilic and (b) hydrophobic surfaces. The configuration of droplet array is set to  $n_d = 4$  and  $d_s/R_d = 10$ .

The experimental evaporation rate of the reference droplet,  $\dot{m}_o$ , was calculated from the gradient of the droplet mass against time, and it was linearized using the expression  $\dot{m}_o = f_1(\text{Sin}(t - \pi)) + f_2(t - 10)^{f_3} + 0.95f_4$  in MATLAB[91], where  $t$  is time and  $f_i$  are coefficients. A comparison of the experimentally and theoretically obtained  $\dot{m}_o$  values is shown in Fig. 9. Since Eq. (3-3) was proposed for an isolated droplet's evaporation<sup>14</sup>, it overpredicted evaporation rates on hydrophilic and hydrophobic surfaces. As shown in Fig. 3.20, Eq. (3-3) deviated significantly from the experimental results at the beginning of evaporation. In Fig. 3.20(a), the present model agrees well with Wray *et al.*'s model[94] and with the experimental results for the evaporation rate of the reference droplet on a hydrophilic surface. However, as shown in Fig. 3.20(b), for a hydrophobic surface, the present model disagree with Wray *et al.*'s model[94], but shows good agreement with the experimental evaporation rate of the reference droplet. This observation confirms that surface wettability is an important factor influencing droplet evaporation, especially for hydrophobic surfaces.

### 3.4 Summary

In this chapter we demonstrate that adjacent droplets make a significant contribution to the droplet evaporation. We demonstrate that a droplet in a droplet array evaporates more slowly than an isolated droplet under identical conditions. The reduction on the evaporation rate of the droplet in an array result from the synergetic effect of the separation distance and surface wettability, because of vapor-mediated interactions between droplets. Although the primary factor of the reduction on the evaporation rate is the separation distance, the secondary factor of surface wettability is particularly

important for hydrophobic surfaces. The contact angle function introduced in the present model should not be ignored when predicting the evaporation rates of droplets in an array on hydrophobic surfaces. It was also found that the evaporation rate of the droplet in array decreases monotonously as the number of adjacent droplets increases from one to four. It is further found that decrease in the separation distance between the reference and adjacent droplets in array will decrease evaporation rate of reference droplet. However, the suppression of evaporation rate becomes insignificant when the separation distance becomes greater than 40 times of droplet radius for  $\theta_Y=50^\circ$ . We also demonstrate that, when the radius of the adjacent droplet is ten times smaller than the reference droplet in array, the evaporation rate of reference droplet is not affected irrespective of number of adjacent droplet and separation distance. The insights obtained in the present study are expected to pave the way for wider engineering and medical applications of droplet-array-based devices.

## Chapter 4

# 4 Conclusions and outlook

### 4.1 Conclusions

In this thesis, we provided detailed insights into the contributions of the slv interface toward droplet evaporation on micro/nanostructured surfaces and highlighted the effects of surface wettability and droplet volume. Moreover, the contribution of adjacent droplets to droplet evaporation on flat surfaces was demonstrated, and the effects of array configuration of adjacent droplets and surface wettability were clarified.

The first study estimates the evaporation rate at the slv interface of a droplet on a microstructured surface, based on the difference between the theoretical evaporation rate at the lv interface and the experimental evaporation rate. The scale of slv interface and its contributions to the droplet evaporation were estimated, and the effects of the surface wettability and droplet volume were clarified. For microstructured surfaces, the scale of the slv interface was estimated to be 253–940  $\mu\text{m}$  for a 4  $\mu\text{L}$  water droplet, significantly contributing toward the evaporation rate, in addition to the evaporation at the lv interface. The evaporation rate at the slv interface accounted for 16–48% of the total droplet evaporation rate. The scale of the slv interface and evaporation rate increased with a decrease in the initial contact angle or an increase in the droplet volume.

The second study demonstrates that show that contribution of adjacent droplets to droplet evaporation in array cannot be ignored due to vapor-mediated interactions

between droplets. The contribution of the adjacent droplets to droplet evaporation is realized through theoretical modeling, numerical simulations, and experiments. We found that the evaporation rate of droplets in the array decreases monotonically as the number of adjacent droplets increases. Meanwhile, the evaporation rate reduces with decreasing the distance between the reference droplet and adjacent droplets in the array. However, the suppression of the evaporation rate becomes inconsiderable when the separation distance becomes significantly large. In addition, the evaporation rate of the droplet is not affected when the radius of the adjacent droplet is sufficiently small. We developed a model involving a contact angle function to accurately predict the evaporation rate of droplets on flat surfaces with an arbitrary contact angle in the array. We demonstrate that the contact angle function introduced in the present model should not be ignored when predicting the evaporation rates of droplets in an array on hydrophobic surfaces.

## **4.2 Outlook**

The findings of this study are expected to advance our understanding of droplet evaporation in a wide range of scientific and engineering applications. The current studies only provide basic understanding about the contribution of solid-liquid-vapor (slv) interface and adjacent droplets to droplet evaporation. However, more challenges still exist to advance our understanding of the topics discussed in this thesis.

Thus, in the near future, we would like to perform more theoretical, numerical and experimental investigations about the role of wetting state on the scale and contribution of the sslv interface. Further, we would like to know the role of surface temperature on

the contribution of the slv interface relative to the liquid-vapor (lv) interface. We would further advance on the accurate measurements regarding the scale of the slv interface and direct measurement of the evaporation rate at the slv interface. Since the solid-liquid-vapor (slv) interface also contributes to droplet evaporation, the effect of the slv interface on droplet evaporation in an array will be investigated in a future study.

---

## Reference

- [1] X. Yu, J. Xu, Does sunlight always accelerate water droplet evaporation?, *Appl. Phys. Lett.* 116 (2020) 253903. <https://doi.org/10.1063/5.0012700>.
- [2] I.G. Hwang, J.Y. Kim, B.M. Weon, Droplet evaporation with complexity of evaporation modes, *Appl. Phys. Lett.* 110 (2017) 31602. <https://doi.org/10.1063/1.4974292>.
- [3] C.-C. Hsu, T.-W. Su, C.-H. Wu, L.-S. Kuo, P.-H. Chen, Influence of surface temperature and wettability on droplet evaporation, *Appl. Phys. Lett.* 106 (2015) 141602. <https://doi.org/10.1063/1.4917291>.
- [4] F. Carle, B. Sobac, D. Brutin, Experimental evidence of the atmospheric convective transport contribution to sessile droplet evaporation, *Appl. Phys. Lett.* 102 (2013) 61603. <https://doi.org/10.1063/1.4792058>.
- [5] L. Bansal, S. Hatte, S. Basu, S. Chakraborty, Universal evaporation dynamics of a confined sessile droplet, *Appl. Phys. Lett.* 111 (2017) 101601. <https://doi.org/10.1063/1.4996986>.
- [6] Y. Kita, A. Askounis, M. Kohno, Y. Takata, J. Kim, K. Sefiane, Induction of Marangoni convection in pure water drops, *Appl. Phys. Lett.* 109 (2016) 171602. <https://doi.org/10.1063/1.4966542>.
- [7] A.E. Korenchenko, A.A. Zhukova, Sessile droplet evaporation in the atmosphere of different gases under forced convection, *Phys. Fluids.* 34 (2022) 42102. <https://doi.org/10.1063/5.0084830>.
- [8] A. Paul, P. Dhar, Evaporation kinetics of sessile droplets morphed by substrate



- 
- curvature, *Phys. Fluids*. 33 (2021) 122010. <https://doi.org/10.1063/5.0074882>.
- [9] S. Tonini, G.E. Cossali, E.A. Shchepakina, V.A. Sobolev, S.S. Sazhin, A model of droplet evaporation: New mathematical developments, *Phys. Fluids*. 34 (2022) 73312. <https://doi.org/10.1063/5.0098331>.
- [10] J.D. Benter, J.D. Pelaez-Restrepo, C. Stanley, G. Rosengarten, Heat transfer during multiple droplet impingement and spray cooling: Review and prospects for enhanced surfaces, *Int. J. Heat Mass Transf.* 178 (2021) 121587. <https://doi.org/https://doi.org/10.1016/j.ijheatmasstransfer.2021.121587>.
- [11] I. Langmuir., The Evaporation of Small Spheres, *Phys. Rev.* 12 (1918) 368–370. <https://doi.org/10.1103/PhysRev.12.368>.
- [12] Y.Q. Zu, Y.Y. Yan, Single Droplet on Micro Square-Post Patterned Surfaces – Theoretical Model and Numerical Simulation, *Sci. Rep.* 6 (2016) 19281. <https://doi.org/10.1038/srep19281>.
- [13] F. Villa, M. Marengo, J. De Coninck, A new model to predict the influence of surface temperature on contact angle, *Sci. Rep.* 8 (2018) 6549. <https://doi.org/10.1038/s41598-018-24828-8>.
- [14] J.N. Israelachvili, *Intermolecular and Surface Forces*, Academic, (1992).
- [15] T. Young, III. An essay on the cohesion of fluids, *Philos. Trans. R. Soc. London*. 95 (1805) 65–87. <https://doi.org/10.1098/rstl.1805.0005>.
- [16] S. Dash, S. V Garimella, Droplet Evaporation Dynamics on a Superhydrophobic Surface with Negligible Hysteresis, *Langmuir*. 29 (2013) 10785–10795. <https://doi.org/10.1021/la402784c>.
- [17] A.B.D. Cassie, S. Baxter, Wettability of porous surfaces, *Trans. Faraday Soc.* 40 (1944) 546–551. <https://doi.org/10.1039/TF9444000546>.
-

- 
- [18] R.N. Wenzel, Resistance of Solid Surfaces to Wetting by Water, *Ind. Eng. Chem.* 28 (1936) 988–994. <https://doi.org/10.1021/ie50320a024>.
- [19] G. Nagayama, D. Zhang, Intermediate wetting state at nano/microstructured surfaces, *Soft Matter*. 16 (2020) 3514–3521. <https://doi.org/10.1039/C9SM02513H>.
- [20] A. Bussonnière, M.B. Bigdeli, D.-Y. Chueh, Q. Liu, P. Chen, P.A. Tsai, Universal wetting transition of an evaporating water droplet on hydrophobic micro- and nano-structures, *Soft Matter*. 13 (2017) 978–984. <https://doi.org/10.1039/C6SM02287A>.
- [21] T.W.G. van der Heijden, A.A. Darhuber, P. van der Schoot, Macroscopic Model for Sessile Droplet Evaporation on a Flat Surface, *Langmuir*. 34 (2018) 12471–12481. <https://doi.org/10.1021/acs.langmuir.8b02374>.
- [22] B. Sobac, D. Brutin, Triple-Line Behavior and Wettability Controlled by Nanocoated Substrates: Influence on Sessile Drop Evaporation, *Langmuir*. 27 (2011) 14999–15007. <https://doi.org/10.1021/la203681j>.
- [23] R.G. Picknett, R. Bexon, The evaporation of sessile or pendant drops in still air, *J. Colloid Interface Sci.* 61 (1977) 336–350. [https://doi.org/https://doi.org/10.1016/0021-9797\(77\)90396-4](https://doi.org/https://doi.org/10.1016/0021-9797(77)90396-4).
- [24] K. Gleason, S.A. Putnam, Microdroplet Evaporation with a Forced Pinned Contact Line, *Langmuir*. 30 (2014) 10548–10555. <https://doi.org/10.1021/la501770g>.
- [25] S. Armstrong, G. McHale, R. Ledesma-Aguilar, G.G. Wells, Pinning-Free Evaporation of Sessile Droplets of Water from Solid Surfaces, *Langmuir*. 35 (2019) 2989–2996. <https://doi.org/10.1021/acs.langmuir.8b03849>.
-

- 
- [26] P.L. Kelly-Zion, C.J. Pursell, N. Hasbamrer, B. Cardozo, K. Gaughan, K. Nickels, Vapor distribution above an evaporating sessile drop, *Int. J. Heat Mass Transf.* 65 (2013) 165–172.  
<https://doi.org/https://doi.org/10.1016/j.ijheatmasstransfer.2013.06.003>.
- [27] S. Dehaeck, A. Rednikov, P. Colinet, Vapor-Based Interferometric Measurement of Local Evaporation Rate and Interfacial Temperature of Evaporating Droplets, *Langmuir*. 30 (2014) 2002–2008. <https://doi.org/10.1021/la404999z>.
- [28] F. Carle, S. Semenov, M. Medale, D. Brutin, Contribution of convective transport to evaporation of sessile droplets: Empirical model, *Int. J. Therm. Sci.* 101 (2016) 35–47. <https://doi.org/https://doi.org/10.1016/j.ijthermalsci.2015.10.012>.
- [29] P.L. Kelly-Zion, C.J. Pursell, S. Vaidya, J. Batra, Evaporation of sessile drops under combined diffusion and natural convection, *Colloids Surfaces A Physicochem. Eng. Asp.* 381 (2011) 31–36.  
<https://doi.org/https://doi.org/10.1016/j.colsurfa.2011.03.020>.
- [30] L. Zhang, L. Zhao, E.N. Wang, Stefan flow induced natural convection suppression on high-flux evaporators, *Int. Commun. Heat Mass Transf.* 110 (2020) 104255.  
<https://doi.org/https://doi.org/10.1016/j.icheatmasstransfer.2019.03.020>.
- [31] P.L. Kelly-Zion, J. Batra, C.J. Pursell, Correlation for the convective and diffusive evaporation of a sessile drop, *Int. J. Heat Mass Transf.* 64 (2013) 278–285. <https://doi.org/https://doi.org/10.1016/j.ijheatmasstransfer.2013.04.051>.
- [32] R.D. Deegan, O. Bakajin, T.F. Dupont, G. Huber, S.R. Nagel, T.A. Witten, Capillary flow as the cause of ring stains from dried liquid drops, *Nature*. 389 (1997) 827–829. <https://doi.org/10.1038/39827>.
-

- 
- [33] R.D. Deegan, O. Bakajin, T.F. Dupont, G. Huber, S.R. Nagel, T.A. Witten, Contact line deposits in an evaporating drop, *Phys. Rev. E.* 62 (2000) 756–765. <https://doi.org/10.1103/PhysRevE.62.756>.
- [34] S. Semenov, V.M. Starov, R.G. Rubio, M.G. Velarde, Instantaneous distribution of fluxes in the course of evaporation of sessile liquid droplets: Computer simulations, *Colloids Surfaces A Physicochem. Eng. Asp.* 372 (2010) 127–134. <https://doi.org/https://doi.org/10.1016/j.colsurfa.2010.10.004>.
- [35] M.R. Barmi, C.D. Meinhart, Convective Flows in Evaporating Sessile Droplets, *J. Phys. Chem. B.* 118 (2014) 2414–2421. <https://doi.org/10.1021/jp408241f>.
- [36] M. Kumar, R. Bhardwaj, A combined computational and experimental investigation on evaporation of a sessile water droplet on a heated hydrophilic substrate, *Int. J. Heat Mass Transf.* 122 (2018) 1223–1238. <https://doi.org/https://doi.org/10.1016/j.ijheatmasstransfer.2018.02.065>.
- [37] F. Girard, M. Antoni, S. Faure, A. Steinchen, Evaporation and Marangoni Driven Convection in Small Heated Water Droplets, *Langmuir.* 22 (2006) 11085–11091. <https://doi.org/10.1021/la061572l>.
- [38] F. Girard, M. Antoni, K. Sefiane, On the Effect of Marangoni Flow on Evaporation Rates of Heated Water Drops, *Langmuir.* 24 (2008) 9207–9210. <https://doi.org/10.1021/la801294x>.
- [39] G. Nagayama, T. Matsumoto, K. Fukushima, T. Tsuruta, Scale effect of slip boundary condition at solid–liquid interface, *Sci. Rep.* 7 (2017) 43125. <https://doi.org/10.1038/srep43125>.
- [40] M.A. Kazemi, D.S. Nobes, J.A.W. Elliott, Effect of the Thermocouple on Measuring the Temperature Discontinuity at a Liquid–Vapor Interface, *Langmuir.*
-

- 
- 33 (2017) 7169–7180. <https://doi.org/10.1021/acs.langmuir.7b00898>.
- [41] P. Jafari, A. Masoudi, P. Irajizad, M. Nazari, V. Kashyap, B. Eslami, H. Ghasemi, Evaporation Mass Flux: A Predictive Model and Experiments, *Langmuir*. 34 (2018) 11676–11684. <https://doi.org/10.1021/acs.langmuir.8b02289>.
- [42] G. Nagayama, M. Takematsu, H. Mizuguchi, T. Tsuruta, Molecular dynamics study on condensation/evaporation coefficients of chain molecules at liquid–vapor interface, *J. Chem. Phys.* 143 (2015) 14706. <https://doi.org/10.1063/1.4923261>.
- [43] T.A.H. Nguyen, S.R. Biggs, A. V Nguyen, Analytical Model for Diffusive Evaporation of Sessile Droplets Coupled with Interfacial Cooling Effect, *Langmuir*. 34 (2018) 6955–6962. <https://doi.org/10.1021/acs.langmuir.7b03862>.
- [44] X. Xu, L. Ma, Analysis of the effects of evaporative cooling on the evaporation of liquid droplets using a combined field approach, *Sci. Rep.* 5 (2015) 8614. <https://doi.org/10.1038/srep08614>.
- [45] Z. Pan, S. Dash, J.A. Weibel, S. V Garimella, Assessment of Water Droplet Evaporation Mechanisms on Hydrophobic and Superhydrophobic Substrates, *Langmuir*. 29 (2013) 15831–15841. <https://doi.org/10.1021/la4045286>.
- [46] F.G.H. Schofield, S.K. Wilson, D. Pritchard, K. Sefiane, The lifetimes of evaporating sessile droplets are significantly extended by strong thermal effects, *J. Fluid Mech.* 851 (2018) 231–244. <https://doi.org/DOI: 10.1017/jfm.2018.496>.
- [47] Y. Wang, L. Ma, X. Xu, J. Luo, Expressions for the evaporation of sessile liquid droplets incorporating the evaporative cooling effect, *J. Colloid Interface Sci.* 484 (2016) 291–297. <https://doi.org/https://doi.org/10.1016/j.jcis.2016.09.011>.
- [48] M. Potash, P.C. Wayner, Evaporation from a two-dimensional extended meniscus,

- 
- Int. J. Heat Mass Transf. 15 (1972) 1851–1863.  
[https://doi.org/https://doi.org/10.1016/0017-9310\(72\)90058-0](https://doi.org/https://doi.org/10.1016/0017-9310(72)90058-0).
- [49] C. Kunkelmann, K. Ibrahim, N. Schweizer, S. Herbert, P. Stephan, T. Gambaryan-Roisman, The effect of three-phase contact line speed on local evaporative heat transfer: Experimental and numerical investigations, Int. J. Heat Mass Transf. 55 (2012) 1896–1904.  
<https://doi.org/https://doi.org/10.1016/j.ijheatmasstransfer.2011.11.044>.
- [50] M. Elena Diaz, J. Fuentes, R.L. Cerro, M.D. Savage, An analytical solution for a partially wetting puddle and the location of the static contact angle, J. Colloid Interface Sci. 348 (2010) 232–239.  
<https://doi.org/https://doi.org/10.1016/j.jcis.2010.04.030>.
- [51] C. Ketelaar, V.S. Ajaev, Evaporation, viscous flow, and electrostatic interaction of charged interfaces in the apparent contact line region, Phys. Fluids. 27 (2015) 112110. <https://doi.org/10.1063/1.4935874>.
- [52] M. Ojha, A. Chatterjee, G. Dalakos, P.C. Wayner, J.L. Plawsky, Role of solid surface structure on evaporative phase change from a completely wetting corner meniscus, Phys. Fluids. 22 (2010) 52101. <https://doi.org/10.1063/1.3392771>.
- [53] Z. Zheng, L. Zhou, X. Du, Y. Yang, Numerical investigation on conjugate heat transfer of evaporating thin film in a sessile droplet, Int. J. Heat Mass Transf. 101 (2016) 10–19.  
<https://doi.org/https://doi.org/10.1016/j.ijheatmasstransfer.2016.05.005>.
- [54] S. HASHIMOTO, C. HONG, I. UENO, Transient Growth Process of Precursor Film at Early Stage of Droplet Spreading, J. Therm. Sci. Technol. 7 (2012) 487–496. <https://doi.org/10.1299/jtst.7.487>.
-

- 
- [55] S. Shiimoto, K. Yamaguchi, M. Kobayashi, Time Evolution of Precursor Thin Film of Water on Polyelectrolyte Brush, *Langmuir*. 34 (2018) 10276–10286. <https://doi.org/10.1021/acs.langmuir.8b02070>.
- [56] G. Guéna, C. Poulard, A.M. Cazabat, The leading edge of evaporating droplets, *J. Colloid Interface Sci.* 312 (2007) 164–171. <https://doi.org/https://doi.org/10.1016/j.jcis.2006.06.023>.
- [57] C.-T. Pham, G. Berteloot, F. Lequeux, L. Limat, Dynamics of complete wetting liquid under evaporation, *EPL (Europhysics Lett.)* 92 (2010) 54005. <https://doi.org/10.1209/0295-5075/92/54005>.
- [58] T. Pompe, S. Herminghaus, Three-Phase Contact Line Energetics from Nanoscale Liquid Surface Topographies, *Phys. Rev. Lett.* 85 (2000) 1930–1933. <https://doi.org/10.1103/PhysRevLett.85.1930>.
- [59] I. Ueno, K. Hirose, Y. Kizaki, Y. Kisara, Y. Fukuhara, Precursor Film Formation Process Ahead Macroscopic Contact Line of Spreading Droplet on Smooth Substrate, *J. Heat Transfer*. 134 (2012). <https://doi.org/10.1115/1.4005638>.
- [60] Y. Yang, L. Zhou, X. Du, Y. Yang, Fluid Flow and Thin-Film Evolution near the Triple Line during Droplet Evaporation of Self-Rewetting Fluids, *Langmuir*. 34 (2018) 3853–3863. <https://doi.org/10.1021/acs.langmuir.8b00170>.
- [61] A.A. Mehrizi, H. Wang, Evaporation-induced receding contact lines in partial-wetting regime on a heated substrate, *Int. J. Heat Mass Transf.* 124 (2018) 279–287. <https://doi.org/https://doi.org/10.1016/j.ijheatmasstransfer.2018.03.066>.
- [62] H. Teshima, S. Misra, K. Takahashi, S.K. Mitra, Precursor-Film-Mediated Thermocapillary Motion of Low-Surface-Tension Microdroplets, *Langmuir*. 36 (2020) 5096–5105. <https://doi.org/10.1021/acs.langmuir.0c00148>.
-

- 
- [63] G. Nagayama, No Title, in: 4th ISMNT Korea, 2011.
- [64] Q. Xu, L. Zhou, X. Du, Y. Yang, Thin film profile and interfacial temperature distribution of binary fluid sessile droplet evaporating on heated substrate, *Int. J. Heat Mass Transf.* 135 (2019) 274–283.  
<https://doi.org/https://doi.org/10.1016/j.ijheatmasstransfer.2019.01.151>.
- [65] H. Wang, S. V Garimella, J.Y. Murthy, Characteristics of an evaporating thin film in a microchannel, *Int. J. Heat Mass Transf.* 50 (2007) 3933–3942.  
<https://doi.org/https://doi.org/10.1016/j.ijheatmasstransfer.2007.01.052>.
- [66] D. Hu, H. Wu, Z. Liu, Effect of liquid–vapor interface area on the evaporation rate of small sessile droplets, *Int. J. Therm. Sci.* 84 (2014) 300–308.  
<https://doi.org/https://doi.org/10.1016/j.ijthermalsci.2014.05.024>.
- [67] K. Chen, R.-N. Xu, P.-X. Jiang, Evaporation Enhancement of Microscale Droplet Impact on Micro/Nanostructured Surfaces, *Langmuir*. 36 (2020) 12230–12236.  
<https://doi.org/10.1021/acs.langmuir.0c01975>.
- [68] M.S. Hanchak, M.D. Vangsness, L.W. Byrd, J.S. Ervin, Thin film evaporation of n-octane on silicon: Experiments and theory, *Int. J. Heat Mass Transf.* 75 (2014) 196–206. <https://doi.org/https://doi.org/10.1016/j.ijheatmasstransfer.2014.03.063>.
- [69] Y.O. Popov, Evaporative deposition patterns: Spatial dimensions of the deposit, *Phys. Rev. E*. 71 (2005) 36313. <https://doi.org/10.1103/PhysRevE.71.036313>.
- [70] H. Hu, R.G. Larson, Evaporation of a Sessile Droplet on a Substrate, *J. Phys. Chem. B*. 106 (2002) 1334–1344. <https://doi.org/10.1021/jp0118322>.
- [71] T.A.H. Nguyen, A. V Nguyen, M.A. Hampton, Z.P. Xu, L. Huang, V. Rudolph, Theoretical and experimental analysis of droplet evaporation on solid surfaces, *Chem. Eng. Sci.* 69 (2012) 522–529.
-



- 
- <https://doi.org/https://doi.org/10.1016/j.ces.2011.11.009>.
- [72] S. Poudel, A. Zou, S.C. Maroo, Droplet Evaporation on Porous Nanochannels for High Heat Flux Dissipation, *ACS Appl. Mater. Interfaces*. 13 (2021) 1853–1860. <https://doi.org/10.1021/acsami.0c17625>.
- [73] R. Gimenez, G.J.A.A. Soler-Illia, C.L.A. Berli, M.G. Bellino, Nanopore-Enhanced Drop Evaporation: When Cooler or More Saline Water Droplets Evaporate Faster, *ACS Nano*. 14 (2020) 2702–2708. <https://doi.org/10.1021/acs.nano.9b06618>.
- [74] X. Chen, J. Chen, X. Ouyang, Y. Song, R. Xu, P. Jiang, Water Droplet Spreading and Wicking on Nanostructured Surfaces, *Langmuir*. 33 (2017) 6701–6707. <https://doi.org/10.1021/acs.langmuir.7b01223>.
- [75] H. Chen, Q. An, H. Zhang, C. Li, H. Fang, Z. Yin, Predicting the lifetimes of evaporating droplets in ordered arrays, *Phys. Fluids*. 34 (2022) 82010. <https://doi.org/10.1063/5.0105243>.
- [76] O. Carrier, N. Shahidzadeh-Bonn, R. Zargar, M. Aytouna, M. Habibi, J. Eggers, D. Bonn, Evaporation of water: evaporation rate and collective effects, *J. Fluid Mech.* 798 (2016) 774–786. <https://doi.org/DOI: 10.1017/jfm.2016.356>.
- [77] S. Hatte, K. Pandey, K. Pandey, S. Chakraborty, S. Basu, Universal evaporation dynamics of ordered arrays of sessile droplets, *J. Fluid Mech.* 866 (2019) 61–81. <https://doi.org/DOI: 10.1017/jfm.2019.105>.
- [78] A.M.J. Edwards, J. Cater, J.J. Kilbride, P. Le Minter, C. V Brown, D.J. Fairhurst, F.F. Ouali, Interferometric measurement of co-operative evaporation in 2D droplet arrays, *Appl. Phys. Lett.* 119 (2021) 151601. <https://doi.org/10.1063/5.0064924>.
-

- 
- [79] K. Pandey, S. Hatte, K. Pandey, S. Chakraborty, S. Basu, Cooperative evaporation in two-dimensional droplet arrays, *Phys. Rev. E.* 101 (2020) 43101. <https://doi.org/10.1103/PhysRevE.101.043101>.
- [80] G. Laghezza, E. Dietrich, J.M. Yeomans, R. Ledesma-Aguilar, E.S. Kooij, H.J.W. Zandvliet, D. Lohse, Collective and convective effects compete in patterns of dissolving surface droplets, *Soft Matter.* 12 (2016) 5787–5796. <https://doi.org/10.1039/C6SM00767H>.
- [81] E. Dietrich, S. Wildeman, C.W. Visser, K. Hofhuis, E.S. Kooij, H.J.W. Zandvliet, D. Lohse, Role of natural convection in the dissolution of sessile droplets, *J. Fluid Mech.* 794 (2016) 45–67. [https://doi.org/DOI: 10.1017/jfm.2016.158](https://doi.org/DOI:10.1017/jfm.2016.158).
- [82] A. Fick, Ueber Diffusion, *Ann. Phys.* 170 (1855) 59–86. <https://doi.org/https://doi.org/10.1002/andp.18551700105>.
- [83] T.R. Marrero, E.A. Mason, Gaseous Diffusion Coefficients, *J. Phys. Chem. Ref. Data.* 1 (1972) 3–118. <https://doi.org/10.1063/1.3253094>.
- [84] J.M. Stauber, S.K. Wilson, B.R. Duffy, K. Sefiane, On the lifetimes of evaporating droplets with related initial and receding contact angles, *Phys. Fluids.* 27 (2015) 122101. <https://doi.org/10.1063/1.4935232>.
- [85] D. Zhang, G. Nagayama, Effective Wetting Area Based on Electrochemical Impedance Analysis: Hydrophilic Structured Surface, *Langmuir.* 35 (2019) 16508–16513. <https://doi.org/10.1021/acs.langmuir.9b03349>.
- [86] D. Zhang, S. Takase, G. Nagayama, Measurement of effective wetting area at hydrophobic solid–liquid interface, *J. Colloid Interface Sci.* 591 (2021) 474–482. <https://doi.org/https://doi.org/10.1016/j.jcis.2021.01.056>.
- [87] C.A. Schneider, W.S. Rasband, K.W. Eliceiri, NIH Image to ImageJ: 25 years of

- image analysis, *Nat. Methods*. 9 (2012) 671–675.  
<https://doi.org/10.1038/nmeth.2089>.
- [88] D.H. Shin, S.H. Lee, C.K. Choi, S. Retterer, The evaporation and wetting dynamics of sessile water droplets on submicron-scale patterned silicon hydrophobic surfaces, *J. Micromechanics Microengineering*. 20 (2010) 55021.  
<https://doi.org/10.1088/0960-1317/20/5/055021>.
- [89] N. V Churaev, V.D. Sobolev, Prediction of contact angles on the basis of the Frumkin-Derjaguin approach, *Adv. Colloid Interface Sci.* 61 (1995) 1–16.  
[https://doi.org/https://doi.org/10.1016/0001-8686\(95\)00257-Q](https://doi.org/https://doi.org/10.1016/0001-8686(95)00257-Q).
- [90] J.-J. Zhao, Y.-Y. Duan, X.-D. Wang, B.-X. Wang, Effect of Nanostructured Roughness on Evaporating Thin Films in Microchannels for Wenzel and Cassie–Baxter States, *J. Heat Transfer*. 135 (2013). <https://doi.org/10.1115/1.4023230>.
- [91] MATLAB and Statistics Toolbox Release 2012b, The MathWorks, Inc., Natick, Massachusetts, United States., (n.d.).
- [92] J.M. Stauber, S.K. Wilson, B.R. Duffy, K. Sefiane, On the lifetimes of evaporating droplets, *J. Fluid Mech.* 744 (2014) R2. <https://doi.org/DOI:10.1017/jfm.2014.94>.
- [93] D.J. Fairhurst, Predicting evaporation rates of droplet arrays, *J. Fluid Mech.* 934 (2022) F1. <https://doi.org/DOI:10.1017/jfm.2021.1084>.
- [94] A.W. Wray, B.R. Duffy, S.K. Wilson, Competitive evaporation of multiple sessile droplets, *J. Fluid Mech.* 884 (2020) A45. <https://doi.org/DOI:10.1017/jfm.2019.919>.
- [95] H. Zhang, Y. Kita, D. Zhang, G. Nagayama, Y. Takata, K. Sefiane, A. Askounis, Drop Evaporation on Rough Hot-Spots: Effect of Wetting Modes, *Heat Transf.*

- Eng. 41 (2020) 1654–1662. <https://doi.org/10.1080/01457632.2019.1640458>.
- [96] D. Orejon, K. Sefiane, M.E.R. Shanahan, Stick–Slip of Evaporating Droplets: Substrate Hydrophobicity and Nanoparticle Concentration, *Langmuir*. 27 (2011) 12834–12843. <https://doi.org/10.1021/la2026736>.
- [97] V. Bergeaud, V. Lefebvre, SALOME A software integration platform for multi-physics, pre-processing and visualisation, in: *Proc. SNA + MC2010 Jt. Int. Conf. Supercomput. Nucl. Appl. + Monte Carlo 2010 Tokyo, Japan, 2010*: p. 1630. [http://inis.iaea.org/search/search.aspx?orig\\_q=RN:43053515](http://inis.iaea.org/search/search.aspx?orig_q=RN:43053515).
- [98] H.G. Weller, G. Tabor, H. Jasak, C. Fureby, A tensorial approach to computational continuum mechanics using object-oriented techniques, *Comput. Phys.* 12 (1998) 620–631. <https://doi.org/10.1063/1.168744>.
- [99] J.P. Ahrens, B. Geveci, C.C. Law, ParaView: An End-User Tool for Large-Data Visualization, in: *Vis. Handb.*, 2005.

## **Acknowledgements**

First, I would like to express my deepest gratitude to the Japanese government for granting me the Monbukagakusho (MEXT) scholarship and generous financial support during my doctoral studies in Japan. My sincere gratitude extends to my doctoral advisor, Prof. Gyoko Nagayama, for giving me the opportunity to study this research topic in Japan and for her support during my doctoral studies. My sincere thanks to Prof. Nobuyuki Tsuboi, Prof. Koji Miyazaki, Prof. Masato Yamamura, and Prof. Tomohide Yabuki for their insightful comments and encouragement during the evaluation of my dissertation. I also thank Dr. Alexandros Askounis (University of East Anglia, UK) and Prof. Hsiu-Yang Tseng (National Taiwan University of Science and Technology, Taiwan) for fruitful collaborations on related projects during my doctoral course. I would also like to acknowledge my former advisors Prof. Taqi Ahmed Cheema (GIK Institute, Pakistan), Prof. Qu Zhiguo (Xi'an Jiaotong University, China) and Prof. Muhammad Ali Kamran (UET Peshawar, Pakistan) for teaching me the fundamentals of heat and mass transfer and for their continuous encouragement to achieve scientific excellence.

I am indebted to all current and former Heat Transfer Lab members (i.e., both Japanese and international students during 2018-2023), seniors, and colleagues at Kyushu Institute of Technology for their encouragement and constructive feedback. I wholeheartedly admire the unconditional and sincere support of Dr. Shrikant Siani, Dr. Madhu Chennapuram, Sackdavong Do Mangkhaseum, Mustafa Anjum, Kalash Dixit, Gaurav Kumar, Sadam Hussain, Yu Mengqi, Jiao Yihang, Meng Xianghua, Bao

Jianchen, Yu Yankun, Chen Wentao, Kota Nishiyama, Tsubasa Nakamura, Chihiro Hoshino, Naoki Shiraishi, and Masaki Fujihara. I am also grateful to my friends inside and outside the university for their support, encouragement, and inspiration, which made my doctoral journey an unforgettable experience.

I would like to express my heartfelt gratitude to my role model and fatherly mentor Dr. Z.A. Khan (Texas, US) for his regular support on my professional and personal development since we met during my high school years. This work would not have been possible without the family's trust and faith in my struggle during the last four and half years of my doctoral studies in Japan. In particular, I deeply admire the support from my father, mother, aunts, uncles, sisters, and brother at all levels. Finally, I would like to dedicate my research achievements to pillar of support in my life, my girlfriend, Miss Lili for her continuous support, love, and belief in me and has been a source of strength and inspiration throughout my doctoral journey.

Mohib

February 02, 2023

## **Research Achievements**

### **Journal articles**

- [1] M. Mohib Ur Rehman and Gyoko Nagayama, Contribution of solid–liquid–vapor interface to droplet evaporation, *Colloids and Surfaces A: Physicochemical and Engineering Aspects*, Volume 656, 130419, 2023
  
- [2] M. Mohib Ur Rehman, Alexandros Askounis and Gyoko Nagayama, Effect of surface wettability on evaporation rate of droplet array, *Physics of Fluids*, Volume 35, 037121, 2023

### **Presentations**

- [1] M. Mohib Ur Rehman and Gyoko Nagayama, Role of Solid-liquid-vapor Interface in Droplet Evaporation, *International Joint Seminar on Mechanical Engineering 2021*
  
- [2] M. Mohib Ur Rehman and Gyoko Nagayama, A theoretical model to account evaporation at solid-liquid-vapor interface of a droplet, *International Joint Seminar on Mechanical Engineering 2020*
  
- [3] M. Mohib Ur Rehman and Gyoko Nagayama, Numerical Simulations on Heat and Mass Transfer at Solid-liquid-vapor Triple-phase Contact Region, *International Joint Seminar on Thermal Engineering 2019*

- [4] M. Mohib Ur Rehman and Gyoko Nagayama, Numerical Simulation of Droplet Evaporation Coupling with Solid-liquid-vapor Interfacial Heat and Mass Transfer, International Joint Seminar on Mechanical Engineering 2019
- [5] M. Mohib Ur Rehman and Gyoko Nagayama, Heat Transfer Enhancement and Fluid Flow Characteristics in a Microchannel Heat Sink with Different Side Wall Ribs: A Comparative Numerical Study, International Joint Seminar on Mechanical Engineering 2018